AD-A258 557

US Army Corps
of Engineers

DETERMINATION OF RESIDUAL STRESS AND EFFECTS IN THICK-SECTION WELDMENTS FOR HYDRAULIC STRUCTURES

by

Chon L. Tsai, Dong S. Kim, Yong L. Shim
Zhili Feng, Sung Lee

Department of Welding Engineering
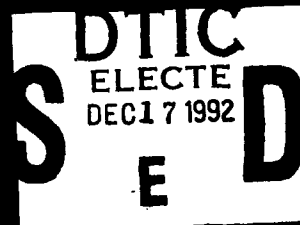Ohio State University
Columbus, Ohio

and

John Jaeger

Information Technology Laboratory

DEPARTMENT OF THE ARMY
Waterways Experiment Station, Corps of Engineers
3909 Halls Ferry Road, Vicksburg, Mississippi   39180-6199

DTIC
ELECTE
DEC 1 7 1992
E

September 1992

Final Report

92-31492

REPORT DOCUMENTATION PAGE

Public reporting burden for this collection of information is estimated to average 1 hour per response, including the time for reviewing instructions, searching existing data sources, gathering and maintaining the data needed, and completing and reviewing the collection of information. Send comments regarding this burden estimate or any other aspect of this collection of information, including suggestions for reducing this burden, to Washington Headquarters Services, Directorate for Information Operations and Reports, 1215 Jefferson Davis Highway, Suite 1204, Arlington, VA 22202-4302, and to the Office of Management and Budget, Paperwork Reduction Project (0704-0188), Washington, DC 20503.

1. AGENCY USE ONLY (Leave blank)	2. REPORT DATE September 1992	3. REPORT TYPE AND DATES COVERED Final report

4. TITLE AND SUBTITLE

Determination of Residual Stress and Effects in Thick-Section Weldments for Hydraulic Structures

5. FUNDING NUMBERS

6. AUTHOR(S)

Chon L. Tsai, Dong S. Kim, Yong L. Shim, Zhili Feng, Sung Lee, John Jaeger

7. PERFORMING ORGANIZATION NAME(S) AND ADDRESS(ES)

See reverse.

8. PERFORMING ORGANIZATION REPORT NUMBER

Technical Report ITL-92-8

9. SPONSORING / MONITORING AGENCY NAME(S) AND ADDRESS(ES)

US Army Corps of Engineers
Washington, DC 20314-1000

10. SPONSORING / MONITORING AGENCY REPORT NUMBER

11. SUPPLEMENTARY NOTES

Available from National Technical Information Service, 5285 Port Royal Road, Springfield, VA 22161.

12a. DISTRIBUTION / AVAILABILITY STATEMENT

Approved for public release; distribution is unlimited.

12b. DISTRIBUTION CODE

13. ABSTRACT (Maximum 200 words)

The primary objective of this research was to develop numerical methodology which may be used to predict thermal and residual stress fields created by welding of thick plates and to verify the results experimentally. A two-dimensional thermomechanical finite element model was developed and is described in this report. Methods for modeling heat input of welding considering arc movement and number of weld passes were developed. The methods which were developed are referred to as ramp heat input and lumping.

Five experiments were carried out using 1/2-in. and 1-in. steel plates with various weld geometries including single-bevel, single-V and double-V groove welds. This report describes experimental techniques which were used to measure temperature and residual stress. Experimental results are compared with analytical predictions. The finite element model developed by this research can be used to predict thermal and residual stress fields which are created during welding of thick plates.

14. SUBJECT TERMS

Finite element modeling	Thermal loading
Heat input	Thermal strain
Residual stress	Welding

15. NUMBER OF PAGES
117

16. PRICE CODE

17. SECURITY CLASSIFICATION OF REPORT UNCLASSIFIED	18. SECURITY CLASSIFICATION OF THIS PAGE UNCLASSIFIED	19. SECURITY CLASSIFICATION OF ABSTRACT	20. LIMITATION OF ABSTRACT

NSN 7540-01-280-5500

Standard Form 298 (Rev. 2-89)
Prescribed by ANSI Std. Z39-18
298-102

7. (Concluded).

Ohio State University
Department of Welding Engineering
Columbus, OH;
US Army Engineer Waterways Experiment Station
Information Technology Laboratory
3909 Halls Ferry Road, Vicksburg, MS   39180-6199

PREFACE

The research described in this report was conducted by the Scientific and Engineering Application Center (S&EAC) of the Computer Aided Engineering Division (CAED), Information Technology Laboratory (ITL), US Army Engineer Waterways Experiment Station (WES), through the Civil Works Research and Development Program work unit Computer Analysis of Welds. Dr. John Jaeger, formerly of CAED, was Project Manager under the general supervision of Mr. H. Wayne Jones, Chief, S&EAC, and Dr. N Radhakrishnan, Director, ITL.

The investigation was performed at Ohio State University, Department of Welding Engineering, Design Group, under the supervision of Dr. Chon L. Tsai. Dr. Dong S. Kim, Mr. Yong L. Shim, and Dr. Jaeger were responsible for finite element modeling. Experimental work was directed by Mr. Zhili Feng, and welding procedures were selected by Mr. Sung G. Lee.

At the time of the publication of this report, Director of WES was Dr. Robert W. Whalin. Commander and Deputy Director was COL Leonard G. Hassell, EN.

Accesion For		
NTIS CRA&I		☒
DTIC TAB		☐
Unannounced		☐
Justification		
By		
Distribution /		
Availability Codes		
Dist	Avail and / or Special	
A-1		

DTIC QUALITY INSPECTED 1

1

CONTENTS

LIST OF TABLES

LIST OF FIGURES

3

LIST OF FIGURES (Continued)

4

5

CONVERSION FACTORS, NON-SI TO SI (METRIC)
UNITS OF MEASUREMENT

Non-SI units of measurement in this report can be converted to SI (metric) units as follows:

Multiply	By	To Obtain
degrees (angle)	0.01745329	radians
Fahrenheit degrees	5/9	Celsius degrees or kelvins*
inches	25.4	millimetres
kips per square inch	6894757.0	pascals
microns	0.000001	metres
pounds mass per cubic inch	27,680.33	kilograms per cubic metre

---

* To obtain Celsius (C) temperature readings from Fahrenheit (F) readings, use the following formula: $C = (5/9) (F - 32)$. To obtain Kelvin readings, use: $K = (5/9) (F - 32) + 273.15$.

PART I: INTRODUCTION

Welding Costs

1. Each time a new tainter gate, miter gate, lift gate, bulkhead, or lock culvert valve is designed and fabricated, thousands of dollars are spent welding each assembly together. At the completion of a single new civil works project, the Government will have spent millions of dollars on welding. With the upcoming design and construction of such major civil works projects as Red River Locks and Dams 3, 4 and 5, the second lock on Locks and Dam 26 (R), and the Olmstead and Bonneville projects, several million dollars will be spent in fabricating welded steel structures. It is imperative that these welded connections be designed cost effectively for optimum serviceability, reliability, and safety.

Welding Stress and Distortion

2. As the steel hydraulic structures are being fabricated, weld residual stress and distortion accumulates. Compensation for this distortion may require physically forcing the steel structure into an acceptable operational alignment. Physically forcing the structure into alignment induces additional stress into the system that was not accounted for in the initial design. Physically forcing a tainter gate, sector gate, or miter gate into alignment will allow immediate operation of the structure, however long-term operational and maintenance effects associated with this induced stress and resulting eccentricities will ultimately be the trade-off.

3. In addition to distortion, welding induced residual stress increases the fracture driving force, such as the stress intensity factor (K), for discontinuities existing in the weld. Residual stress is developed as a result of manufacturing and fabricating a steel structure. In the case of welded structures, once the welding arc is established, nonlinear thermal loading cycles are created. This thermally induced loading produces compressive and tensile residual stress after cooling. This stress increases the potential for cracking. Currently, there are little data available pertaining to the magnitude and nature of the residual stress in the plate along the through-thickness direction. In addition, the thermal loading will alter the original base metal toughness adjacent to the weld in the heat affected zone (HAZ).

8

The objective of this study is to develop a numerical evaluation methodology for thermal and residual stress fields created by welding of thick plates and to verify the results experimentally.

4. As the weld process progresses, both the weld metal and the base metal experience an increase in temperature. At the solidus temperature, the material within the fusion zone begins to liquefy. Upon cooling, a reversal occurs and the fusion zone solidifies to complete the joining process. A consequential result of the induced nonlinear thermal cycles associated with the welding process is the development of residual stresses. The fluid material in the fusion zone is bounded by the solid HAZ material and unaffected base metal. The solid material adjacent to the fusion zone acts as a mechanical constraint that results in inelastic strains being produced as the fusion zone material solidifies. As the fusion zone solidifies, the grain growth progresses from the heat affected zone toward the center of the weld. The elastic strains result in tensile residual thermal stresses in the fusion zone. Previous work (Masubuchi 1980a) has shown that tensile longitudinal residual stresses in the fusion zone exist after welding and results of analyses indicate that residual tensile stresses are frequently at the yield point of the material as shown in Figure 1. Currently, there are little data available pertaining to the magnitude and nature of the residual stress in the plate through thickness direction. As the plate thickness increases, the number of weld passes required to complete a full penetration weld also increases. Consequently, the plate is now subjected to multiple nonlinear thermal cycles and possibly a more complex inelastic strain pattern.

Three-Bar Analogy Method of Evaluating Residual Stress

5. A simple method for conceptually understanding residual stress in a plate created from welding is the three-bar analogy. This analogy simplifies the weld into three bars parallel to each other, one bar is parallel and adjacent to each side of the weld with the third bar being the fusion zone itself (Figure 2). As the fusion zone heats and liquifies during welding, no stress can be developed in bar 3, because the molten pool can not transfer a load. Bars 1 and 2 are isolated from bar 3, consequently there is no thermal expansion created in either of these bars. As bar 3 solidifies on cooling, it shrinks. The end constraints prevent shrinkage which results in bar 3 going into tension while bars 1 and 2 are in compression to satisfy the equilibrium

9

a. Butt weld

b. Distribution of σ_x along YY

c. Distribution of σ_y along XX
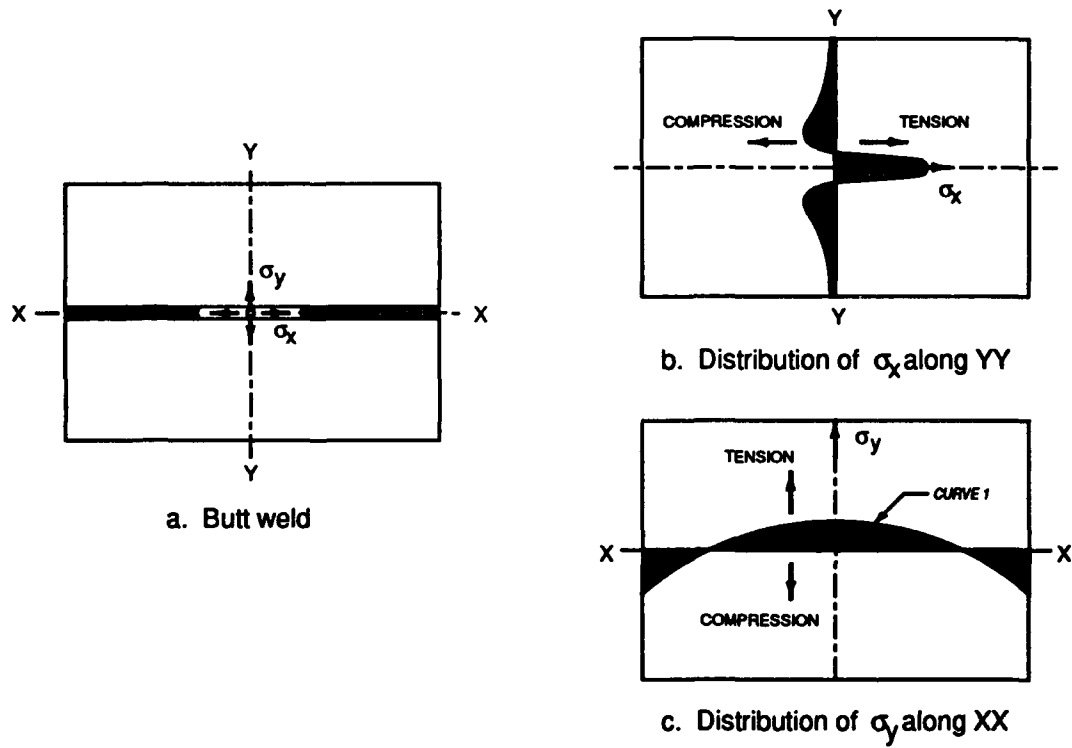
Figure 1. Typical distributions of residual stresses in butt weld

a. Free state   b. Stressed state
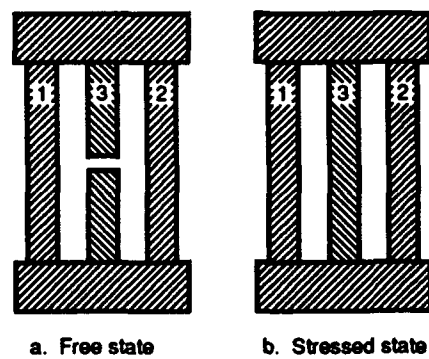
Figure 2. Three-bar analogy of welding stresses

10

condition. The three-bar analogy provides qualitative information about residual stresses and gives basis for instinctive judgement. The simplification, however, often introduced in the theoretical analysis does not warrant the accuracy of the analysis quantitatively, especially for the multipass welded structures.

6. The nonlinear finite element method was introduced to overcome theoretical difficulties that exist in analogies such as the three-bar analogy. In the finite element method, temperature data calculated from the thermal finite element analysis are used as input for the stress analysis. Plane stress conditions are reasonable for evaluating stresses on the surface of a thin plate. For thick plates or multipass cases, plane strain assumptions may not adequately represent the constraint along the welding direction. The generalized plane strain assumption was implemented in this study to allow parallel rigid body motion perpendicular to the welding direction. This study was performed using the ABAQUS (Hibbit, Karlson, and Sorensen 1988) commercial finite element analysis package.

7. To experimentally measure thermal strain during welding and residual strain after welding, American Society for Testing and Materials (ASTM) A-36 steel plates with two different thicknesses (1/2- and 1-in. thickness) were used. The selected welding process for the experimental work was gas metal arc welding (GMAW), since it is considered a standard process. The plates were annealed before welding to minimize the influence of preexisting stress from prior cutting or rolling.

8. Temperature profiles were obtained through the use of thermocouples and a data acquisition system was developed at the Department of Welding Engineering, Ohio State University. Thermal strain during welding was also obtained using high-temperature strain gages. The experimental temperature fields were compared with finite element results from a thermal mechanical model developed at the University.

9. Residual stresses at the surface of the plates were experimentally measured using the blind-hole drilling method. American Stress Technology Co. (AST) X-ray diffraction and magneto-elastic equipments were considered as a means of confirming the surface residual stress measurements obtained by the blind-hole drilling method. Since the X-ray measurement system is more sensitive to plate surface conditions, the magneto-elastic technique was studied. However, only limited results were obtained because of the time restraint imposed by this project. They are presented in Appendix A.

10.   The residual stress measurement equipment described is limited only to surface measurements.   To obtain data on the distribution of residual stress in the through-thickness direction, the ABAQUS finite element program was utilized.   Thermal mechanical finite element analyses were performed to predict the residual stress distribution in the through-thickness direction.

PART II: EXPERIMENTS

Overview of Experiments

11. The experimental tests were directed toward collecting temperature and stress information on the surfaces of the weldment. The experimental results were used for comparison and calibration of the finite element analysis. Once the computer simulation results obtained from finite element method match the experimental work, the computer simulation would become a tool for investigating the temperature and stress distributions in the weldment. It could also be used to study the effect of welding parameters on the stress distributions. This chapter discusses the experimental instrumentation, procedures, and measurement results.

12. Many techniques have been reported for measuring residual stresses in metals (Masubuchi 1980b). These techniques include stress relaxation (such as blind-hole drilling or sectioning), X-ray diffraction, ultrasonic, and magneto-elastic (Barkhausen effect) techniques. One of the most widely used techniques for measuring residual stress is the blind-hole drilling method. The measurement procedure is relatively simple and has been standardized as ASTM Standard Test Method E837-85 (ASTM 1985). In this project, the blind-hole drilling method was the primary method used to experimentally determine the surface residual stresses in the weldment. Limited information was also obtained by using the magneto-elastic method.

13. Strain gages were used to measure variations in thermal strain (transient conditions). Although weldable strain gages can be used under high temperatures, their large dimensions make them unacceptable to evaluate sensitive thermal strain variations during welding because of the existence of steep stress gradients near the weld. The nature of smaller precision strain gages and their bonding materials restrict their maximum service temperature. In general, the maximum temperature can not exceed 700 °F (Measurement Group, Inc., 1989). When these smaller gages are used, the temperature changes at the strain gage location must be monitored during welding to compensate the temperature induced electrical resistance changes in the strain gage. In this project, efforts have been made to measure the transient thermal strain during welding.

14. Thermocouple and infrared techniques have been used to record the surface temperature changes during welding. Quantitative data at certain locations were collected via thermocouples for local comparison with the finite element results. The infrared method produced more global semiquantitative/qualitative information that was used for general overall model comparisons.

15. The next several sections present the technical background for the testing methods, followed by descriptions of testing instrumentation, testing procedures, and measurement results pertaining to the experimental work.

Background

Blind-hole drilling
residual stress measurements

16. Measurement of residual stress in opaque objects cannot be accomplished by conventional procedures for experimental stress analysis, since the strain sensor (strain gage, photoelastic coating, etc.) is totally insensitive to the history of the part and measures only changes in strain after installation of the sensor. To measure residual stress with these standard sensors, the locked-in stress must be relieved in some fashion so that the sensor can register the change in strain caused by removal of the material. The relationship between the residual stresses and the measured strain relaxation in the remaining material can be found analytically for simply shaped specimens with material removed in a simple, geometric way.

17. Hole drilling provides stress relaxation in the vicinity of the hole. From theory of elasticity, a closed-form solution can be obtained for the case of a hole drilled completely through a thin plate in which the residual stress, prior to the introduction of the hole, is uniformly distributed through the plate thickness (Timoshenko and Goodier 1951). The theoretical solution for the radial strain relaxation is (Muskhelishvili 1953)

$$\epsilon_r = (A + B \cos 2\theta)\sigma_{max} + (A - B \cos 2\theta)\sigma_{min} \qquad (1)$$

14

where

$$A = -\frac{1-\mu}{2E}\left(\frac{a}{r}\right)^2 \tag{2}$$

and

$$B = -\frac{1+\mu}{2E}\left\{\frac{4}{1+\mu}\left(\frac{a}{r}\right)^2 - 3\left(\frac{a}{r}\right)^4\right\} \tag{3}$$

where

σ_{max} — maximum principal stress at the point interested

σ_{min} — minimum principal stress at the point interested

a — hole radius

r — radius of the point interested

E — Young's modules

μ — Poisson's ratio

Θ — angular coordinate measured counterclockwise from the maximum principal stress direction.

18. For a strain gage rosette specially designed for residual stress measurement by the hole drilling method (Figure 3), this relationship can be inverted to give the magnitude and direction of the two principal stresses in terms of the measured radial strains. For the 45-deg rectangular rosette in Figure 3, the result (Measurement Group, Inc., 1988) is

$$\sigma_{max,min} = \frac{\epsilon_1 + \epsilon_3}{4A} \mp \frac{\sqrt{2}}{4B}\sqrt{(\epsilon_1 - \epsilon_2)^2 + (\epsilon_2 - \epsilon_3)^2} \tag{4}$$

$$\beta = \frac{1}{2}\tan^{-1}\left[\frac{2\epsilon_2 - \epsilon_1 - \epsilon_3}{\epsilon_1 - \epsilon_3}\right] \tag{5}$$

15
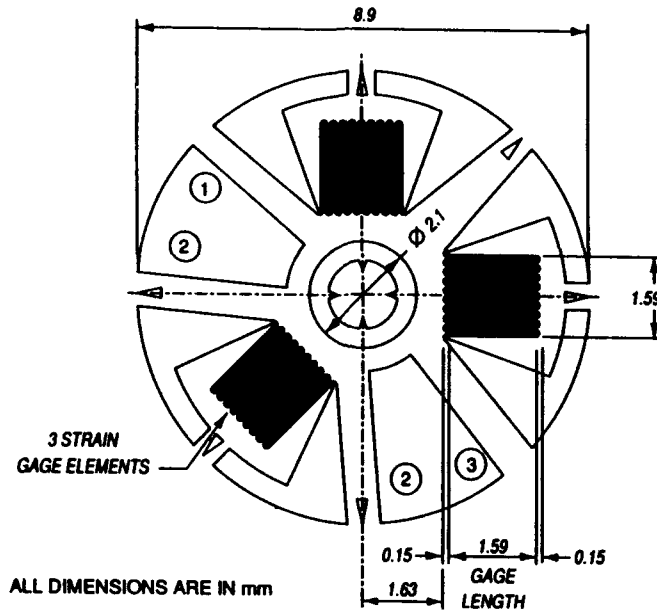
Figure 3. Rosette gage for residual stress
measurements, Measurement Group, Inc. (type
062-RE) (all dimensions are in millimetres)

$$\alpha = \begin{cases} \beta, & \text{if } \epsilon_1 \le \epsilon_3 \\ \beta + 90°, & \text{if } \epsilon_1 \ge \epsilon_3, \ \beta \le 0 \\ \beta - 90°, & \text{if } \epsilon_1 \ge \epsilon_3, \ \beta \ge 0 \end{cases} \tag{6}$$

where ϵ_1, ϵ_2, and ϵ_3 are the radial strains measured by the gages as numbered
in Figure 3, and α is the angle measured clockwise from gage 1 to the maximum
principal stress direction.

19. Careful consideration must be given for determining the appropriate
values for coefficients A and B. It should be noted that Equations 1 through
3 give only the stress distributions at points with coordinate (r,θ) around a
circular hole through a thin, wide plate subjected to uniform plane stresses.
However, the output of each gage tends to represent the average strain over
the area of the grid. As a result, more accurate values for the coefficients
can be obtained by integrating those equations over the areas of the respec-
tive gage grids. An alternative method is to measure them by experimental
calibration.

20. The introduction of a blind hole into a thick plate produces a very
complex local stress state, for which no exact solution is yet available from
the theory of elasticity. Fortunately, researchers (Measurement Group, Inc.,
1988; Rendler and Vignees 1966) have demonstrated that this case closely

16

parallels the through-hole condition in the general nature of the stress dis-
tribution. It follows, then, that Equations 1 through 6 are equally applica-
ble to the blind-hole implementation of the method when appropriate blind-hole
coefficients A and B are employed. Since these coefficients cannot be calcu-
lated directly from theoretical considerations, they must be obtained by
experimental calibration or by numerical procedures such as finite element
analysis.

21. In a generalized functional form, the coefficients can be expressed
as:

$$A = f_a \left(E, \mu, r, \frac{Z}{D_o} \right)$$
$$B = f_b \left(E, \mu, r, \frac{Z}{D_o} \right)$$

(7)

where

D_o — hole diameter

Z — hole depth

22. For commercially available strain gage rosettes designed for
residual stress measurement, coefficients A and B can be obtained from the
manufacture's engineering sheets. In general, these data are obtained under
the condition that the applied stresses are uniform through the thickness
direction. Hence, caution must be taken when these coefficients are applied
to a testing piece in which stresses vary in the thickness direction.

23. Obviously, the residual stress distribution influences the varia-
tion of relieved strain measured on the surface with respect to hole depth.
The plots of relieved strain variation with hole depth produced by different
residual stress distributions along the through-thickness direction should
have different shapes. This information may be used to study the residual
stress uniformity by comparing a testing plot with the standard plot
representing uniform through thickness stress. If the testing plot and the
standard plot have the same shape, then the stress in the through-thickness
direction would be most likely uniform and the magnitudes of the residual
stresses calculated from the above equations would be accurate. Although some
efforts have been made (Schajer 1981; Kelsey 1956; Kabiri 1984; Niku-Lari
1985), it is still immature to experimentally determine an arbitrary stress
distribution along the through-thickness direction from the plots of strain

17

variation with hole depth. In fact, the stress relaxation due to hole drilling is a local phenomenon. According to Saint-Venant Principle, the stress relaxation at the bottom of the hole will have negligible effect on the readings of the strain gage on the surface of the specimen, when the hole depth exceeds the hole diameter. Therefore, the hole drilling method can not determine the stress variation with depth in a thick plate.

24. As recommended in ASTM E837-85 (ASTM 1985), it is always preferable to drill the hole in small increments of depth, recording the observed strains and measured hole depth at each increment. Data can then be obtained to determine whether the residual stress is essentially uniform with depth, thus validating the use of the standard coefficients A and B for calculating the stress magnitudes.

25. When there are residual stress gradients parallel to the surface of the testing piece, the coefficients A and B provided by manufactures should be used cautiously to determine the residual stresses. This is particularly important for determining welding related residual stresses, since a steep stress gradient always exists near the weld.

26. From this consideration, we would conclude that the values of residual stresses obtained by the blind-hole drilling method are of average stresses over the hole depth and the hole diameter and depend upon the stress gradients in the through-thickness direction and along the surface.

Thermocouple temperature measurement

27. When two wires composed of dissimilar metals are joined at both ends and one end is heated, there is a continuous current which flows in the thermoelectric circuit. Thomas Seebeck made this discovery in 1821. If this circuit is broken, the net open circuit voltage (Seebeck voltage) is a function of the junction temperature and the composition of the two metals.

28. The Seebeck voltage cannot be directly measured because we must first connect a voltmeter to the thermocouple, and the voltmeter leads themselves create a new thermocouple circuit. Using the basic electrical circuit principles, it is easy to see that the resultant voltmeter reading will be proportional to the temperature difference $(T_1 - T_{ref})$ between the junctions. Thus, we can't find the temperature at the interested junction (T_1) unless we first find the temperature at the junctions between the thermocouple and the voltmeter (the Reference Temperature, T_{ref}).

29. One way to determine the reference temperature is to make voltmeter-thermocouple junctions on an isothermal (same temperature) block.

18

The isothermal block is an electrical insulator, a good heat conductor, and it serves to hold the reference junctions at the same temperature. The equivalent electric circuit is shown in Figure 4. Now the voltmeter reading is

$$V = \alpha \left(T_1 - T_{ref} \right) \tag{8}$$

where α is the Seebeck coefficient for the given thermocouple.
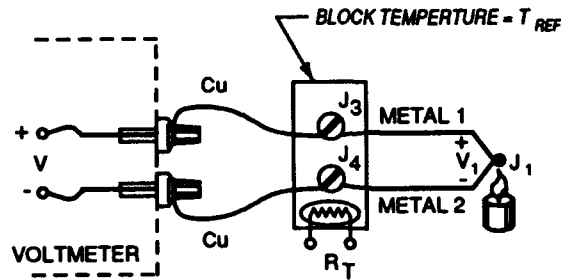
EXTERNAL REFERENCE JUNCTION-NO ICE BATH

Figure 4. Isothermal reference junction

30. A thermistor, with resistance R_T as a function of temperature, provides a way to measure the absolute temperature of the reference junctions. The reference junctions and the thermistor are all assumed to be at the same T_{ref}, due to the design of the isothermal block. Using a digital multimeter under computer control, we simply:

    <u>a</u>. Measure R_T to find T_{ref} and convert T_{ref} to its equivalent reference junction voltage V_{ref} $(V_{ref} = \alpha T_{ref})$

    <u>b</u>. Measure V in Figure 4, and add V_{ref} to find V_1, and convert V_1 to temperature T_1 $(V_1 = \alpha T_1)$

31. This procedure is known as software compensation because it relies upon the software of a computer to compensate for the effect of the reference junction. Software compensation becomes especially convenient when monitoring a large number of data points. This is accomplished by using the isothermal reference junction for more than one thermocouple. A relay scanner connects the voltmeter to the various thermocouples in sequence. Different types of thermocouples can also be mixed on the same isothermal junction block (often called a zone box) provided that appropriate modifications in software are

19

made. In addition, when using a data acquisition system with a built-in zone box, the thermocouples only need be simply connected to the system. All of the conversions are performed by the computer.

32. Since the Seebeck coefficient usually is not a constant over a wide range of temperature, better conversion accuracy can be obtained by using a power series polynomial:

$$T_1 = a_o + a_1 V_1 + a_2 V_1^2 + \cdots + a_n V_1^n \qquad (9)$$

where

T_1 = temperature at the junction of the thermocouple

V_1 = thermocouple voltage

a_i = polynomial coefficients unique to each thermocouple type

n = maximum order of the polynomial

33. As n increases, the accuracy of the polynomial improves. A representative number is n = 9 for $\pm$ 2 °F.

Infrared temperature measurements

34. The basic theory of the infrared temperature measurement system is the theory of black-body radiation. It is stated that all objects emit radiation in a manner related to their absolute temperatures and in proportion to the emissivity of their surfaces relative to that of an ideal black surface (Inframetrics 1981). A black body is an ideal radiation which can only be approximated in practice. It may be defined as a body absorbing all radiation incident upon it and reflects or transmits none.

35. Thermal radiation takes place at wave lengths between approximately 3×10^{-4} microns and 300 microns. The infrared wave lengths, which are useful for thermographic purposes since these convey radiant temperatures normally encountered at the earth temperatures, are between 2.0 and 14 microns. The temperature field in this infrared system can be evaluated using the Stefan-Boltzmann Law. The Stefan-Boltzmann Law states that the energy radiated by a black body is proportional to the absolute temperature and is written as follows:

$$W = rT^4 \qquad (10)$$

where

W = total radiance, watt/cm^2

20

r - Stefan-Boltzmann constant, watts/cm^2/K

T - absolute temperature, K

36. Therefore, infrared wave lengths emitted by the weldment can be measured and converted to a temperature field.

Experimental Instrumentation

Data acquisition system

37. To monitor transient strain or the thermal strain variations during welding, it is necessary to record the output from strain gages and the temperature changes at the strain gage locations. A data acquisition system has been specially developed to fulfill this requirement.

38. The data acquisition system was designed to measure the temperature and strain changes during welding. It was also developed to monitor strain relaxation during blind-hole drilling for residual stress measurement. Electric strain gages were used for strain measurement and thermocouples were used to measure temperature. The system can measure strain and temperature at the same time or separately.

39. The system configuration is sketched in Figure 5. It consists of four major components: an IBM AT computer, an HP3497A data acquisition/ control unit, an IBM graphic printer, and an HP6214B power supply. The communication between the IBM AT and the HP3497A is carried by an IEEE488 interface bus. Detailed information on each component can be found in individual technical references and/or user's manuals.

40. The electrical voltage output from the strain gages is entered into the HP3497A unit through the strain gage/bridge assemble board on the HP3497A. The HP6214B power supply provides the bridge excitation voltage for strain gage measurement. The thermocouple voltage is input into the HP3497A via the low thermal relay assembly board on the HP3497A. The HP3497A serves as an input channel scanner and input analog voltage digitalizer. Although the opening and closing of the input channel is done by the HP3497A, it is the IBM AT that controlled the sequence and timing of the channel scanning. In addition, the IBM AT converts the signals to stress and temperature data and stores that data on a hard disk.

41. To reduce the electrical noise generated during welding (particularly from power lines), the HP3497A data logger incorporates an integrating analog-to-digital conversion mechanism. However, the tradeoff is reduced
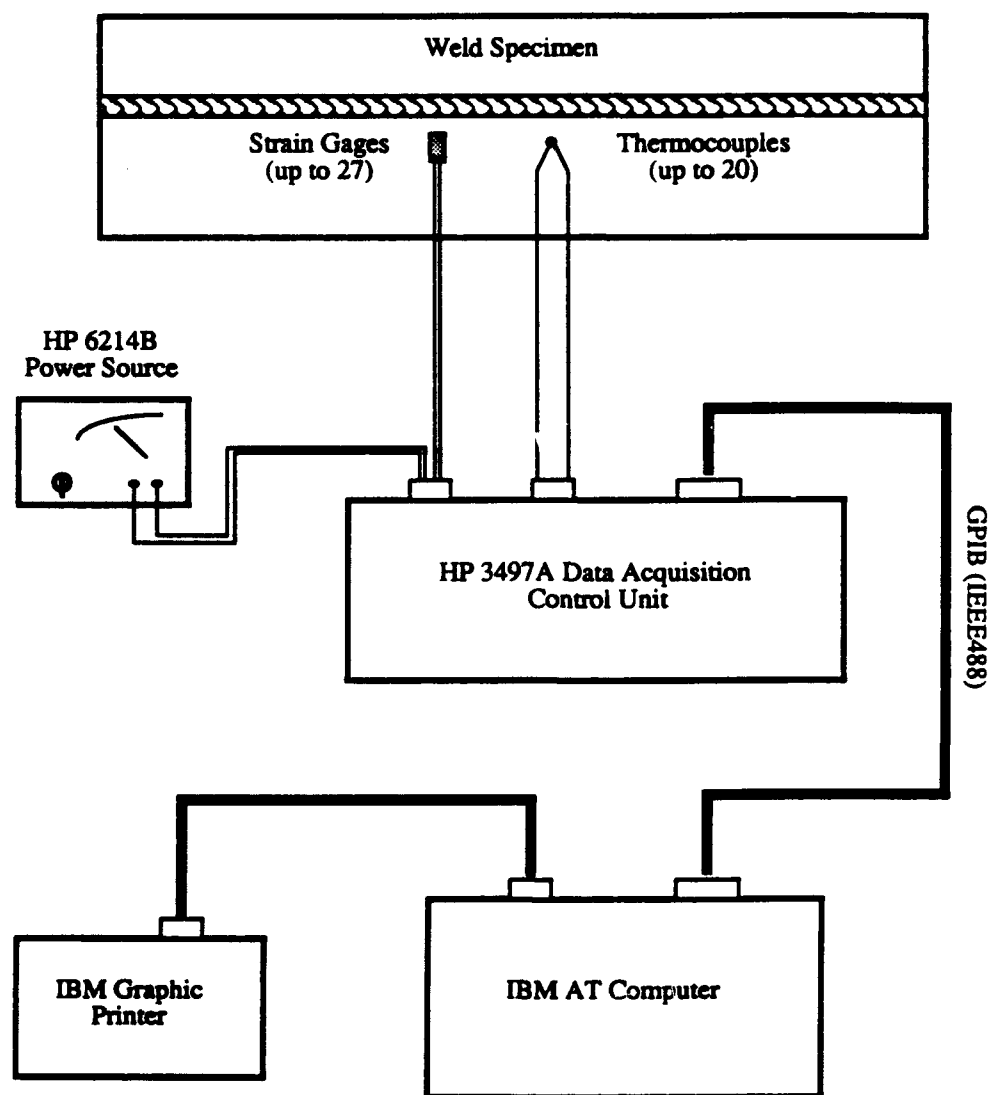
Figure 5. Configuration of the data acquisition system

scanning speed of the HP3497A. The overall maximum speed of the system is about 10 channels per second. Generally, this speed is fast enough for monitoring the temperature changes and the strain changes during welding.

42. The conversions of the thermocouple output and the strain gage output were performed on real time. The converted data were saved on the IBM AT hard disk before the next scanning cycle started. This minimizes the loss

of data if power failure occurs. This feature was specially useful when the data collection period was long or when data collection was conducted in an industrial environment and power line surges were significant.

43. An unbalanced Wheatstone bridge was used for strain gage measurements. Since quarter-bridge configurations were employed, the gages used were of the self-temperature compensated type.

44. The quarter-bridge circuit on the HP3497A strain/bridge assembly board is shown in Figure 6. R_g represents the testing strain gage, R_1, R_2, and R_3 are the completion resistors with values not changing during the test. The equations used to convert the strain gage output to strain are (Williams and McFetridge 1983)

$$\epsilon = - \frac{4V_r}{GF\ (1 + 2V_r)}$$

$$V_r = \left[\frac{V_{out}}{V_{in}}\right]_{strained} - \left[\frac{V_{out}}{V_{in}}\right]_{unstrained}$$

(11)

where

GF — gage factor

V_{out} — strain gage output voltage

V_{in} — excitation power supply voltage
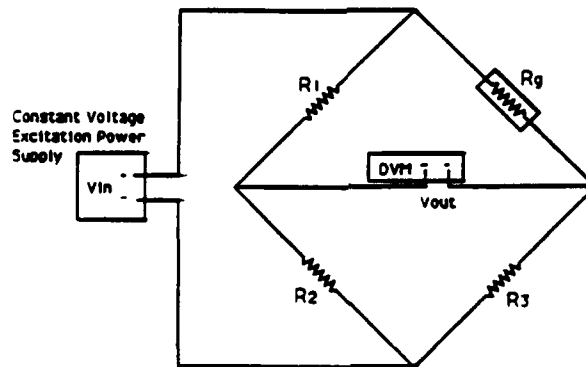
Figure 6. Configuration for unbalanced quarter-bridge strain gage measurement

45. Software compensation was used for the thermocouple measurements. The system can handle commonly used thermocouple types, such as:

ANSI standard type E:	Ni-Cr(+) vs. Cu-Cr(-) (Chromel-Constantan)
ANSI standard type J:	Fe(+) vs. Cu-Ni(-) (Iron-Constantan)
ANSI standard type K:	Ni-Cr(+) vs. Ni-Al(-) (Chromel-Alumel)
ANSI standard type R:	Platinum(+) vs. Platinum-13%Rhodium(-)
ANSI standard type S:	Platinum(+) vs. Platinum-10%Rhodium(-)
ANSI standard type T:	Cu(+) vs. Cu-Ni(-) (Copper-Constantan)
ANSI standard type B:	Pt-6%Rh(+) vs. Pt-30%Rh(-)
ANSI standard type N:	Ni-14.2%Cr-1.4%Si(+) vs. Ni-4.4%Si-0.1%Mg(-)
Non-ANSI standard type n:	(Nicrosil-Nisil)

46. The thermocouple characteristic curve (temperature versus voltage) is generally not a straight line over a wide temperature range. Polynomial curve fitting is often used for automated temperature measurement. In this system, the thermocouple characteristic curve was divided into eight sectors and each sector was approximated by a one-third-order polynomial, as shown in Figure 7. The data acquisition system measures the output voltage, categorizes it into one of the eight sectors, and chooses the appropriate coefficients for that sector. This technique was faster and more accurate than the higher-order polynomial approximation over the entire range.

47. A cantilever beam was used to calibrate the system for strain measurement. It was found that the relative error was less than 3 percent. Ice-water equilibrium mixture and boiling water were used to determine the system's error for temperature measurement. The absolute error was less than ±3 °F.

Infrared instrument

48. The Inframetrics Model 525 system was used to measure the surface temperature field during and after welding. This system has a -4 to 2,730 °F temperature measurement range and has four basic display functions:
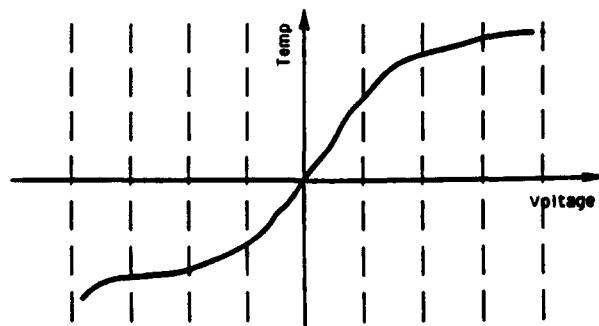
Figure 7. Thermocouple characteristic curve
divided into sections

<u>a</u>. <u>IMAGE</u> - normal picture with brightness indicating temperature difference and a calibrated gray scale.

<u>b</u>. <u>LINE SELECT</u> - normal picture is displayed with a brightened line indicating vertical position of the line scan that will be displayed in the line scan mode.

<u>c</u>. <u>LINE SCAN</u> - temperature versus horizontal position is displayed for a continuous horizontal scan fixed in the scene vertically by the line position potentiometer.

<u>d</u>. <u>ISOTHERM</u> - constant temperature contours are intensified over the normal image for selected temperature levels. A marker at the left of the display indicates the difference temperature as a fraction of the temperature for a given range set.

49. As the system is scanned, the naturally emitted infrared radiation is converted by a liquid, nitrogen cooled mercury, cadmium, telluride (HgCdTe) detector to an electrical signal that is processed into a TV picture of the temperature pattern in the scene. An ambient temperature chopper is viewed by this detector 60 times a second to DC restore the picture.

50. A calibrated grey scale is presented across the bottom of the picture in the normal imaging mode. In addition, there are two quantitative modes - Isotherm and Line scan. There are seven temperature-difference ranges with full-scale settings of 10, 20, 50, 100, 200, 500, and 1,500 °C. A zoom feature is also provided having 4:1 ratio. Figure 8 illustrates the infrared system with video tape recorder. The weld specimen is scanned by the scanner and the infrared signal is converted to a temperature field by the control/electronic units. The temperature field is displayed on the monitor and a video recorder can save all the temperature readings from the monitor. The testing setup for the infrared system is shown in Figure 9.

<u>Welding Procedure</u>

<u>Weld specimen preparation</u>

51. The test specimens were prepared using ASTM A-36 plate. The chemical compositions and mechanical properties of 1/2- and 1-in.-thick specimens specified in ASTM are given in Table 1 and Table 2, respectively.

52. A single-bevel butt joint was prepared for the 1/2-in.-thick plate with both single and double V-grooves made for the 1-in.-thick plate. The specimen sizes and joint details are shown in Figure 10 and Figure 11. To remove preexisting residual stresses, the 1-in.-thick plates were stress relieve annealed prior to welding.

25
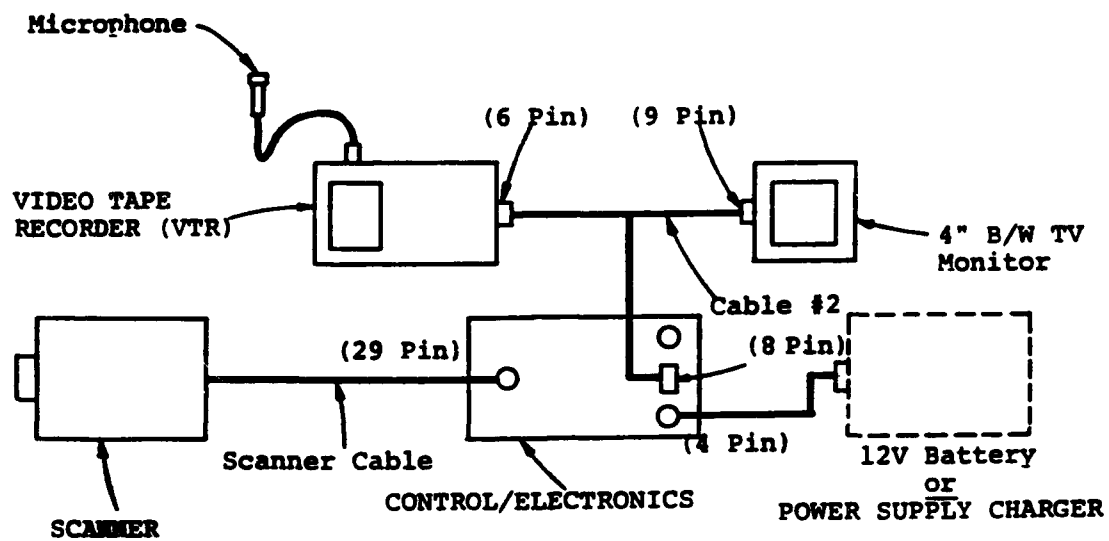
Figure 8. Schematic diagram of basic system with VTR
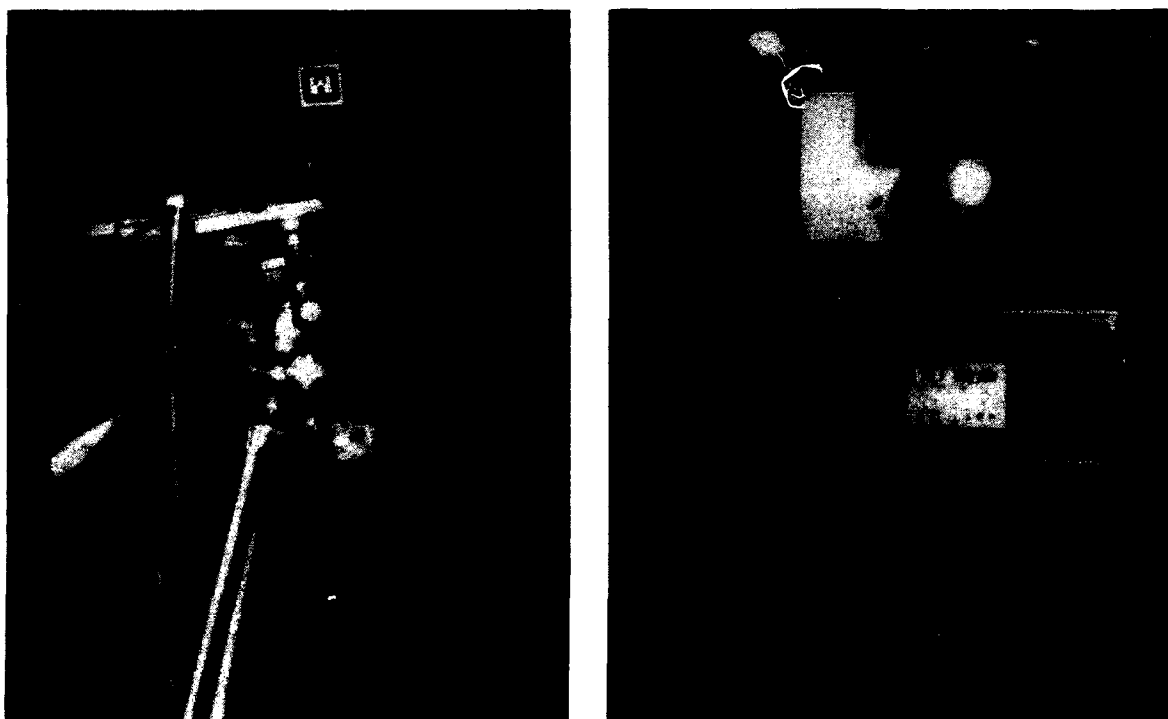
Figure 9. Testing setup of infrared system

26
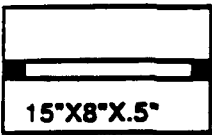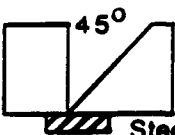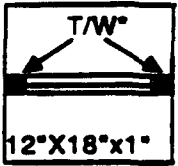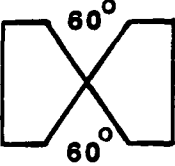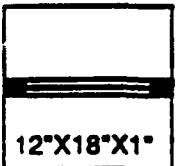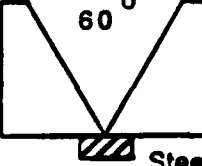
Table 1

Chemical Compositions of ASTM A-36 Steel (Maximum Values)

Plate Thickness	C, %	Mn, %	P, %	S, %
0.5 in.	0.25	--	0.04	0.05
1 in.	0.25	0.8-1.2	0.04	0.05

Table 2

Tensile Properties

Yield point (min):	36 ksi [250 Mpa]
Tensile strength:	58-80 ksi [400-550 Mpa]
elongation in 2 in. (min):	23 %

Test No.	Thick.	Groove	Dimensions of Specimen	Joint Details	Remarks
1 5	1/2"	Single Bevel (1/2V)	15"X8"X.5"	45° Steel Backing	
2 4	1.0"	Double V Groove	T/W° 12"X18"x1"	60° 60°	2:Stress Relief Anneal. before Welding
3	1.0"	Single V Groove	12"X18"X1"	60° Steel Backing	3:Stress Relief Anneal. before Welding

* T/W: Tack Welding

Figure 10. Dimensions of specimen and joint details
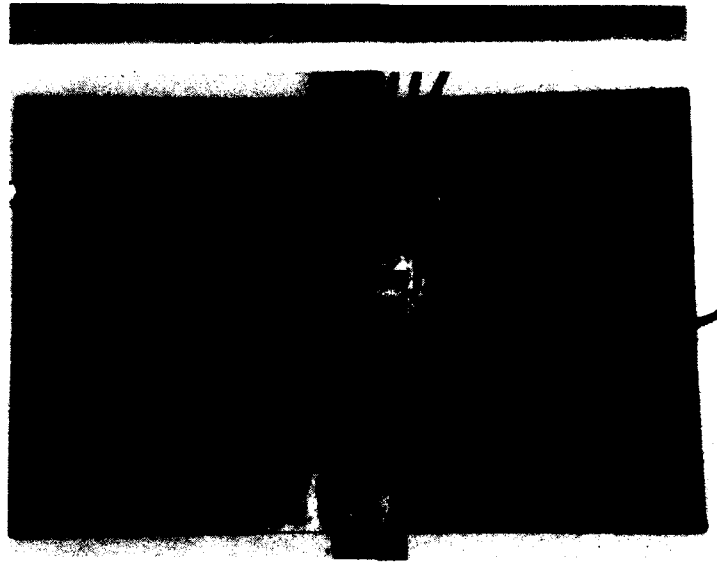
Figure 11. Shape of 1-in. specimen before
and after welding

53. Tack welds about 1.5 in. in length were made at both ends of the
plates and no presetting was provided prior to welding. After locally
polishing the surface of the specimens, thermocouples were attached. High-
temperature strain gages and plastic material for photoelasticity measurements
were also attached to the 1/2-in. specimens (Test No. 1).

Welding equipment and setups

54. A GMAW (MIG) system and BUG-O automatic traveling unit were com-
bined to make an automatic process system. A HOBART MEGA-MIG 450RVS unit was
used for power source and wire feed. To accurately measure heat input, a
volt-meter and ampere-meter were attached to the welding system. The equip-
ment setup is shown in Figure 12.

Welding procedures

55. Welding was performed using electrodes which conformed to American
Welding Society (AWS) specifications. These electrodes included 0.13 percent
carbon content, medium manganese content, and were silicon killed (American
Welding Society 1979). These electrodes had a tensile strength of approxi-
mately 75 ksi and a yield strength of approximately 63 ksi. Sheilding gas was

28
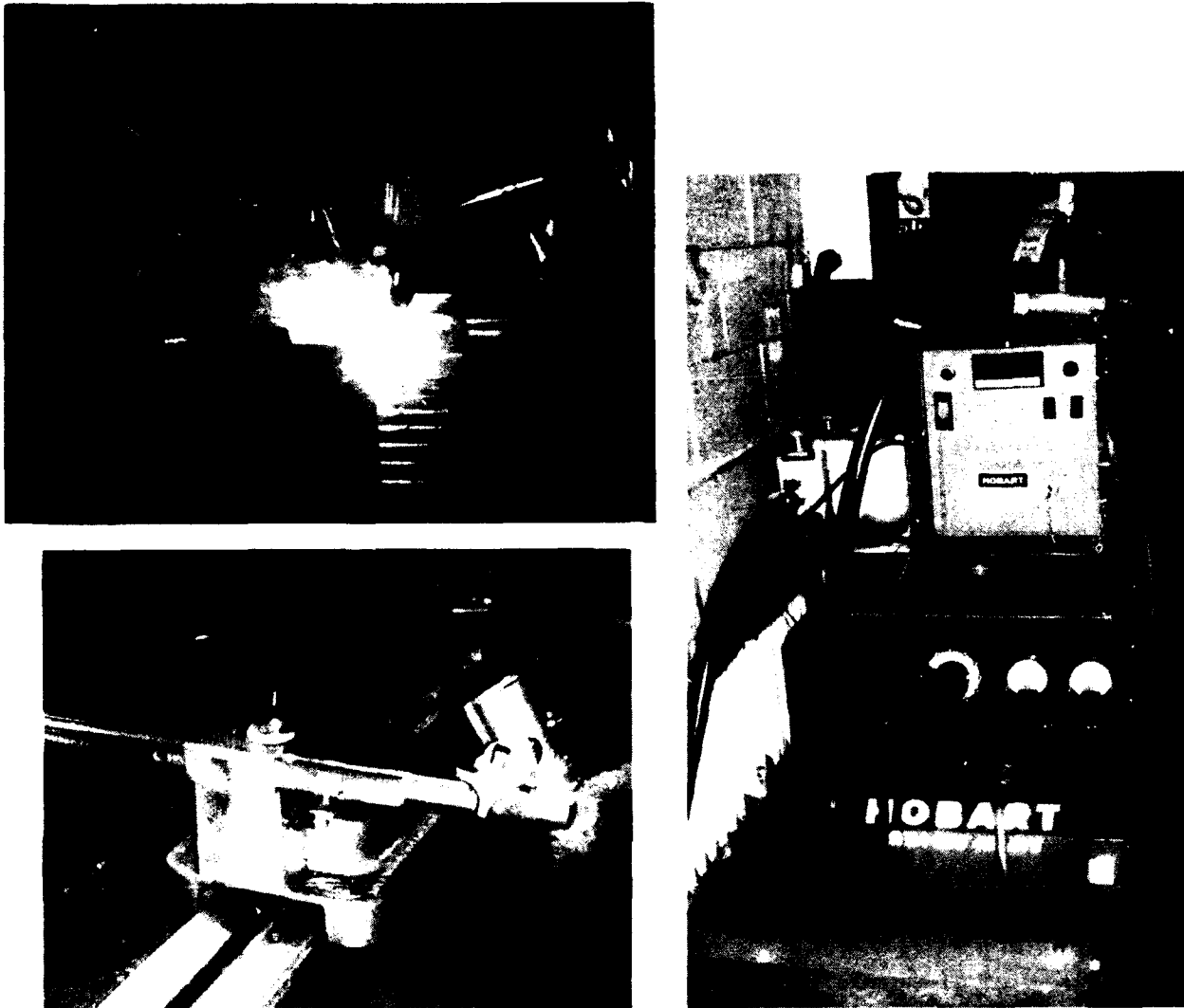
Figure 12. Welding equipment and traveling unit

composed of 98 percent agron and 2 percent oxygen gas and was given a flow
rate of 50 ft³/hr. The spray transfer mode was obtained during welding.

56. Welding procedure specifications (WPS) such as welding parameters,
preheat/interpass temperatures, and material specifications are given in
Table 3 and Table 4. The pass sequences and welding parameters of each pass
are shown in Table 5. The calculated heat input and deposit rate of weld
metal are also given in Table 5.

Table 3

WPS for Single V-groove Weld
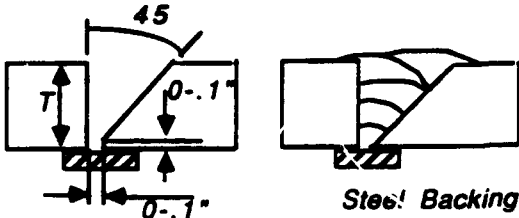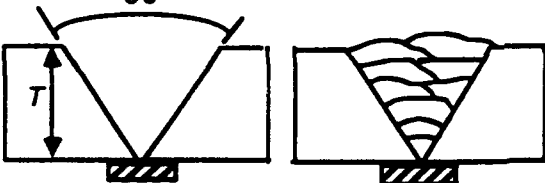
WELDING PROCEDURE SPECIFICATION				DATE: JAN.4,1989	
PROCESS	*GMAW*	WPS NO.	*GMAW-01*	POSITION: *1G(FLAT)*	
BASE METAL	*ASTM A36*			THICK. RANGE *3/8"<T<1 1/4"*	
CONSUMABLES	CLASS: E 70S-3 OR E70S-4 BRAND: FLOW RATE: SHIELDING GAS: 98%Ar-2%O2 50 ft3/hr				

JOINT DETAILS: SINGLE BEVEL OR V GROOVE	MIN. PREHEAT	DRYOUT (70 °F)
Steel Backing	INTERPASS TEMP.(MAX)	500 °F
	PWHT	NA

PASS	DIA. (in)	POL.	AMPS (A)	VOLTS (V)	SPEED (in/min)	REMARKS
ROOT	.045	DCRP	180-200	23-26	6-9	• STICK-OUT: .5" • WEAVING: STRAIGHT • TORCH ANGLE: 70 (PUSH ANGLE)
FILL & CAP	.045	DCRP	190-220	24-27	8-14	

NOTE	* STEEL BACKING * WELDING DIRECTION: SAME IN ALL PASSES	REV.: 0
		DATE: JAN.4,1989
		PREPARED BY: S.G.LEE

Table 4

WPS for Double V-Groove Weld
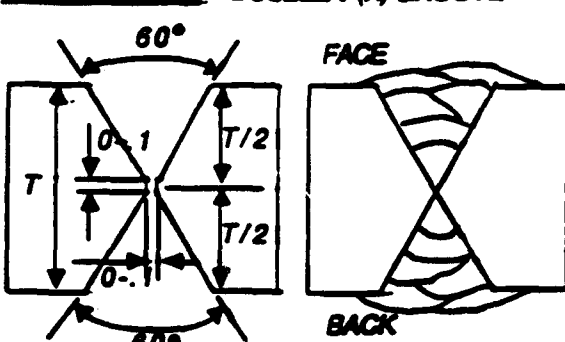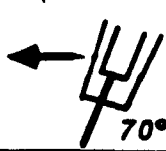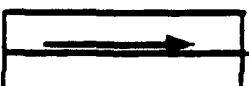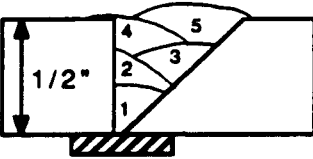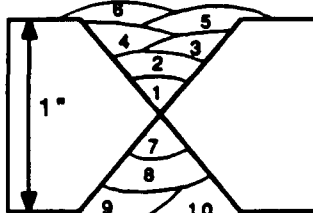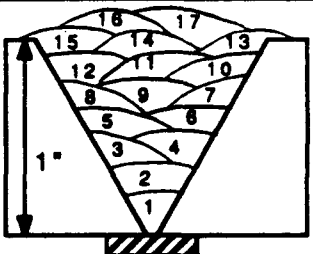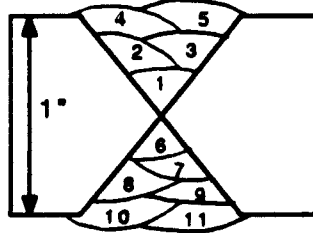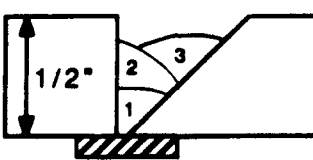
WELDING PROCEDURE SPECIFICATION				DATE: JAN.4,1989	
PROCESS	GMAW	WPS NO.	GMAW-02	POSITION: 1G(FLAT)	
BASE METAL	ASTM A36			THICK. RANGE	1/2" <T≤2"
CONSUMABLES	CLASS: E 70S-3 OR E70S-4 BRAND: SHIELDING GAS: 98%Ar-2%O2			FLOW RATE: 50 ft3/hr	

JOINT DETAILS: DOUBLE V (X) GROOVE

	MIN. PREHEAT	DRYOUT (70°F)
	INTERPASS TEMP.(MAX)	500°F
	PWHT	NA

PASS	DIA. (in)	POL.	AMPS (A)	VOLTS (V)	SPEED (in/min)	REMARKS
FACE						
ROOT	.045	DCRP	180 - 200	23-25	7-10	• STICK-OUT: .5" • WEAVING: STRAIGHT • TORCH ANGLE: 70° (PUSH ANGLE)
FILL & CAP	.045	DCRP	200 - 220	24-26	9-13	
BACK						
FILL & CAP	.045	DCRP	200 - 220	24-26	9-13	

NOTE	• STEEL BACKING • WELDING DIRECTION: SAME IN ALL PASSES	REV.: 0
		DATE: JAN.4,1989
		PREPARED BY: S.G.LEE

Table 5

Pass Sequences and Welding Parameters of Each Pass

Test No.	Pass Sequence	Pass No.	Welding Parameters			Heat Input (KJ/in)	Remarks
			Amp (I)	Volt (E)	Speed V(lpm)		
1	1/2"	1	215	24	14.4	18.3 *	
		2	205	25	14.4	18.2	
		3	215	26	14.4	19.8	
		4-5	210	24	14.4	17.9	
2	1"	1-2	200	24.2	7.7	32.1	Specimen:
		3-5	200	24.2	12.0	20.6	Annealed
		6	200	24.5	9.9	25.2	Before
		7-10	215	24.5	10.0	26.9	Welding
3	1"	1-2	195	24.5	6.6	34.8	Specimen:
		3-6	200	24.5	7.9	31.2	Annealed
		7-12	190	24.5	7.9	29.7	Before
		13	195	24.5	7.9	30.5	Welding
		14-17	190	24.8	6.6	34.3	
4	1"	1	190	25	7.9	30.7	
		2-5	215	26	11.1	25.7	
		6	190	25	7.9	30.7	
		7-9	220	26	11.1	26.3	
		10-11	250	27	11.1	29.8	
5	1/2"	1	205	25	11.1	23.5	Welding Stopped after 3 Passes
		2-3	215	26	11.1	25.7	

* HEAT INPUT = $\dfrac{60\,N\,E\,I}{V}$ WHERE ARC EFFICIENCY (N) = 85% FOR GMAW PROCESS

32

Temperature Measurement Results

Thermocouple method

57. Surface temperatures have been measured on 0.5- and 1-in.-thick plates using ANSI type K thermocouple. A discharging welding machine and a portable thermocouple attachment unit made by Cooperheat, Inc. (also based on the discharging method), were both used to attach the thermocouple to the specimen. Paragraphs 51 through 57 provide detailed information on welding conditions, such as welding parameters, welding processes, specimen and groove geometry, and heat input rates. The distances between the thermocouple and the groove edge of the weld were measured prior to the welding for all thermocouples. Except for those used in the thermal strain measurement (Test 5), all thermocouples were mounted around the middle of the transverse cross-section of the specimen as illustrated in Figure 13, even though the exact longitudinal distances from the side edges of the specimens were not recorded. Some experimental results are presented here, together with discussions on the accuracy of the experimental data. The relationship between the temperature distribution and the welding process as well as welding parameters is not considered in this chapter. More experimental temperature measurement results are presented when compared with the finite element analysis results (paragraphs 51 through 53).

1/2-in.-thick plate

58. A total of five passes were deposited on the 0.5-in.-thick plate (Test 1). The geometry of the weld beads is depicted in Figure 14 and given in Table 6. The welding conditions are presented in paragraphs 51 through 57. Three thermocouples were placed on the top surface of the specimen. Another thermocouple was attached on the bottom surface as shown in Figure 13.

59. The thermal cycles of all the passes were recorded using the data acquisition system. The first two passes are plotted in Figure 15, and the remaining three passes are plotted in Figure 16. The peak temperatures T_p and interpass temperatures T_o are shown in Table 7. The differences between T_p and T_o are shown in Figures 17 and 18. It should be noted that the first thermocouple was broken during the fourth pass due to high temperature.

60. It is clear, from these figures and tables, that the peak temperatures and the thermal responses of a given thermocouple vary from pass to pass. One of the reasons is that, for multipass welding, the thermal cycle at
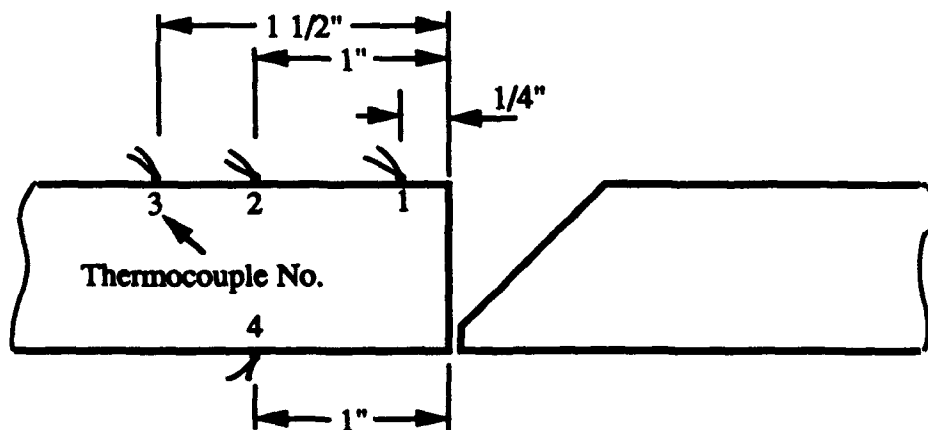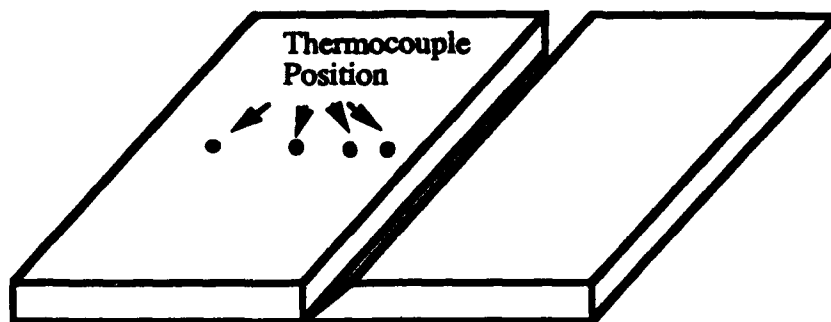
Note: Thermocouple 1 was broken during the final pass due to high temperature

Figure 13. Thermocouple layout for 1/2-in.-thick plate (Test 1)
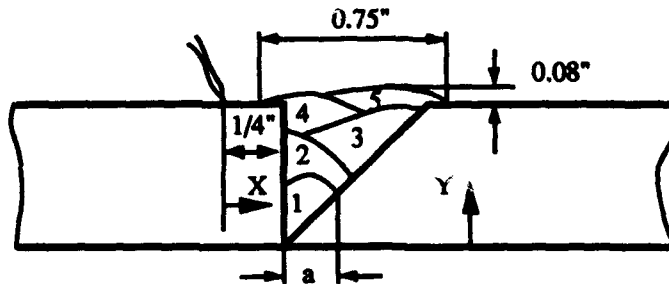
Figure 14. Geometry of weld beads of
1/2-in. welding specimen (Test 1)

Table 6

Geometry of Weld Beads on 1/2-in.-thick Plate (Test 1)

Pass No.	Bead Width (a), in.	Bead Height (Y), in.	Distance Between Thermocouple and Center of Weld Bead (X), in.
1	0.26	0.26	0.39
2	0.35	0.37	0.39
3	0.41	0.43	0.59
4	0.51	0.51	0.39
5	0.47	0.55	0.69
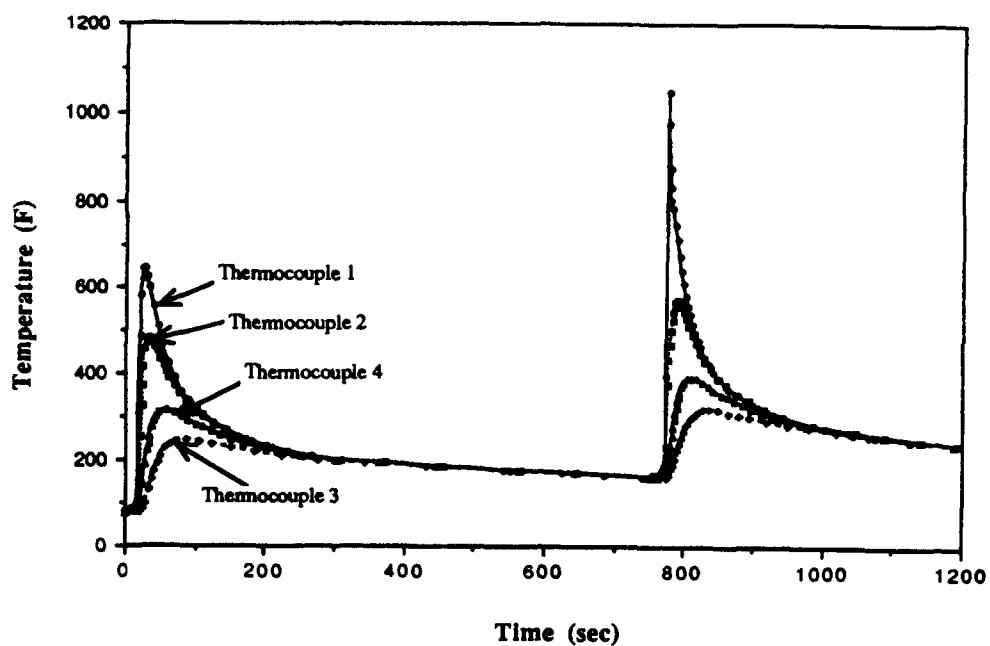
Figure 15. Temperature variations during the first two
passes on 1/2-in. plate (Test 1)
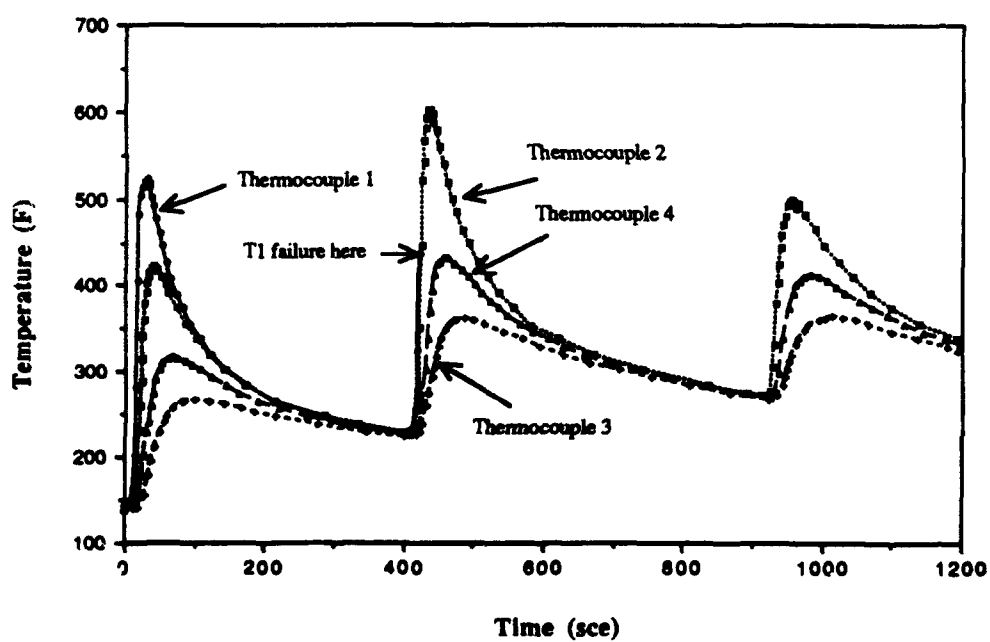
Figure 16. Temperature variations during the last three
passes on 1/2-in. plate (Test 1)

36

Table 7

Peak Temperatures as a Function of Thermocouple No. and Welding Pass (Test 1)

Channel No.	Peak Temp °F	Peak Time sec	Interpass °F	Pass No.	T_p-T_o °F
1	644	26.5	81	1	563
2	484	35	79	1	405
3	248	84.8	79	1	169
4	316	57.7	77	1	239
1	1,049	20.8	163	2	886
2	572	34.8	165	2	407
3	320	81.9	163	2	157
4	392	55.8	163	2	229
1	522	30.1	144	3	378
2	423	40.3	140	3	283
3	268	99.7	138	3	130
4	318	67.5	138	3	180
1	n/a*	n/a*	n/a*	4	n/a*
2	603	40.8	230	4	373
3	363	90	225	4	139
4	433	64.8	226	4	207
1	n/a*	n/a*	n/a*	5	n/a*
2	500	35.6	271	5	229
3	365	94	268	5	97
4	412	63.2	270	5	142

* Thermocouple #1 failed at the end of pass 3.
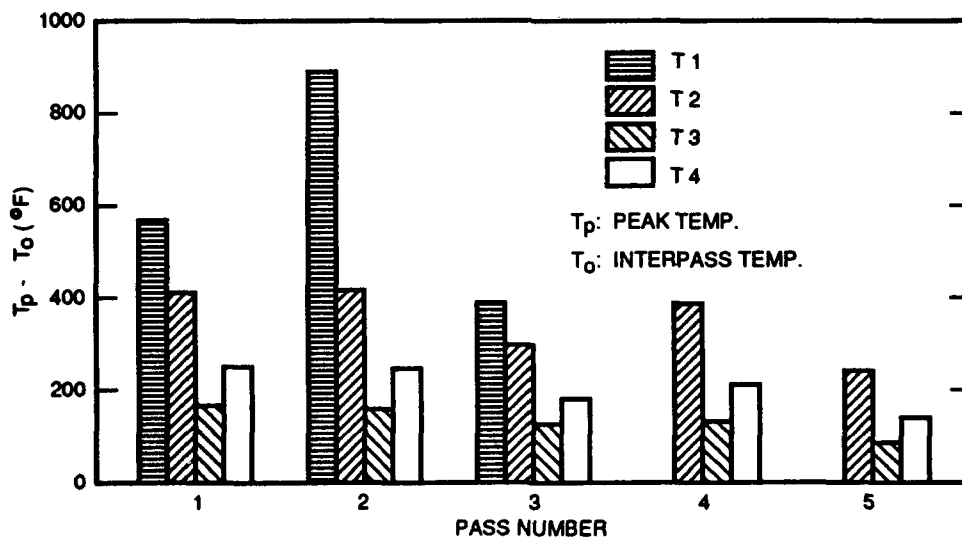
Figure 17. Peak temperatures of the 1/2-in. plate (Test 1)
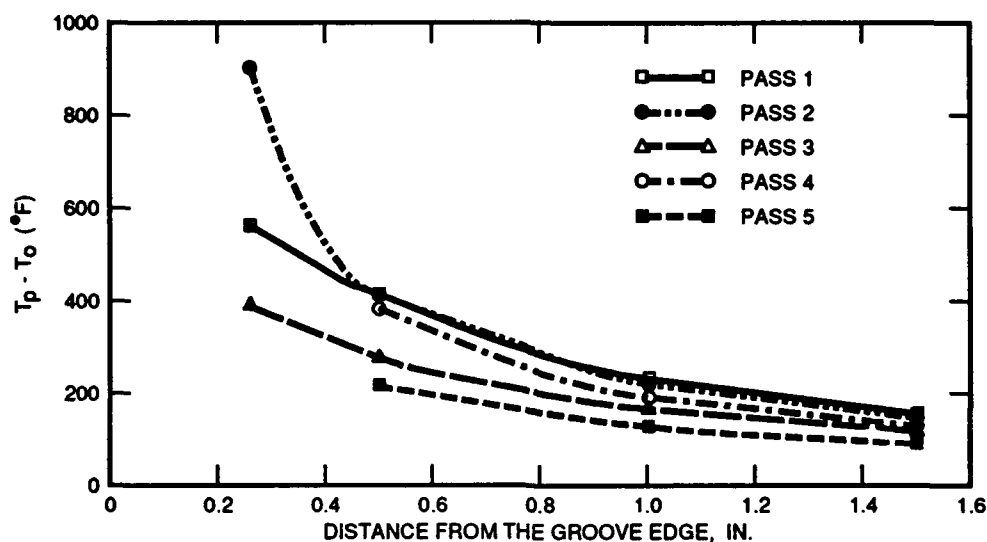
Figure 18. Peak temperature versus distance from the
groove edge in Test 1 (0.5-in.-thick, single V-groove)

a given position in the specimen is actually determined by its relative
distance to the weld bead which is being deposited.

1-in.-thick plate

61. Three tests were performed on the 1-in.-thick plates. Test 2 and
Test 4 were of the double V-groove type. Test 3 was a single V-groove type.
Test 2 was to evaluate the temperature measurement accuracy and repeatability
during welding by having two thermocouples at the same distance from the grove
edge. Test 3 was to measure the surface temperature changes for a single V-
groove specimen as a function of the distance from the weld. Test 4 was to
measure the surface temperature changes of a double V-groove specimen. All
tests were conducted using GMAW process.

62. In Test 2, two thermocouples were placed on the top surface of the
specimen at a distance of 1/4 in. from the groove edge, and the other two were
1 in. from the groove edge (Figure 19). This distance is not the distance
from the edge of weld bead. The latter varies from pass to pass. A total of
10 passes were deposited on the specimen. Figures 20 through 22 reveal the
temperature changes for passes 1, 5, and 10, respectively. These figures
represent various weld bead positions relative to the groove edge. The peak
temperature is shown in Figure 23 and Table 8.

38

TOP VIEW

Welding direction

SIDE VIEW
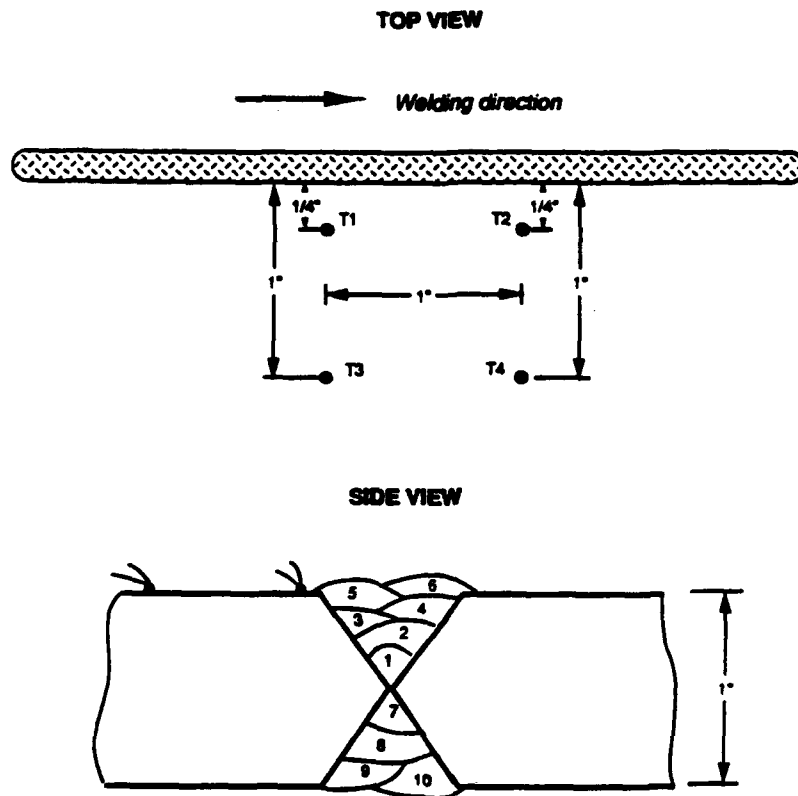
Note: Distance was measured from the groove edge rather than from the weld bead

Figure 19.   Thermocouple layout of Test 2 (1-in.-thick,
double V-groove)

63.   Six thermocouples were used in Test 3.   The thermocouple arrange-
ment is shown in Figure 24.   A total of 17 passes were required to complete
the joint.   The thermal history created by passes 1, 14, 15 and 17 is shown in
Figures 25 through 28.   Figure 29 and Table 9 present peak temperature as a
function of the distance from the groove edge.   Thermocouple T5 became inoper-
able during pass 16 due to high temperature.

64.   In Test 4, 11 passes were made on a 1-in.-thick double V-groove
plate.   Temperature changes were measured at 0.25, 0.5, 1, and 1.5 in. from
the groove edge (Figure 30).   Again, representative temperature variations
with respect to time are plotted in Figures 31 through 33 for passes 1, 5, and
11, respectively.   Thermocouple T1 and T2 can be compared to examine the

39
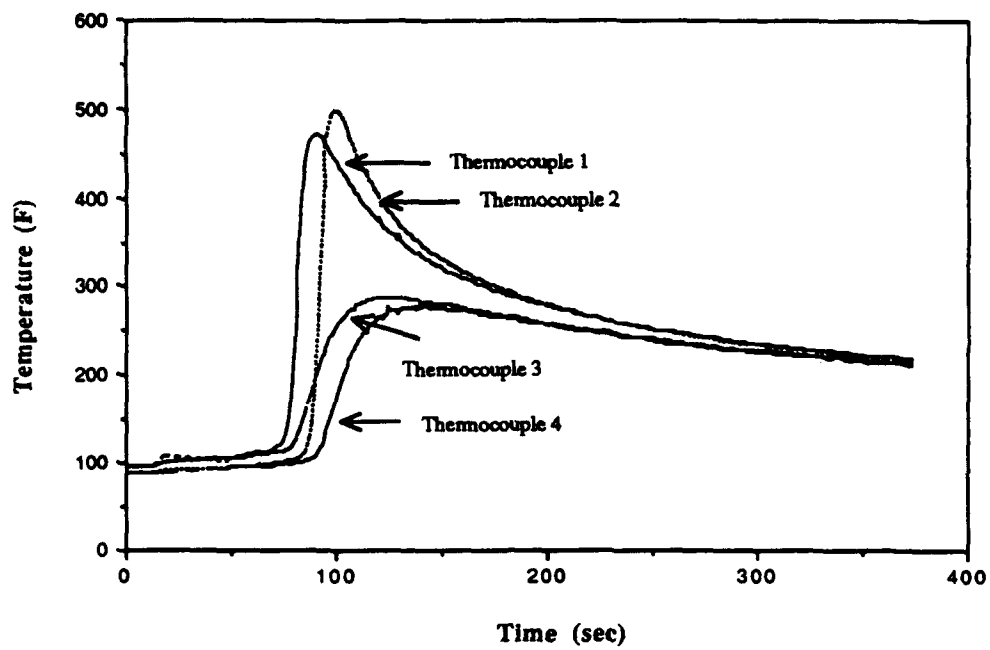
Figure 20.   Temperature versus time for Test 2, pass 1
             (1-in.-thick, double V-groove)
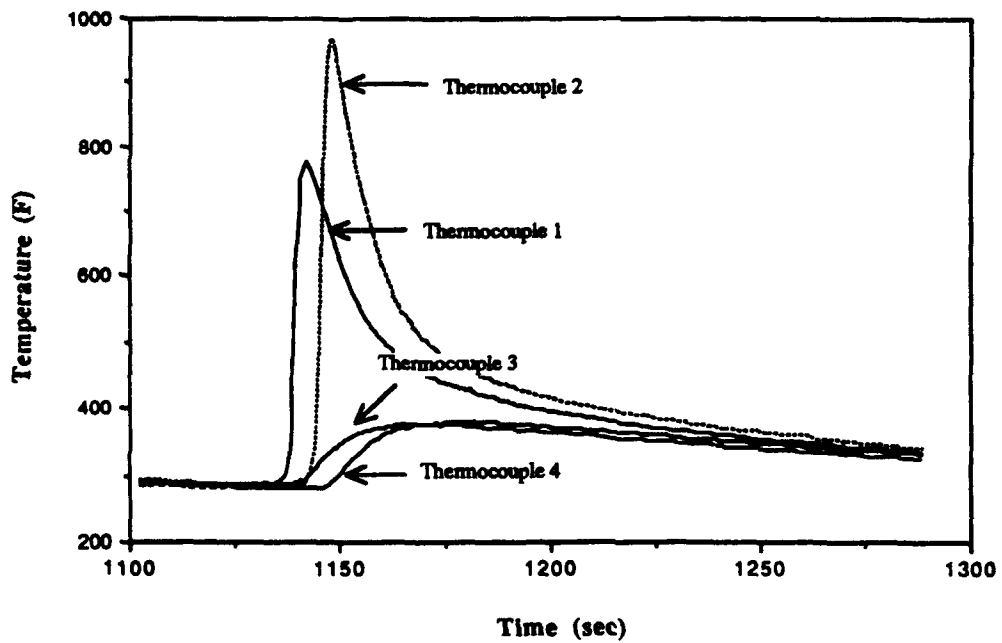
Figure 21.   Temperature versus time for Test 2, pass 5
             (1-in.-thick, double V-groove)
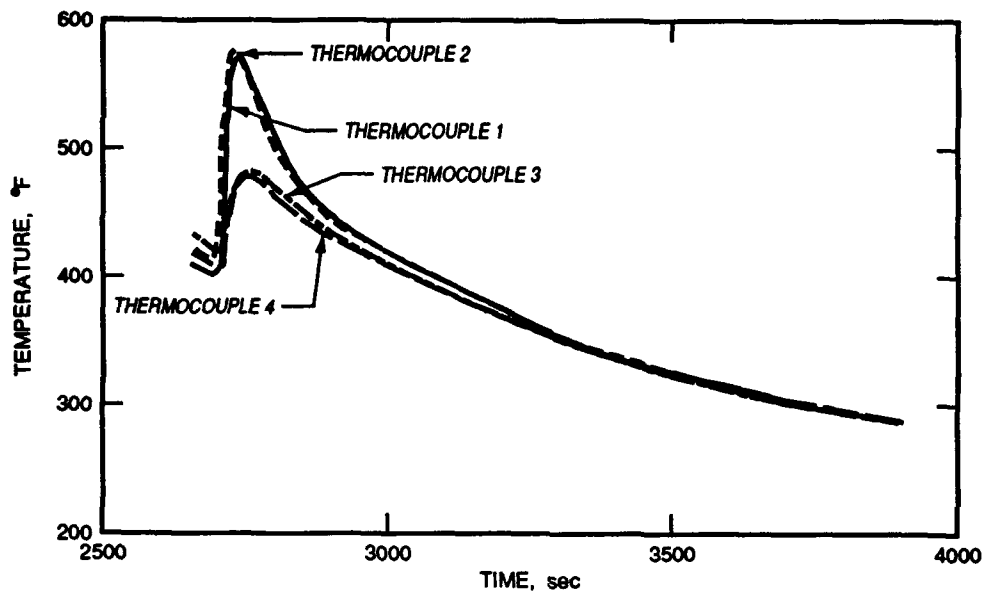
Figure 22.   Temperature versus time for Test 2, pass 10
(1-in.-thick, double V-groove)
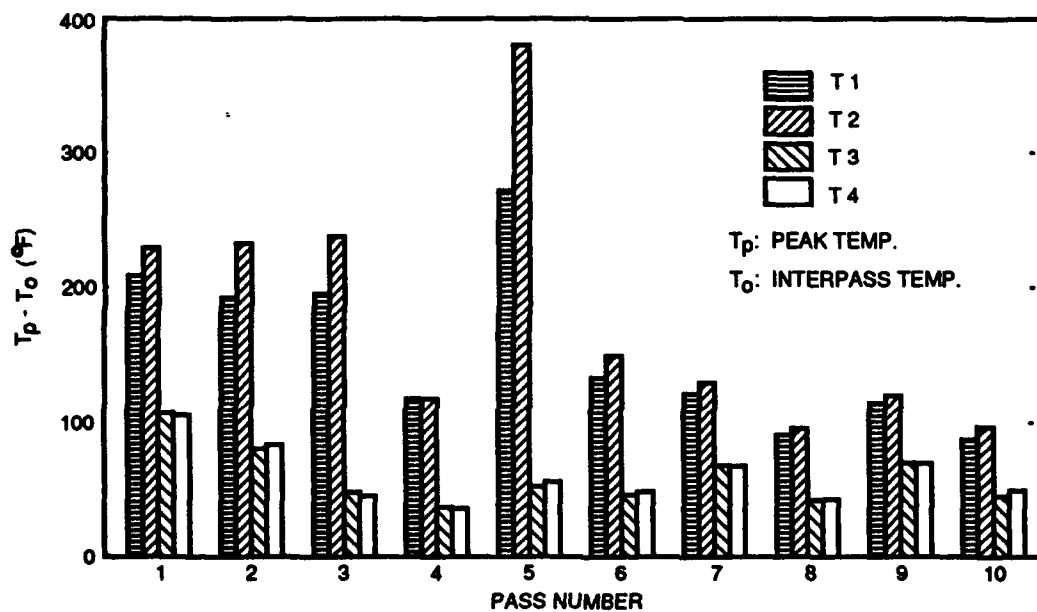
Figure 23.   Peak temperature as a function of passes (Test 2,
1-in.-thick, double V-groove)

41

Table 8

Peak Temperatures as a Function of Pass (Test 2, 1-in.-thick, double V-groove)

Couple No.	Peak Temp, T_p °F	Peak Time sec	Interpass, T_o °F	Pass No.	T_p-T_o °F
1	471	90.6	95	1	376
2	498	100.1	90	1	409
3	288	129	95	1	193
4	277	140.9	90	1	187
1	568	415.9	216	2	353
2	630	426.4	214	2	416
3	352	457.7	210	2	142
4	352	460.8	207	2	146
1	657	601.4	298	3	358
2	727	606.8	302	3	425
3	374	625.5	286	3	88
4	369	636.3	286	3	83
1	504	836.2	295	4	209
2	509	842.7	297	4	212
3	356	868.2	286	4	70
4	354	876.3	286	4	68
1	775	1,142	286	5	490
2	966	1,148	284	5	682
3	374	1,171	280	5	94
4	378	1,181	279	5	99
1	572	1,330	329	6	243
2	606	1,339	333	6	274
3	406	1,368	320	6	86
4	406	1,378	320	6	86
1	523	1,769	306	7	218
2	545	1,759	311	7	234
3	415	1,796	300	7	115
4	419	1,789	304	7	115
1	572	1,886	415	8	157
2	585	1,878	419	8	166
3	469	1,907	392	8	77
4	469	1,899	392	8	77
1	532	2,525	327	9	205
2	540	2,516	324	9	216
3	442	2,549	324	9	119
4	437	2,538	320	9	117
1	565	2,730	414	10	151
2	574	2,721	408	10	166
3	482	2,756	401	10	81
4	478	2,741	396	10	183

TOP VIEW

Welding direction

1/4"

T1 T5 1/4"

1/2" 1/2"

3/4" 1"

T2 T6

1 1/4"

T3

T4

SIDE VIEW
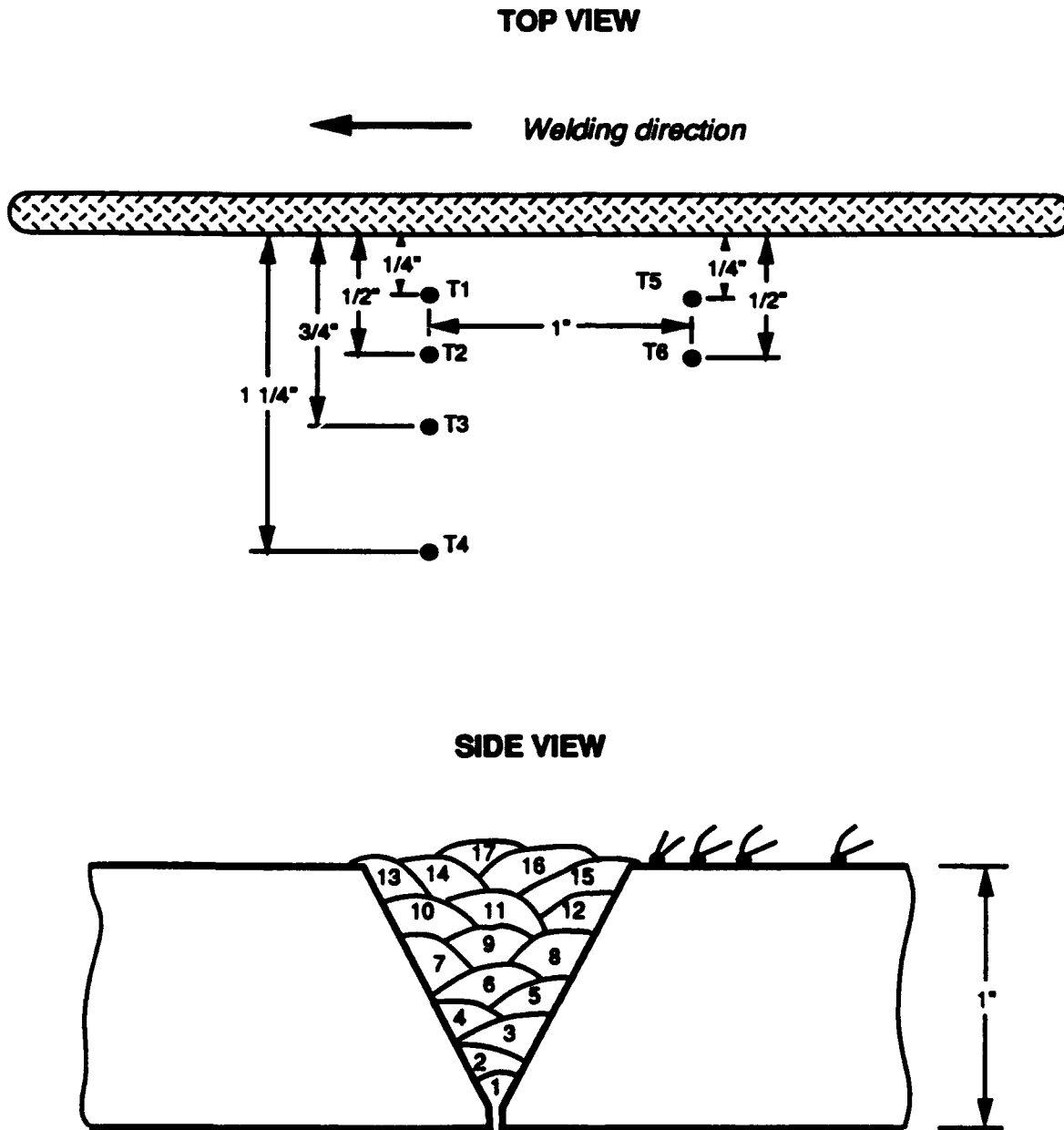
Note: Distance was measured from the groove edge rather than from the weld bead

Figure 24.   Thermocouple layout in Test 3, (1-in.-thick, single V-groove)
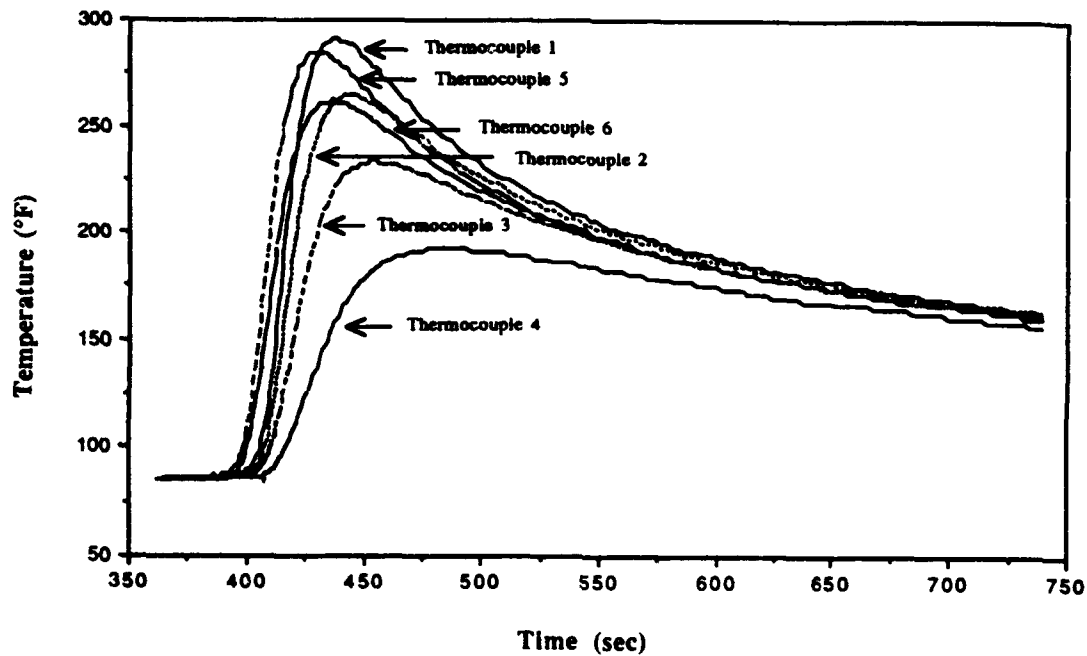
Figure 25. Temperature versus time in Test 3, pass 1 (1-in.-thick, single V-groove)
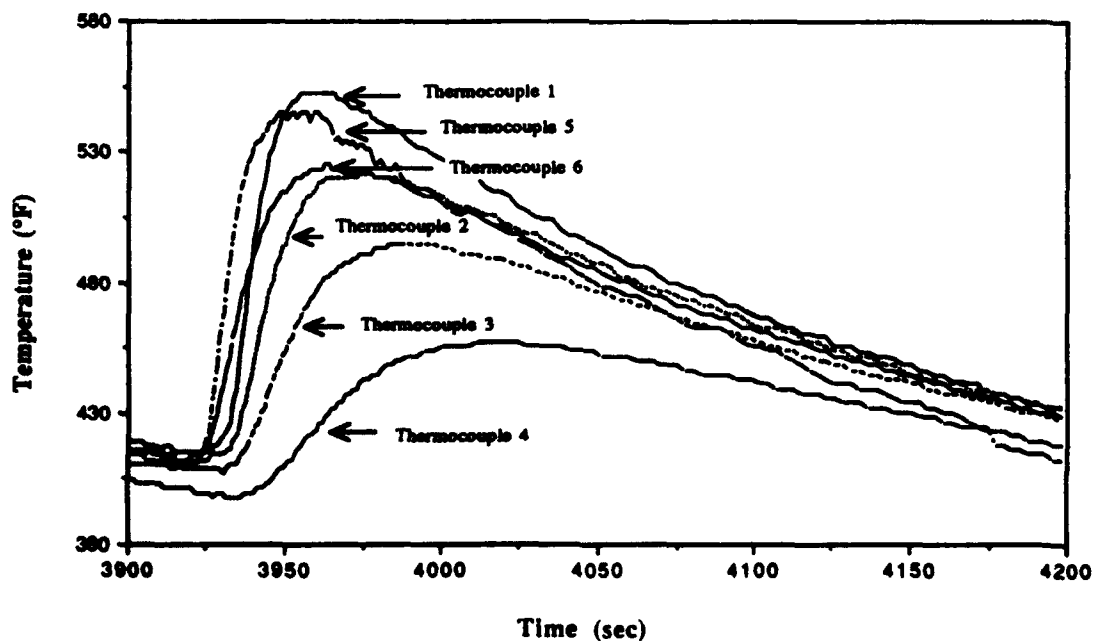
Figure 26. Temperature versus time in Test 3, pass 14 (1-in.-thick, single V-groove)

44
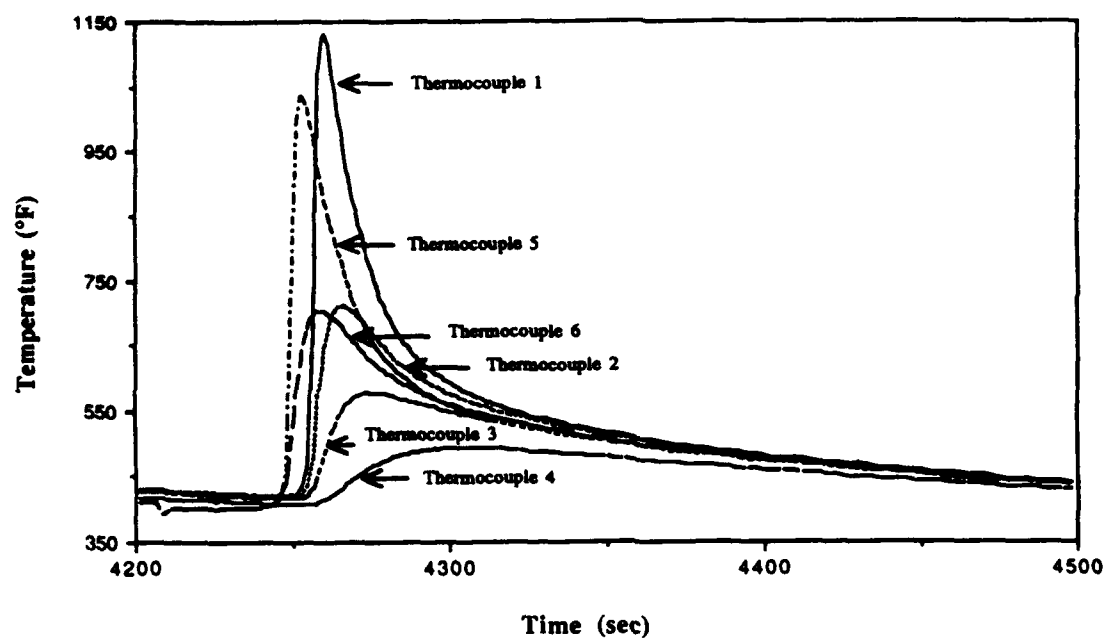
Figure 27. Temperature versus time in Test 3, pass 15
(1-in.-thick, single V-groove)
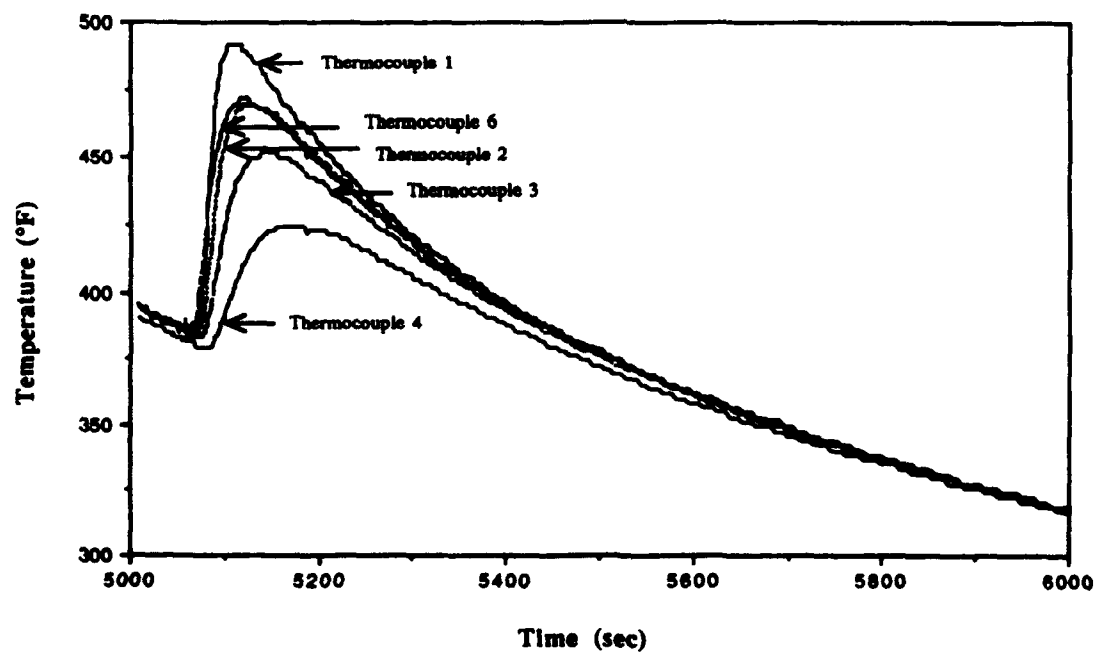
Figure 28. Temperature versus time in Test 3, pass 17
(1-in.-thick, single V-groove)
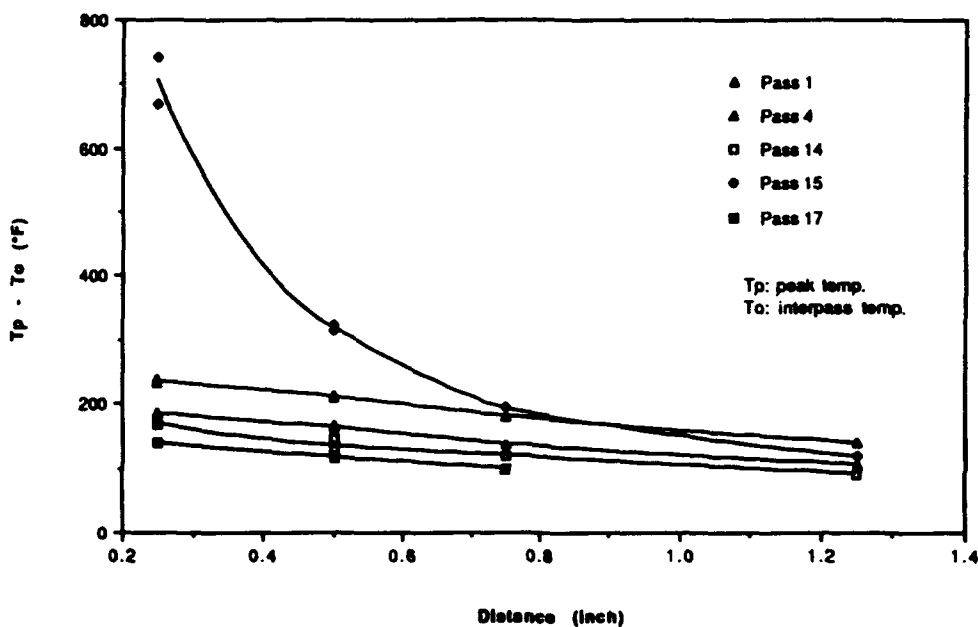
Figure 29. Peak temperature versus distance from the groove
edge in Test 3 (1-in.-thick, single V-groove)

repeatability of the measurement. The peak temperature as a function of
distance measured from the groove edge and welding pass are given in Figure 34
and Table 10.

65. From these results, satisfactory and repeatable temperature mea-
surement by the thermocouple method generally can be obtained when the thermo-
couple is about 0.5 in. or farther away from the weld fusion line. However,
unrepeatable results often appear for thermocouples placed within 0.5 in. from
the fusion line. Within this range, slight changes in position could
dramatically change the peak temperature. This can be seen from the plots of
peak change in temperature (peak temp-interpass temp) (T_p-T_o) versus distance,
such as Figure 34. There are several possible reasons for this variation.
First, it is practically impossible to attach two thermocouples at exactly the
same distance from the groove edge. Since the peak temperature is very sensi-
tive to the position near the fusion line, minor variation in locating the
thermocouple from the groove edge could result in significant difference in
peak temperature. This factor makes the peak temperature of one thermocouple
higher than the other, i.e. a shift in peak temperatures for all passes.
Another more important factor is that the weld fusion line is somewhat
irregular as shown in Figure 35. Thus, even though two thermocouples

46

Table 9

Peak Temperature as a Function of Thermocouple No. and Welding Pass (Test 3, 1-in.-thick, Single V-groove

Couple No.	Peak Temp, T_p °F	Interpass, T_o °F	Pass No.	T_p-T_c °F
1	291	84	1	207
2	264	84	1	180
3	234	84	1	149
4	192	84	1	108
5	284	84	1	200
6	262	84	1	178
1	340	162	2	178
2	315	162	2	153
3	286	160	2	126
4	246	154	2	92
5	336	160	2	176
6	316	160	2	157
1	441	212	3	229
2	401	210	3	191
3	358	208	3	149
4	302	201	3	101
5	428	208	3	220
6	396	210	3	185
1	405	250	4	155
2	379	246	4	133
3	352	246	4	106
4	313	239	4	74
5	396	244	4	151
6	378	248	4	130
1	552	289	5	263
2	489	264	5	225
3	435	284	5	151
4	372	275	5	97
5	538	286	5	252
6	484	288	5	196
1	491	354	6	137
2	466	352	6	113
3	435	347	6	88
4	390	333	6	58
5	484	351	6	133
6	464	352	6	112

(Continued)

Note: Thermocouple No. 5 was broken after the fifteenth pass.

(Sheet 1 of 3)

47

Table 9. (Continued)

Couple No.	Peak Temp, T_p °F	Interpass, T_o °F	Pass No.	T_p-T_o °F
1	399	311	7	88
2	385	311	7	74
3	369	307	7	61
4	343	302	7	41
5	394	307	7	86
6	385	311	7	74
1	642	340	8	302
2	536	340	8	196
3	469	334	8	135
4	410	325	8	85
5	622	336	8	286
6	531	338	8	193
1	496	381	9	115
2	473	379	9	94
3	448	376	9	72
4	410	363	9	47
5	491	376	9	115
6	473	379	9	94
1	460	399	10	61
2	448	397	10	50
3	430	392	10	38
4	403	379	10	23
5	453	396	10	58
6	448	397	10	50
1	520	399	11	121
2	491	397	11	94
3	466	392	11	74
4	428	379	11	49
5	509	390	11	119
6	491	397	11	94
1	673	403	12	270
2	563	401	12	162
3	507	396	12	112
4	453	387	12	67
5	664	397	12	266
6	570	399	12	171

(Continued)

(Sheet 2 of 3)

Table 9. (Concluded)

Couple No.	Peak Temp, T_p °F	Interpass, T_o °F	Pass No.	T_p-T_o °F
1	480	419	13	61
2	468	417	13	50
3	451	414	13	38
4	426	403	13	23
5	469	412	13	58
6	466	417	13	49
1	552	415	14	137
2	522	410	14	112
3	495	406	14	88
4	457	406	14	51
5	545	408	14	137
6	525	412	14	113
1	1,132	421	15	711
2	711	419	15	292
3	577	415	15	162
4	493	406	15	86
5	1,035	397	15	637
6	702	419	15	283
1	678	428	16	250
2	577	426	16	151
3	527	423	16	104
4	480	415	16	65
5	n/a	n/a	n/a	n/a
6	574	426	16	148
1	491	383	17	108
2	469	385	17	85
3	451	383	17	68
4	424	379	17	45
5	n/a	n/a	n/a	n/a
6	471	385	17	86

(Sheet 3 of 3)

TOP VIEW

Welding direction

SIDE VIEW
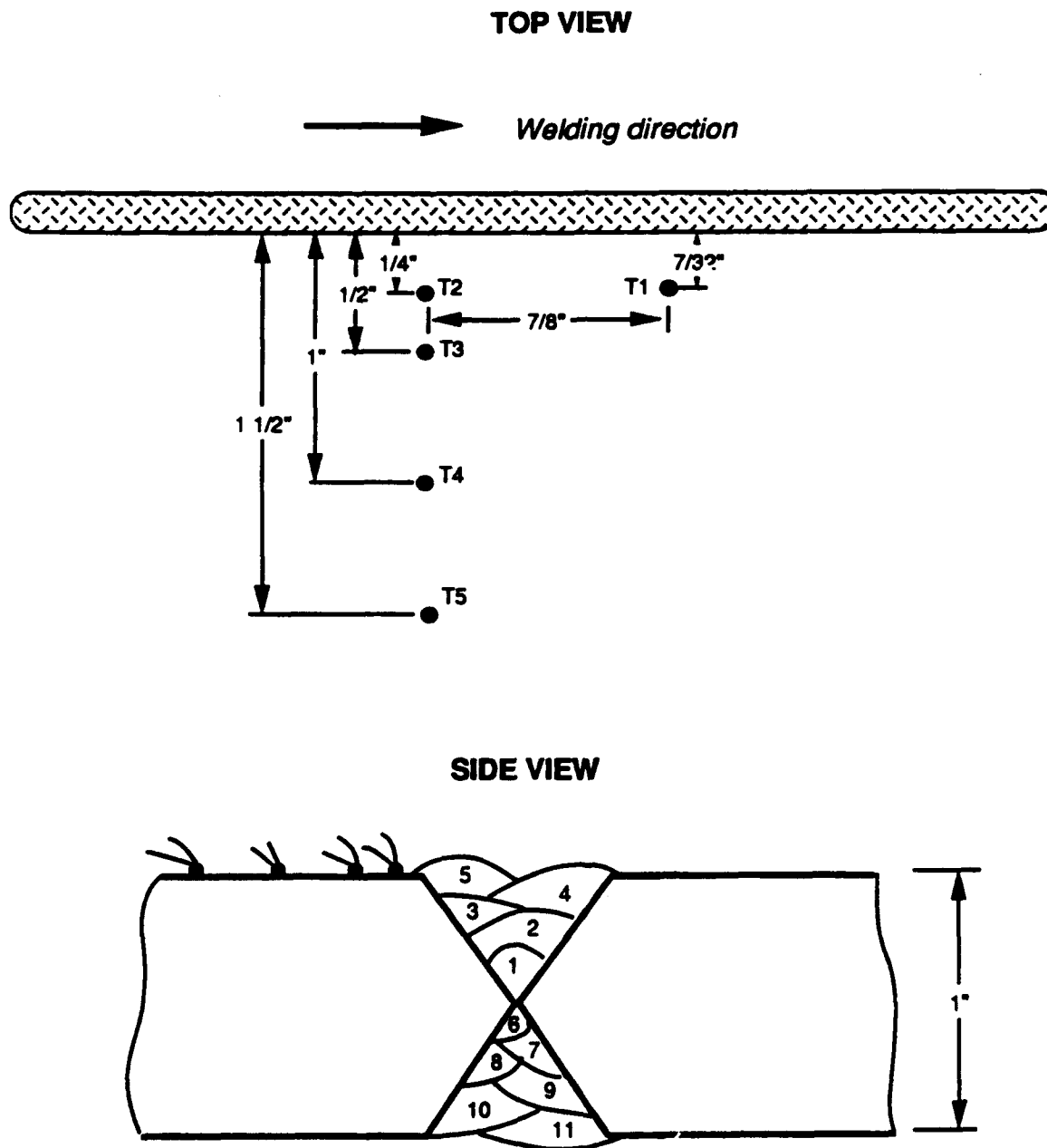
Note: Distance was measured from the groove edge rather than from the weld bead

Figure 30.   Thermocouple layout in Test 4 (1-in.-thick, double V-groove)
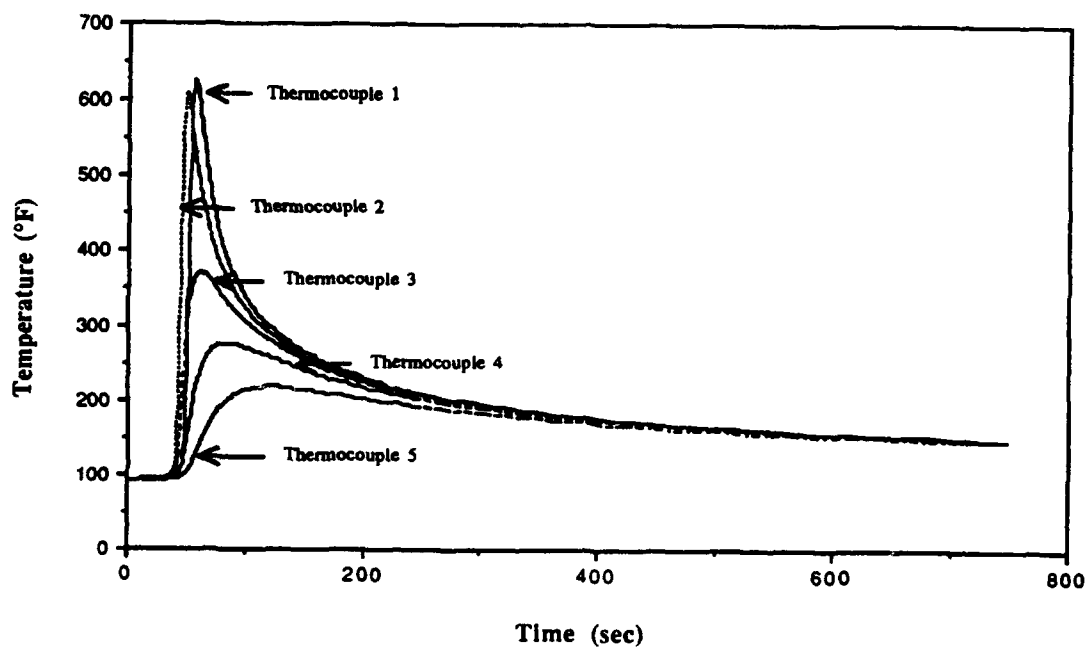
Figure 31. Temperature versus time in Test 4, pass 1 (1-in.-thick, double V-groove)
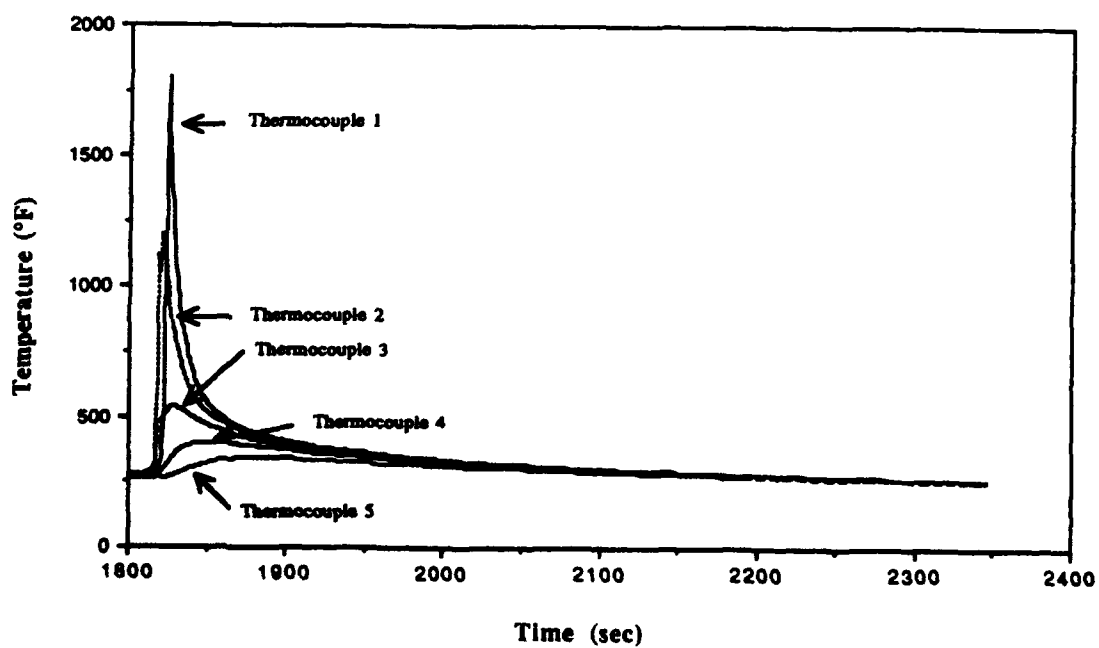
Figure 32. Temperature versus time in Test 4, pass 5 (1-in.-thick, double V-groove)

51
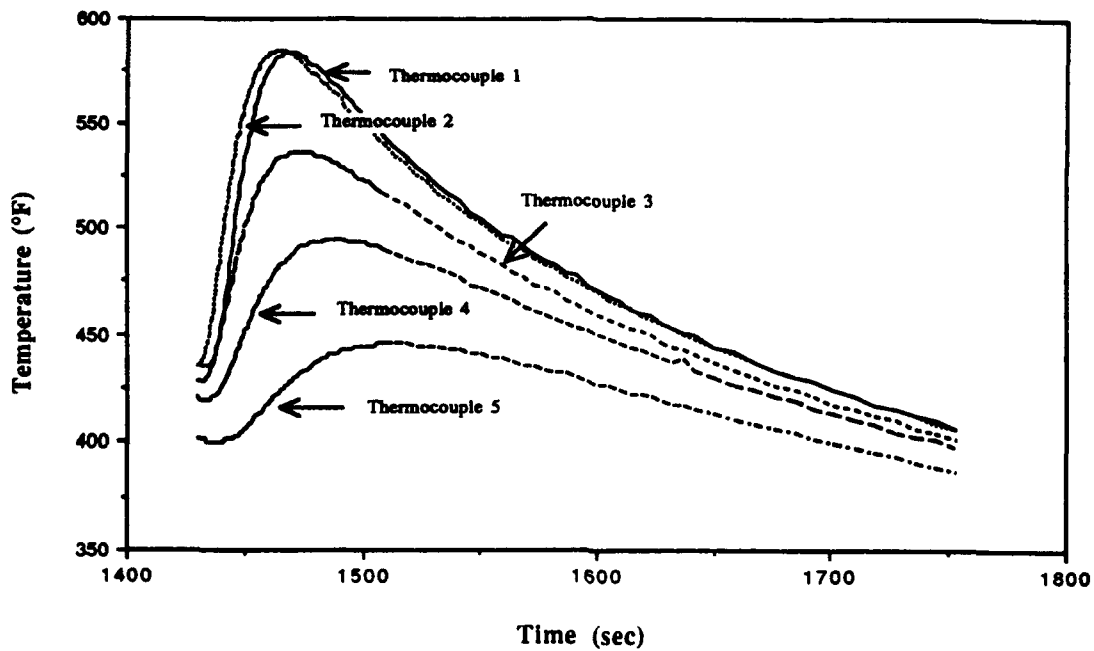
Figure 33. Temperature versus time in Test 4, pass 11 (1-in.-thick, double V-groove)
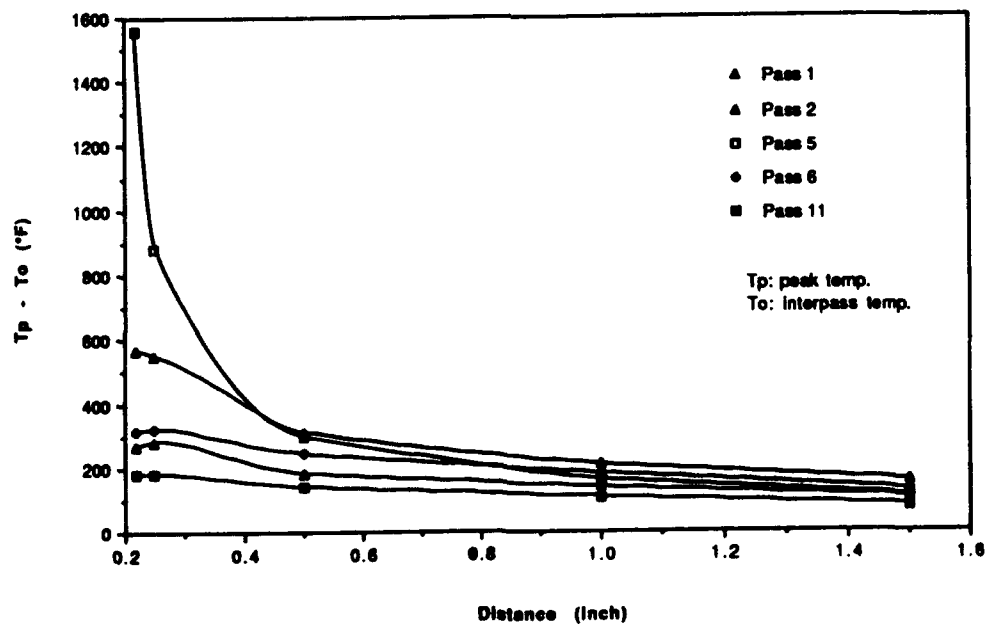
Figure 34. Peak temperature versus distance from the groove edge (Test 4, 1-in.-thick, double V-groove)

Table 10

Peak Temperature as a Function of Thermocouple No. and Welding Pass (Test 4,
1-in. plate, double V-groove

Couple No.	Peak Temp, T_p °F	Interpass, T_o °F	Pass No.	$T_p - T_o$ °F
1	626	91	1	535
2	608	91	1	517
3	370	91	1	279
4	275	91	1	178
5	217	91	1	126
1	383	147	2	236
2	397	147	2	250
3	298	147	2	151
4	253	147	2	106
5	219	145	2	74
1	545	192	3	353
2	572	192	3	380
3	372	192	3	180
4	311	192	3	119
5	268	190	3	77
1	464	239	4	225
2	592	235	4	356
3	365	235	4	130
4	320	234	4	86
5	284	228	4	56
1	1,805	279	5	1,526
2	1,126	275	5	851
3	540	273	5	266
4	399	268	5	131
5	338	259	5	79
1	507	223	6	284
2	513	223	6	290
3	435	223	6	212
4	372	223	6	149
5	318	221	6	97
1	460	253	7	207
2	464	253	7	211
3	405	252	7	153
4	361	252	7	110
5	320	248	7	72

(Continued)

Table 10. (Concluded)

Couple No.	Peak Temp, T_p °F	Interpass, T_o °F	Pass No.	T_p-T_o °F
1	532	309	8	223
2	534	311	8	223
3	478	307	8	171
4	426	304	8	122
5	370	293	8	77
1	522	365	9	157
2	523	365	9	158
3	475	360	9	115
4	433	354	9	79
5	390	340	9	50
1	590	367	10	223
2	594	369	10	225
3	541	363	10	178
4	487	360	10	128
5	428	349	10	79
1	583	435	11	148
2	585	435	11	149
3	536	495	11	108
4	495	419	11	76
5	446	399	11	47

Figure 35. Weld fusion line shows irregular pattern (Test 4)

originally have the same distance from the groove edge, their actual distance from the fusion line would not be the same. For these reasons, experimental differences in peak temperatures would be expected as the thermocouples neared the fusion line.

Infrared method

66. The infrared temperature measurement system along with a video tape recorder were used to verify the thermocouple results. The temperature profile in the line scan mode and isotherm mode were recorded on video tape. The infrared measurement system gives qualitative information about the surface temperature profile. Temperature measurement errors are due to surface conditions such as roughness and slag covering. Surface roughness and slag covering can affect the light emissivity. Therefore, precise quantitative temperature values cannot be obtained by this method.

Thermal Strain Measurement Results

67. The measurement of thermal strain during welding was conducted in Test 5 on a 1/2-in.-thick ASTM A-36 steel. Detailed welding information is given in paragraphs 51 through 57. The strain gages used in the test were

55

manufactured by Measurement Group, Inc., and were of the three-gage 45-deg
rosette type (WK-06-062RB-350) made from K type alloy. This strain gage type
is suitable for moderately high temperature use. The manufactures recommended
strain gage attachment procedures strictly followed.

68. Two strain gage rosettes were used in the test as shown in
Figure 36. Rosette 1 was placed 1/2 in. from the groove edge, while Rosette 2
was placed 1 in. from the groove edge. Because of testing difficulties, valid
data were obtained only for the first three passes with Rosette 2. Valid data
for Rosette 1 were obtained for the first 50 sec of welding time of the first
pass. Through use of the data acquisition system, both strain and temperature
changes at the same position were recorded. Corrections were made using a
computer program to compensate for temperature effects on the thermal strain
data. Figure 37 and Figure 38 provide the thermal strain information obtained
from the initial 50 sec of the first pass, together with the temperature
information at the testing positions. At 50.7 sec after the testing was ini-
tiated, Rosette 1 was split from the specimen. This triggered the data acqui-
sition system down. Thus, only the data in the first 50 sec were recorded.
In passes 2 and 3, only Rosette 2 was available. The thermal strain and tem-
perature as functions of welding time are presented in Figure 39 for pass 2.

69. From these plots, it can be seen that a great variance in longitu-
dinal strain (gages G3 and G4) and transverse strain (gages G1 and G6) exists
within a distance of 1/2-in. between the two rosettes. These steep strain or
stress variances will be further investigated in the numerical analysis.

Residual Stress Measurement Results

70. Residual stresses after welding were measured on both the 1/2- and
1-in. plates, with more emphases being placed on the thicker 1-in. plates.
Several tests were first conducted to evaluate the thermal stresses from pro-
longed strain gage heating (Test A), the machining stresses due to blind hole
drilling (Test C), and the residual stresses prior to welding (Test B). These
tests and the results are discussed in detail in this section.

71. The strain gages used were designed and manufactured for the blind
hole drilling method by Measurement Group, Inc. (gage pattern: EA-06-062RE-
120). A high-speed air turbine drill was used to reduce the drilling induced
stress. The manufactures recommended that strain gage installation procedures

TOP VIEW

← *Welding direction*

0.25"
0.5" ● T1
0.5"
0.25"
T4 ◉

G3
● T2
Rosette 1
G1 G2

1"
1"
1"

G4
● T3
Rosette 2
G5 G6
T5 ◉

7.2" from the edge ⟶

7.5" from the edge ⟶

8.5" from the edge ⟶

SIDE VIEW
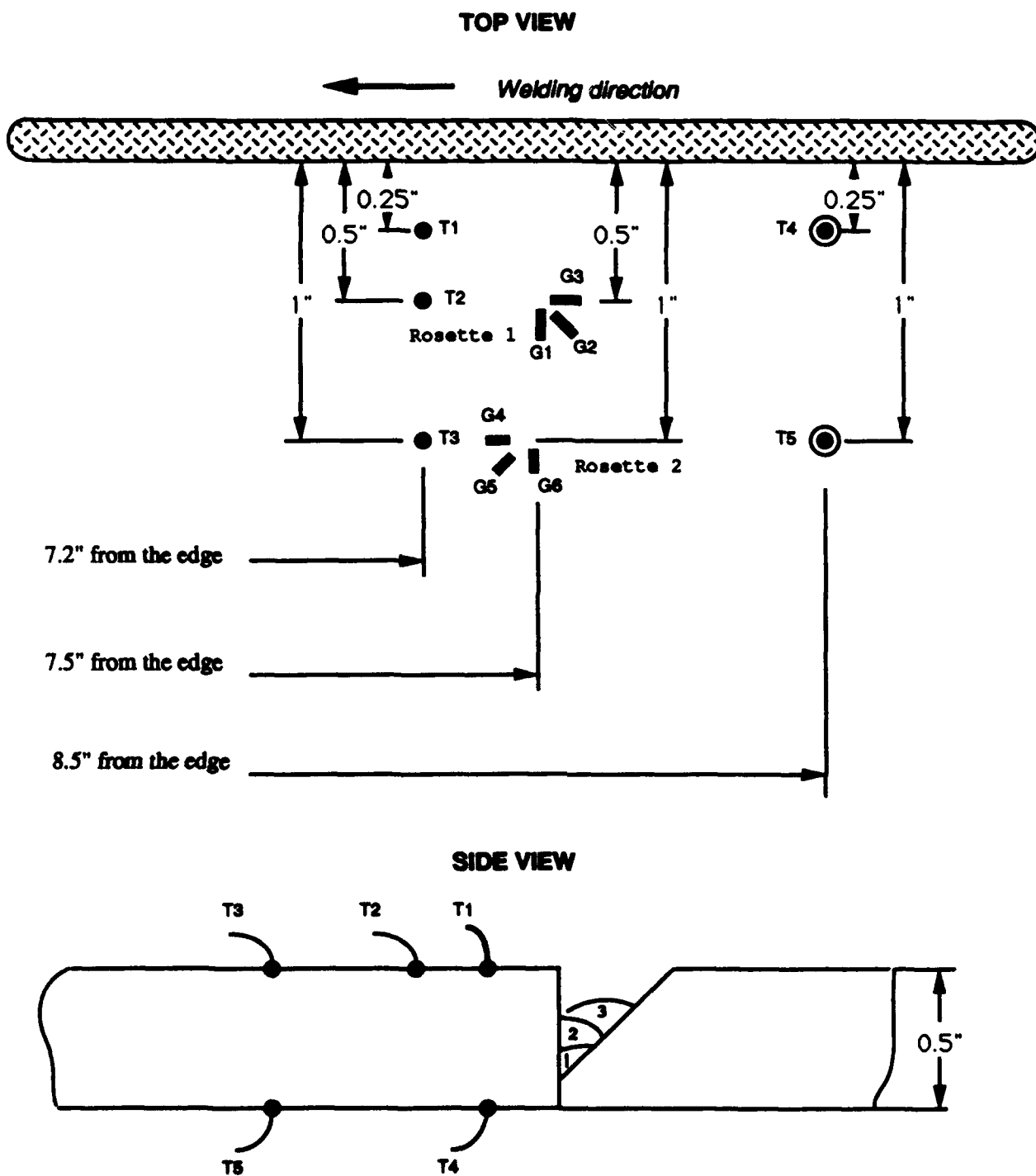
T3   T2   T1

3
2
1
0.5"

T5   T4

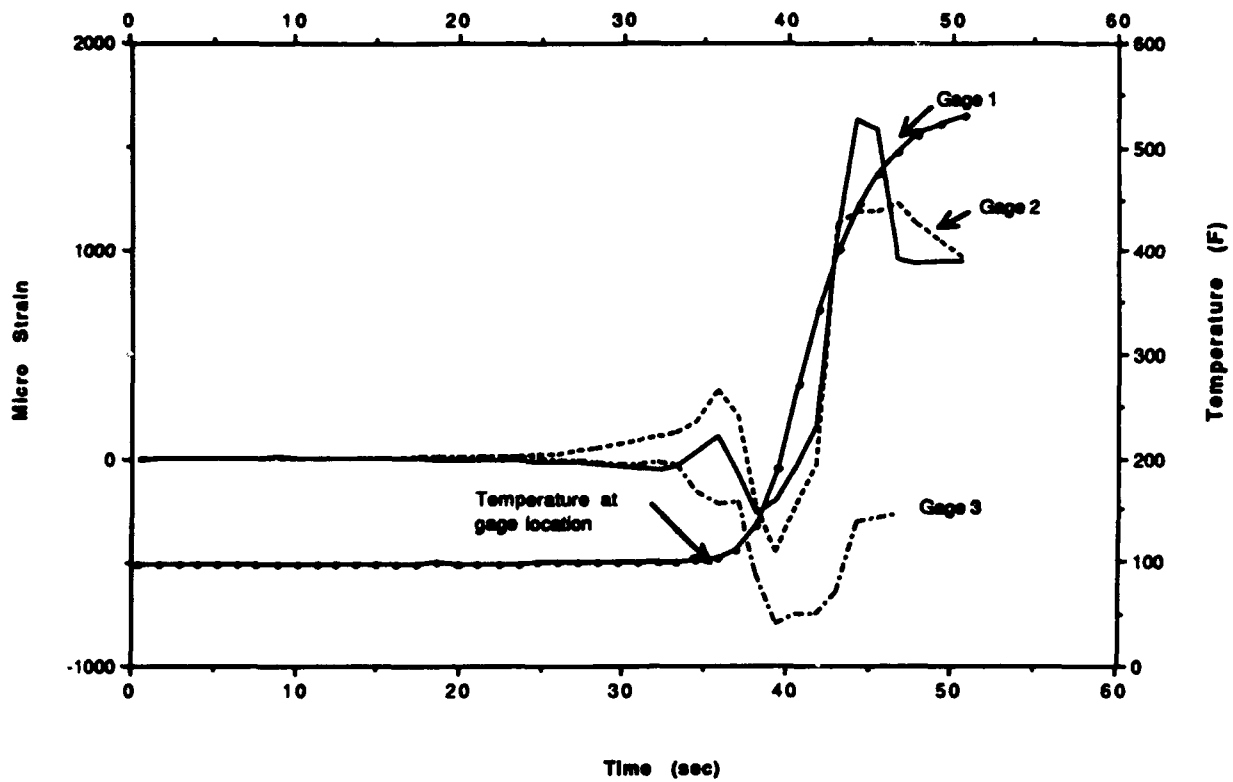Figure 36. Strain gage and thermocouple layout of Test 5

Figure 37. Thermal strain variations of Rosette 1 in Test 5, pass 1
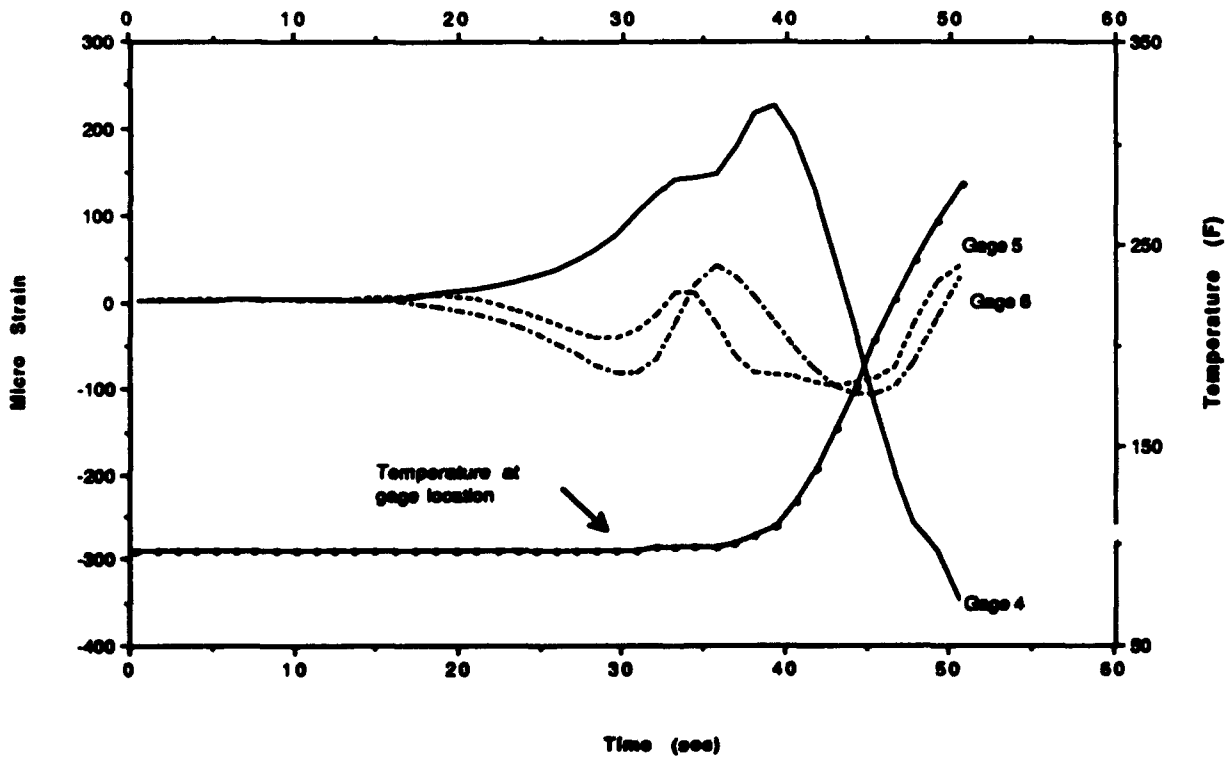

Figure 38. Thermal strain variations of Rosette 2 in Test 5, pass 1
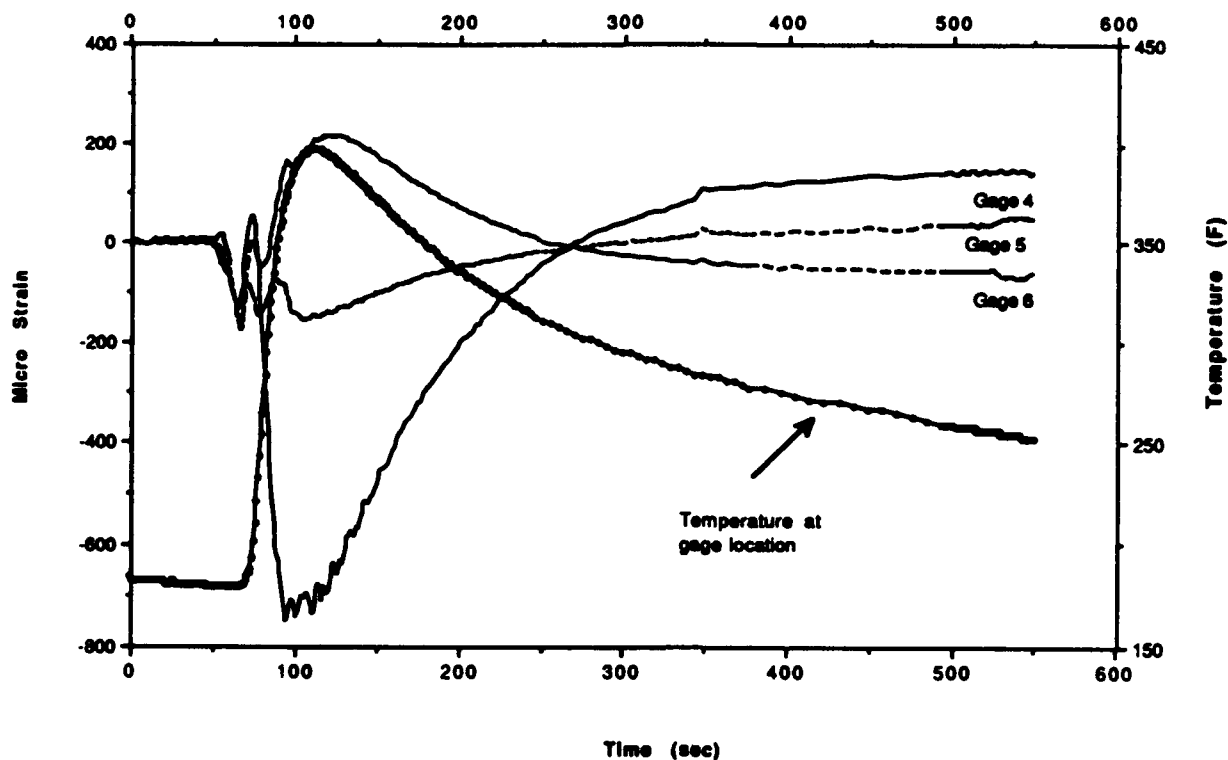
58

Figure 39.   Thermal strain variations of Rosette 2 in Test 5, pass 2

be strictly followed.   Standard data conversion coefficients A and B (equations 2, 3, and 4) were obtained from the engineering data sheet accompanied with each strain gage.   These coefficients were used throughout the tests. The strain relaxation data used to convert the strain to residual stress were those when the hole depth reached 1.2 times the hole diameter as recommended by the strain gage manufacturer (Timoshenko and Goodier 1951).

Stability of the strain gage

72.   To obtain accurate blind hole drilling results that reflect only the residual stress from welding, the drilling must be performed slowly with minimal pressure; otherwise, additional thermal and mechanical strains from drilling will be superimposed.   To achieve this goal the drilling process usually took approximately 5 min to complete.

73.   Another concern that could influence obtaining accurate results was the thermal strain created from the gage excitation voltage over the 5-min drilling duration.   To investigate the influence from the excitation voltage, a special test was performed (Test A).   This test consisted of monitoring the strain reading variance with time from an identical strain gage rosette, as those used in the actual Test 1 through Test 3, bonded to a stress-relieved

annealed ASTM A-36 plate. No hole was drilled in this special test. A gage
excitation voltage input similar to those used in Test 1 through Test 3
(approximately 5 volts) was applied to the gages and the outputs from the
gages were monitored for approximately 40 min with the data acquisition sys-
tem. If sufficient heat was generated by the applied 5 volts, then there
would be a significant variance in the strain readings with time. The results
from the Special Test A are plotted in Figure 40. It is clear that the ther-
mal strain from the excitation voltage itself, during the 5 min of hole drill-
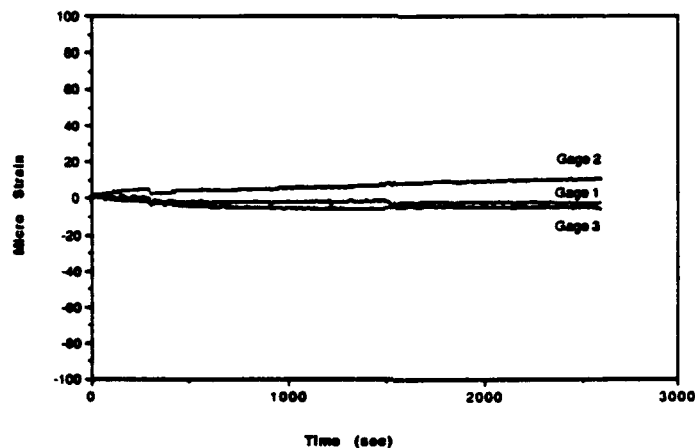ing, is negligible.

Figure 40. Thermal strain disturbance generated by
strain gage excitation voltage (Special Test A)

Machining stresses due to hole drilling

74.   Another concern for obtaining accurate blind-hole drilling data is
that the mechanical strain created from friction during drilling and the local
strain from the punching force may influence the accuracy of the measured
welding related residual strain. To determine the machining effect from hole
drilling on residual stress measurements, Test C was conducted. In the test,
strain gage output with respect to the hole depth was recorded. The test was
performed on a preannealed 1-in.-thick steel plate which was also later used
in Test 3. Figure 41 shows the strain relieved as a function of the hole
depth. The average machining stress is -5 ksi (compression). The strain
readings reached steady values when the ratio of hole depth-to-diameter equals
0.5. In the case of uniform stress along the through thickness direction, the
steady strain readings occur when the hole depth reaches the hole diameter.
Hence, the mechanical stresses from hole drilling is localized at the surface.
It should be noted that, from Figure 41, the strain gage readings are not zero
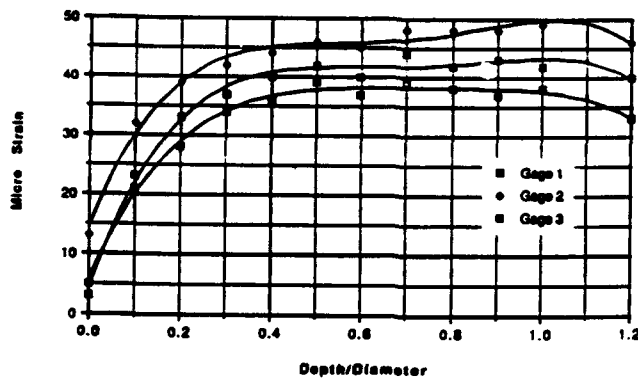
60

Figure 41. Strain relaxation versus hole depth
(Special Test C, hole drilling effect)

when the drill just contacts the surface (Depth/Diameter - 0). The primary
cause may be the compressional pressure injected on the strain gage rosette by
the air flow from the high-speed air turbine drill. Throughout this study,
the pressure used to drive the drill was kept at 40 psi, as recommended in the
operation manual. Errors caused by this effect are even smaller than those
from machining stress. No correction was therefore necessary to correct for
machining related stresses due to hole drilling.

Initial stresses prior to welding

75. To assure the blind-hole drilling method only measures welding
residual stress and is not influenced by residual stress created during mill
rolling, Test B was performed to measure the initial residual stresses in the
plate under "as received" state. The results are shown in Figure 42 and the
average initial residual stress is about -12.7 ± 0.5 ksi. Thus, to provide
accurate data for verifying the computer numerical simulation results, the
plates used in the tests had to be annealed to remove the high initial
residual stresses. This was done by slowly heating the specimens to 1,650 °F,
holding for 2 hr at this temperature, and then furnace cooling to ambient tem-
perature. After the stress-relieving heat treatment, the residual stress
prior to welding was reduced to -5 ksi (Test C).

Residual stresses in 1-in.-
thick, double V-groove plate (Test 2)

76. The testing specimen was first annealed at 1,650 °F for 2 hours to
eliminate the initial residual stress. Then the specimen was welded according
to Section 2.4, followed by residual stress measurement. Residual stress mea-
surements were obtained at three locations by using the blind-hole drilling
technique. The locations of the holes were around the middle transverse cross
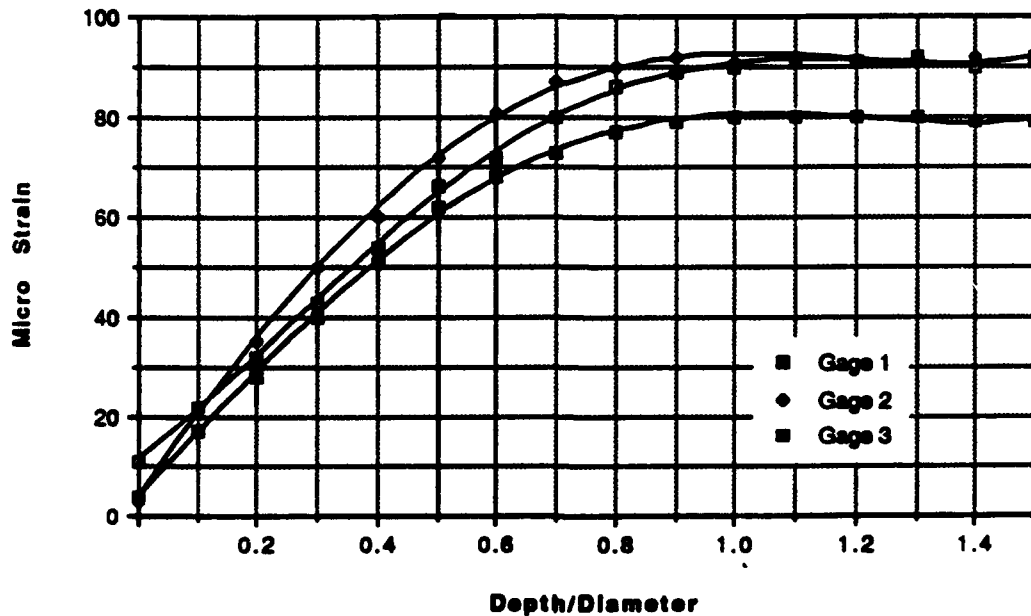
61

Figure 42. Strain relaxation versus hole depth for Special
Test B, initial residual stresses

section of the specimen. The residual stresses are represented by the maximum
principal and minimum principal stresses, and the angles (α) between the
maximum principal stress and the direction transverse to the weld bead as
shown in Figure 43. The angle α is positive when clockwise from the direction
transverse to the weld bead to the maximum principal stress. The welding
residual stress distribution as a function of the distance from the final weld
fusion line are presented in Figure 44, Figure 45, and Table 11, in terms of
the magnitudes and angles. There is high biaxial tensile stresses in the near
HAZ. The maximum principal stress drops to zero as moving away from the
fusion line; whereas the minimum principal stress becomes negative. The
maximum principal stress is more towards to the transverse direction to the
weld bead. In other words, the transverse stresses in the HAZ is higher than
the longitudinal stress. Examples of the strain relaxation curves are given
in Figure 46 and Figure 47.

62
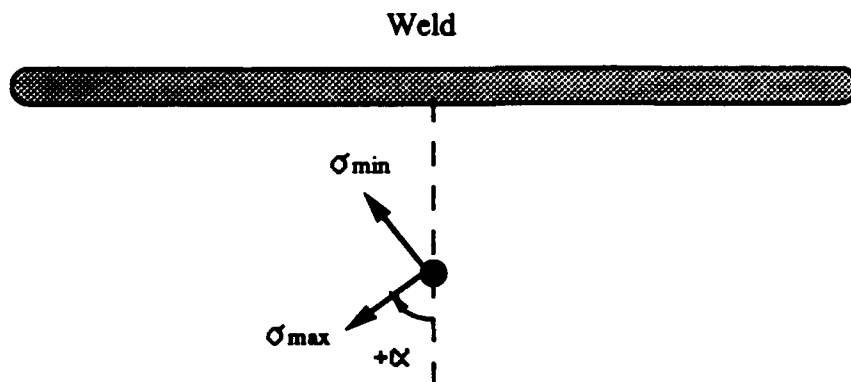
Weld

Figure 43. Maximum (σ_{max}) and minimum (σ_{min})
principal stresses and their directions
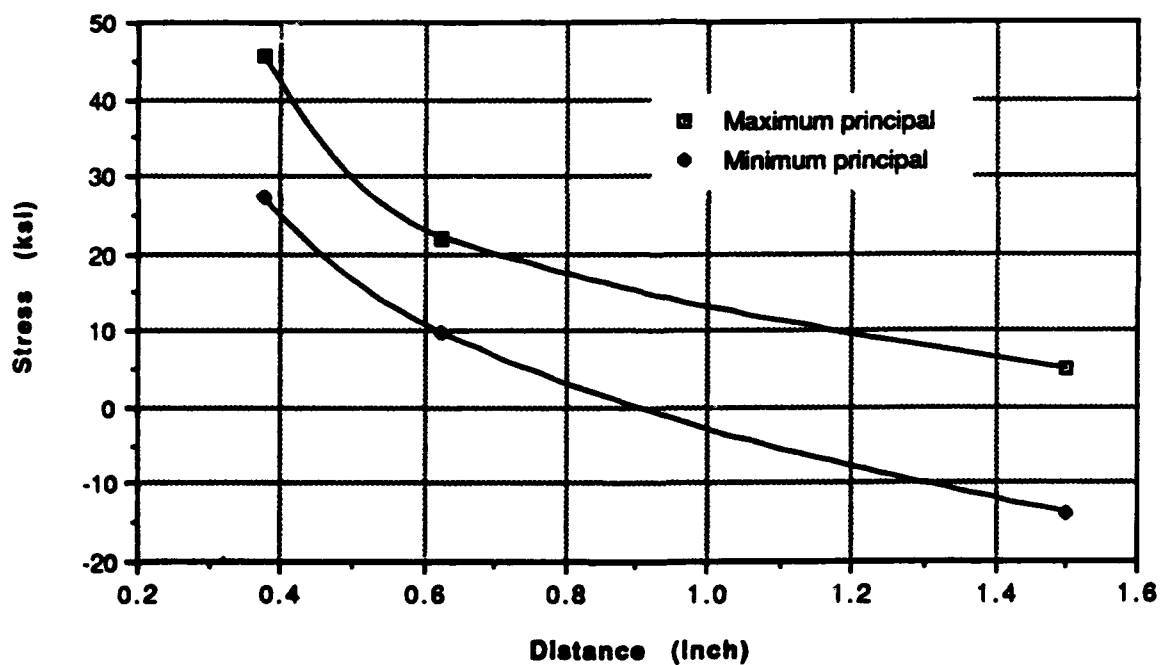
Figure 44. Residual stress distribution as a function of the
distance from the weld fusion line (Test 2, 1-in.-thick,
double V-groove)
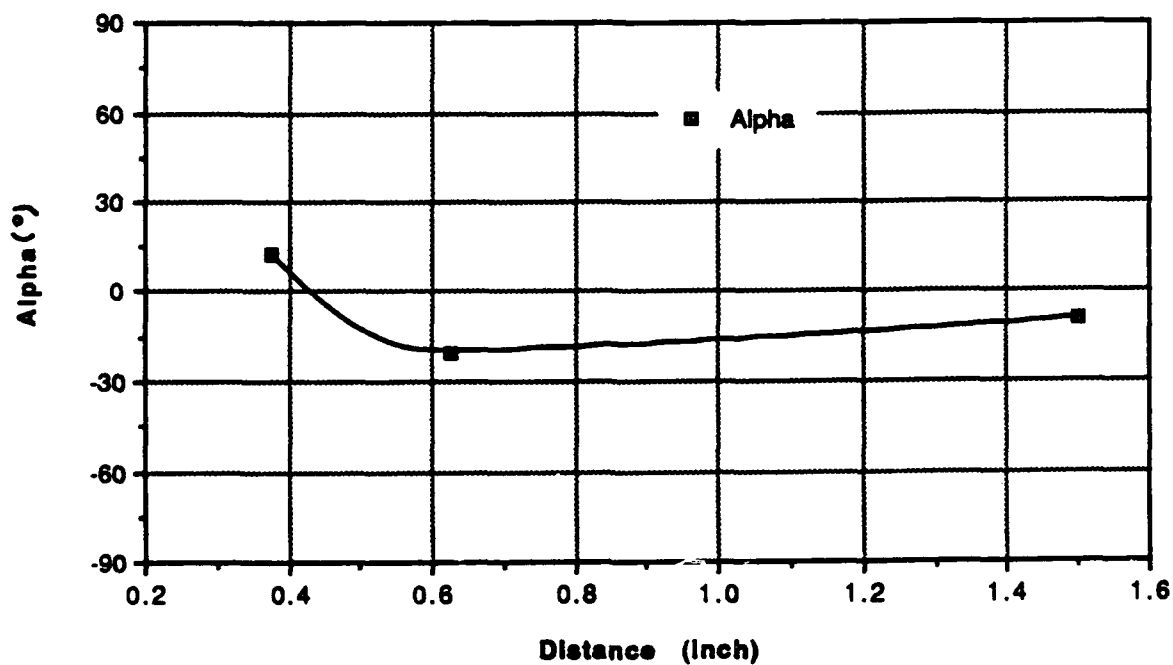
Figure 45. The angle between the maximum principal stress and the direction transverse to the weld bead. (Test 2, 1-in.-thick, double V-groove)

Table 11

Residual Stress Distribution in Test 2, 1-in. Plate, Double V-Groove

Distance in.	σ_{max} ksi	σ_{min} ksi	α deg
0.375	45.7	27.2	13
0.625	22.0	9.6	-20
1.5	5.0	-13.9	-9
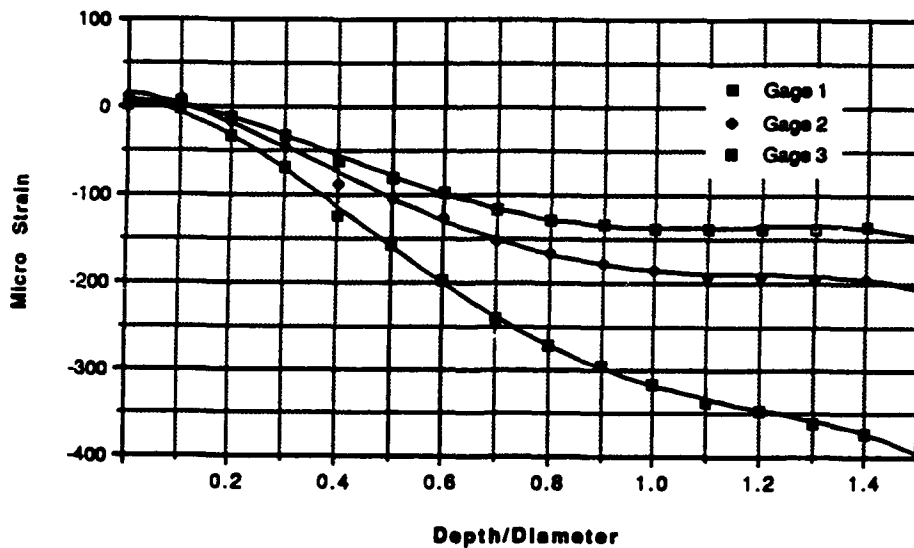
Figure 46. Strain relaxation as a function of the hole depth
(Test 2, 1-in.- thick, double V-groove, 0.375 in. from the
fusion line)

Figure 47. Strain relaxation as a function of hole depth (Test 2,
1-in.-thick, double V-groove, 1.5 in. from the fusion line)

**Residual stresses in 1-in.-
thick, single V-groove plate (Test 3)**

77. The residual stress distribution on the top surface of a 1-in.-
thick, single V-groove plate was determined (Test 3). The specimen was first
annealed at 1,650 °F for 2 hr before welding to eliminate preexisting residual
stresses. Two strain gage rosettes were located at 0.25" from the fusion
line, with four additional rosettes located at 0.5, 0.75, 1, and 2 in. from

the weld fusion line. They were located around the middle transverse cross section of the specimen. The residual stress distribution as a function of the distance from the weld fusion line at the joint face are shown in Figure 48, Figure 49, and Table 12. They are expressed in terms of the maximum principal stress, the minimum principal stress, and the angle between the maximum principal stress and the direction transverse to the weld bead as shown in Figure 43. Similar to the results of the double V-groove specimen (Test 2), high biaxial tensile stresses exist in the near HAZ. The maximum principal stress drops to zero while the minimum principal stress becomes negative (compression) at positions away from the fusion line. The transverse residual stress is higher than the longitudinal stress. By comparing Figure 44 and Figure 48, the overall trends of the stress distribution, however, is that the tensile stresses in the HAZ of the double V-groove plate is higher than these in the single V-groove plate at the same distance from the fusion line. Figures 50 through 52 show the strain relaxation curve at 0.25, 0.5, and 2 in. from the weld fusion line, respectively.

Table 12

Residual Stresses on the Top Surface of Specimen in Test 3 (1-in. Plate, Single V-groove)

Distance in.	σ_{max} ksi	σ_{min} ksi	α deg
0.25	54.7	30.7	26
0.25	22.3	13.1	-12
0.5	8.7	0	7
0.75	9.1	-7	3
1	5.5	-10.7	0.5
2	-4.5	-16.1	-5

Residual stresses in
0.5-in. thick plate (Test 1)

78. In Test 1, residual stress was measured at 0.25 in. from the fusion line. The maximum principal stress is 40 ksi in tension, whereas the minimum principal stress is 13.8 ksi in tension. These values are near the 1-in.-thick plate measurements at the same distance from the fusion line. The angle (α) shown in Figure 43 between the maximum principal stress and the direction transverse to the weld bead is 79 deg. This indicates that for this welded

66
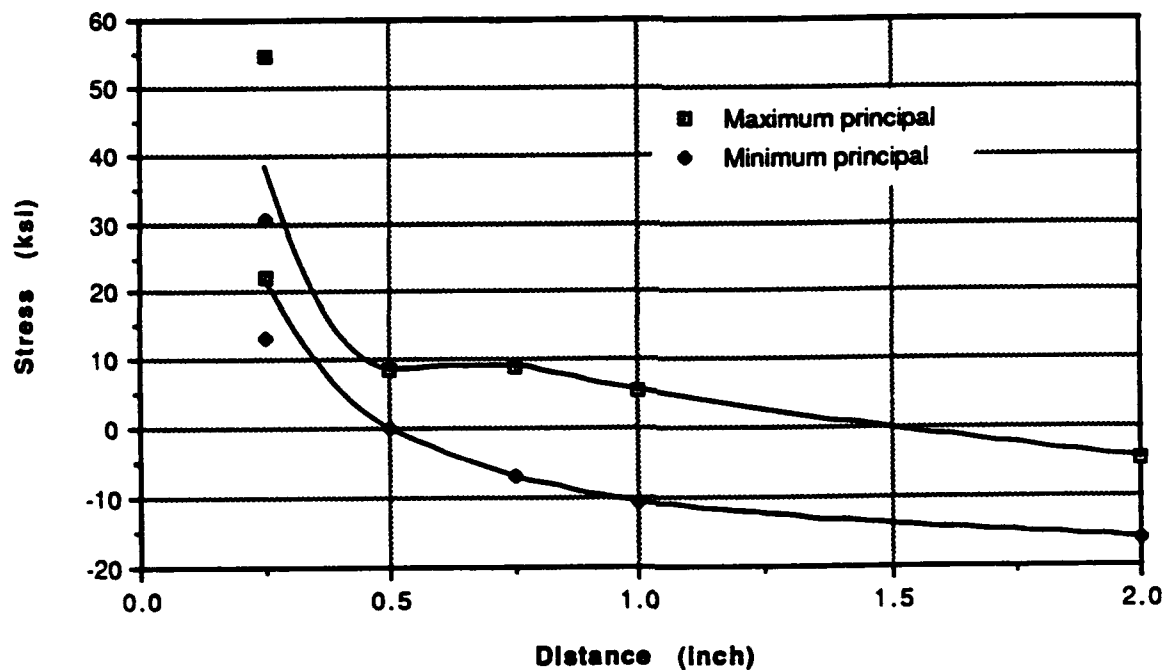
Figure 48. Residual stresses versus distance from the fusion line
in Test 3 (1-in.-thick, single V-groove, joint face)

Figure 49. The angle between the maximum principal stress and the direction
transverse to the weld bead (Test 3, 1-in.-thick, single V-groove,
joint face)

Figure 50.   Strain relaxation curve as a function of the hole depth
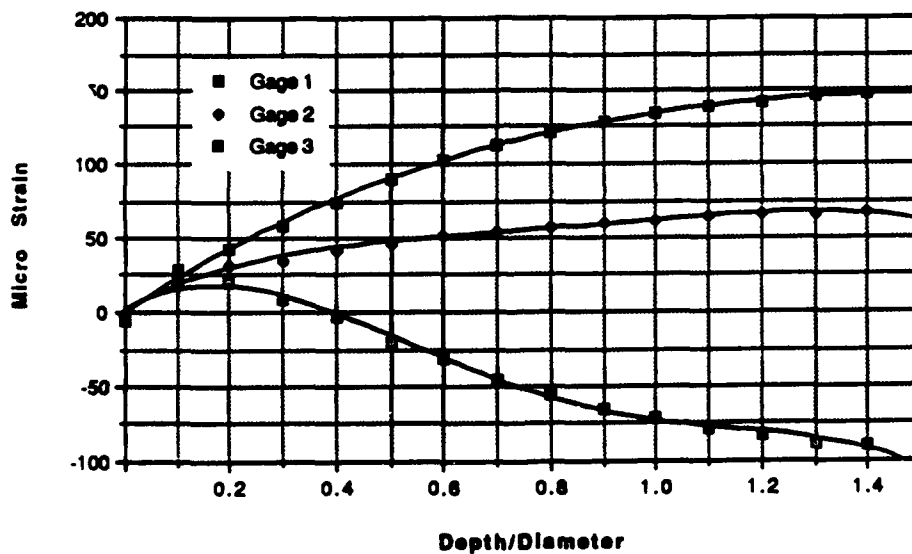(Test 3, 1-in.-thick, single V-groove, 0.25 in. from the
fusion line)

Figure 51.   Strain relaxation curve as a function of the hole depth (Test 3,
1-in.-thick, single V-groove, 0.5 in. from the fusion line)
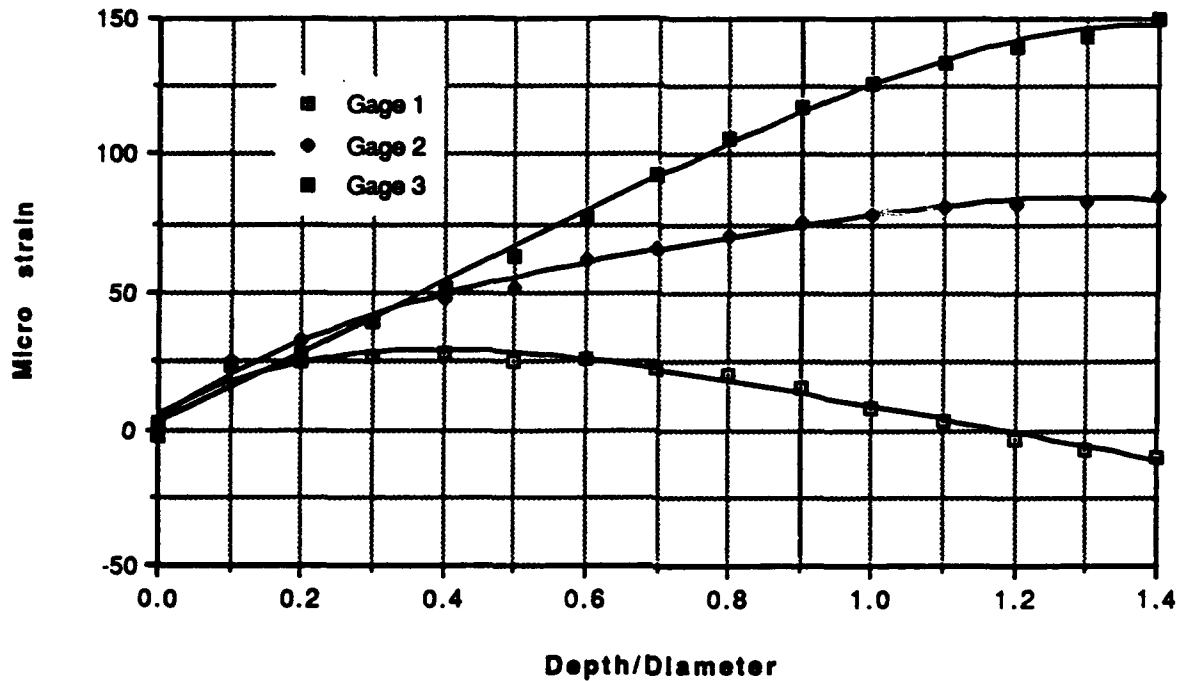
Figure 52. Strain relaxation curve as a function of the hole depth
(Test 3, 1-in.-thick, single V-groove, 2 in. from the fusion line)

0.5-in. thick plate, the longitudinal residual stress is greater than the
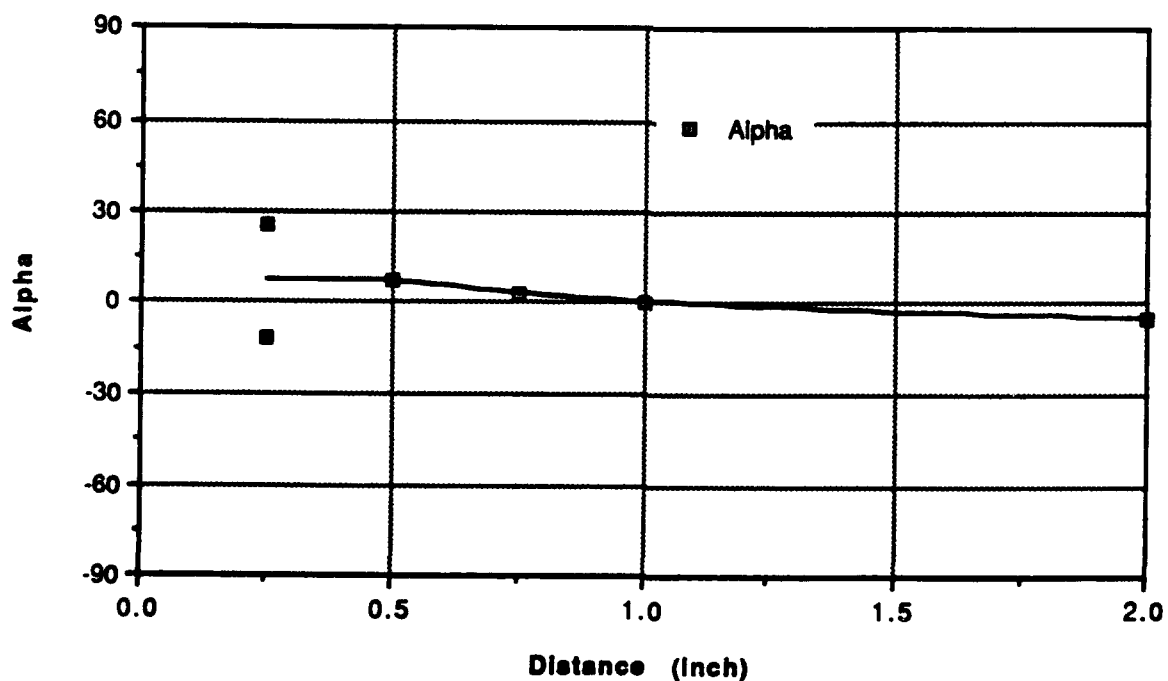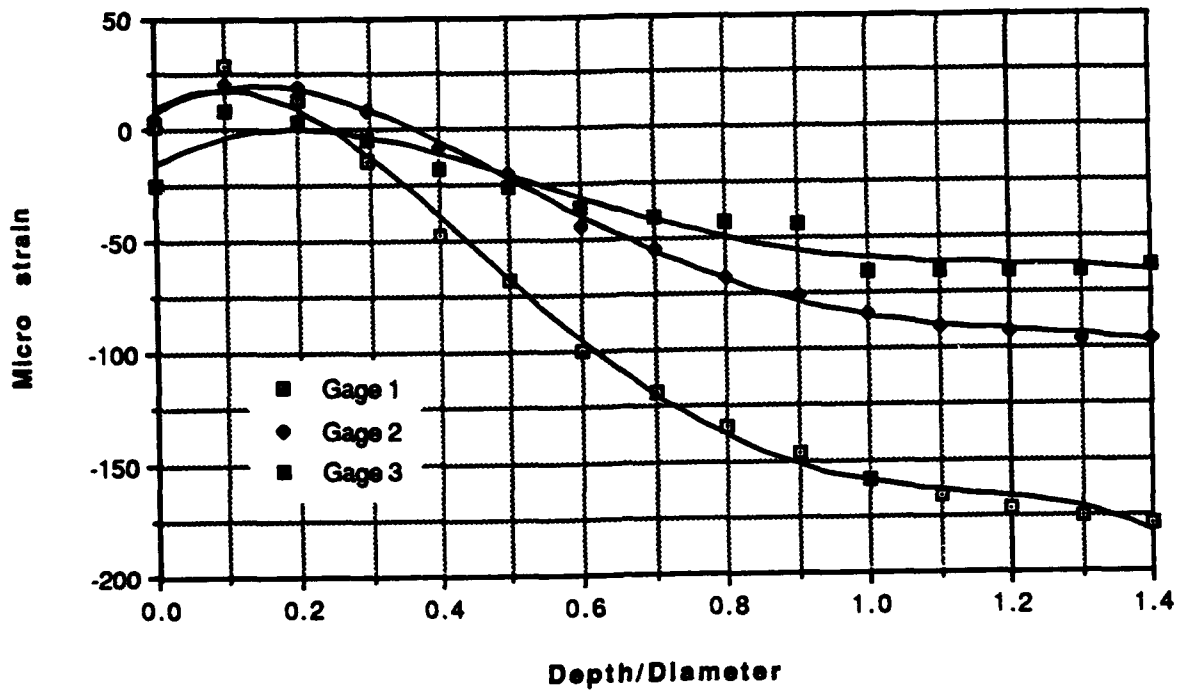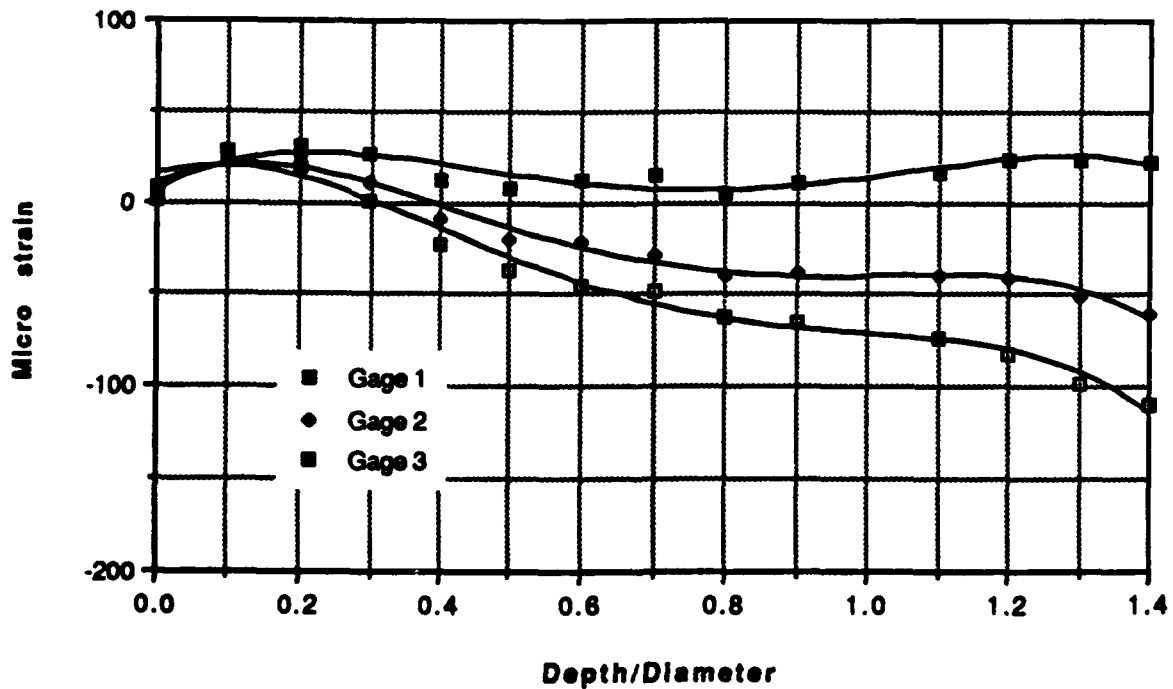transverse residual stress. This is contrary to the results obtained from 1-
in.-thick plates used in Test 2 and Test 3 which show that the longitudinal
residual stress is less than the transverse residual stress at the same dis-
tance from the fusion line.

Remarks

79. Quantitative temperature results were obtained via the thermocouple
method. The infrared technique is not capable of comparing and verifying the
finite element analysis results, due to the qualitative or semiquantitative
nature of the Inframetrics Model 525 system used in the study. The tempera-
ture measurement via thermocouple was repeatable and accurate enough when the
thermocouples were 0.5 in. or further away from the fusion line of the weld
bead which is being deposited. When the distance is shorter than 0.5 in., the
repeatability of the measurements tended to be more dependent upon the
accuracy in measuring the distance between the thermocouple and the fusion
line as well as upon the size of the thermocouple junction on the specimen

69

surface, rather than the thermocouple technique itself. Repeatability could be improved by measuring the distance after welding and make the junction size small. Nevertheless, the thermocouple measurement results obtained in this study can be used to quantitatively compare with the results from the finite element analysis which are discussed in Part III.

80. The measurement of transient thermal strain was more troublesome. The practical technique is limited to the high temperature strain gage only. The application of X-ray diffraction or magneto-elastic techniques to the real time welding thermal strain measurement is not restricted by the high temperature. Much of the technical details, however, remains unsolved for practical use. The high temperature strain gage technique gives only reliable information on transient thermal strain where the temperature is not high, that is, in those areas that are away from the fusion line. The closest distance is typically limited to 1.5 to 2 in. away from the fusion line. Nevertheless, limited results from this study indicate that the transient thermal strain variances are very complicated.

81. Quantitative surface residual stresses were obtained by using the blind-hole method. It indicates that, in 1-in.-thick plates, transverse tensile stresses in the HAZ are higher than the longitudinal stresses, whereas 0.5-in. plate shows an opposite result. In addition, double V-groove geometry in 1-in.-thick plate has higher tensile stresses in HAZ than the single V-groove geometry for both transverse and longitudinal directions. The measurement errors introduced by the blind hole drilling methods is small in comparison with the magnitudes of welding residual stresses in the HAZ.

PART III: NUMERICAL ANALYSIS BY FINITE ELEMENT METHOD

Introduction

82. Part III of this report pertains to the background, procedure, and
results obtained from existing experimental techniques available to measure
thermal history and residual stress. A limiting fact for these techniques is
that only surface measurements can be obtained. The purpose of Part III is to
explore the development of a numerical model that can be used to evaluate
temperature and thermal stress history throughout the entire weldment. This
includes an analytical method for predicting through-thickness distribution of
residual stresses in multipass welding of thick plates. The practical diffi-
culty in measuring through-thickness residual stresses is that the procedure
is destructive. The weldment must be sliced into sections while strain gages
are used to measure released strain. Therefore, numerical analysis is a very
effective method that can be used to predict residual stress distribution
through the plate thickness. The accuracy of the analysis was checked by tem-
perature measurements using thermocouples and hole drilling residual stress
measurements at the surface of the plates. The results of this comparison
will be discussed in the Part IV.

83. The finite element code ABAQUS was used for this study. The finite
element method is very useful for modeling nonlinear response. Many commer-
cial finite element packages have been successfully employed in the analysis
of welding problems (Tekriwal, Stitt, and Mazumder 1987; Free and Porter Goff
1989).

84. The thermal and stress response of weldments is a three-dimensional
problem that may require a considerable amount of computing time and be
costly. Frequently, symmetry along the cross section is assumed to reduce the
problem to a two-dimensional plane strain analysis. Adequate results with the
plane strain assumption have been reported by many investigators (Free and
Porter Goff 1989; Argyris, Szimmat, and William 1982). The generalized plane
strain theory assumes rigid body movement of the cross section along the weld-
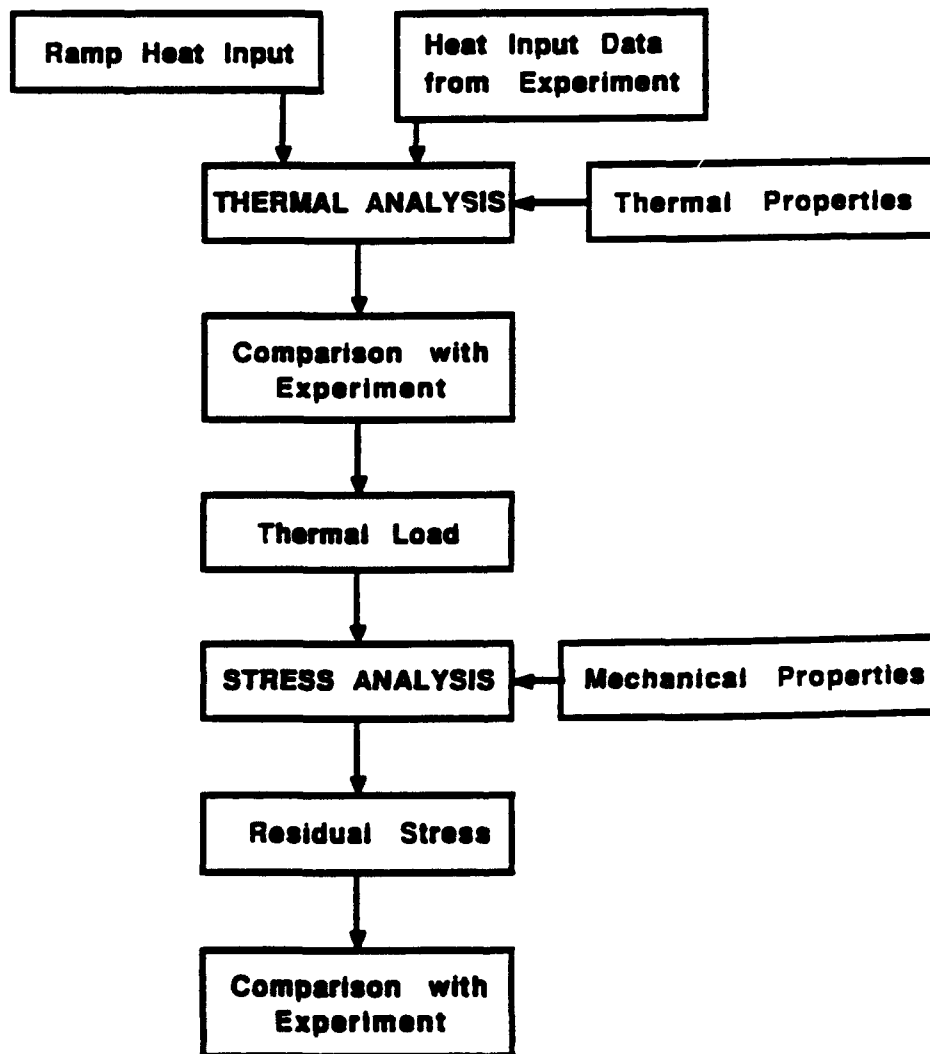ing direction.

85. Since plastic deformation has a negligible effect on the welding
temperature field, an uncoupled thermomechanical analysis was performed. This
implies that the thermal analysis is initially performed and the temperature
history from that analysis is then used as the loading input for the

71

subsequent stress analysis. The temperature data is input into the stress analysis by time steps. The finite element mesh and time steps were identical for both the heat flow analysis and the stress analysis. A general numerical analysis procedure in the flow chart form is shown in Table 13.

Table 13

General Procedure of the FEM Analysis

NUMERICAL ANALYSIS

```
┌─────────────────┐      ┌─────────────────┐
│ Ramp Heat Input │      │  Heat Input Data│
│                 │      │  from Experiment│
└────────┬────────┘      └────────┬────────┘
         │                        │
         └───────────┬────────────┘
                     ▼
          ┌─────────────────┐      ┌─────────────────────┐
          │ THERMAL ANALYSIS│◄─────│  Thermal Properties │
          └────────┬────────┘      └─────────────────────┘
                   ▼
          ┌─────────────────┐
          │ Comparison with │
          │   Experiment    │
          └────────┬────────┘
                   ▼
          ┌─────────────────┐
          │  Thermal Load   │
          └────────┬────────┘
                   ▼
          ┌─────────────────┐      ┌─────────────────────┐
          │ STRESS ANALYSIS │◄─────│ Mechanical Properties│
          └────────┬────────┘      └─────────────────────┘
                   ▼
          ┌─────────────────┐
          │ Residual Stress │
          └────────┬────────┘
                   ▼
          ┌─────────────────┐
          │ Comparison with │
          │   Experiment    │
          └─────────────────┘
```

Finite Element Model

86. Since a butt welded plate is symmetric about the weld line, only one-half of the plate must to be modeled. The size of the mesh has an effect on the accuracy of the results. As mesh refinement increases ,convergence is promoted and the precision of the results increases, however the computing time and computational cost also increases. The trade-off between mesh geometry and computational costs must be considered. The size of the model in the fusion zone and heat affected zone should be small enough to capture the high temperature gradient in that area. The mesh size increases away from the weld area where the temperature field tends to decrease linearly. From previous experience (Boyles, Lee, and Kim 1987), the element size at the weld area should be smaller than or equal to the depth of the weld bead.

87. A two-dimensional model was used for both the heat transfer and stress analysis as shown in Figure 53. ABAQUS eight-node rectangular elements (list from element library) were used. The thermal analysis must model the heat input from the moving electrode in the two-dimensional model. The fusion zone mesh is stair-stepped to numerically represent the individual weld beads. Elements in the fusion zone were activated to simulate the deposition of the weld beads. A heat flux was applied to these newly activated elements to generate the heat input. Each pass was divided into about 50 to 100 time increments. The specific number of time increments used was dependent on the heat flux and interpass temperature. The size of the time increments used was dependent on the magnitude of the temperature gradients. The maximum allowable temperature change between time increments was 200 °F. The time increment temperature data at each node were saved as input to the stress analysis.

88. Once the thermal analysis was completed, the temperature history was used as input to the stress analysis. For each time increment, strains and stresses were calculated using the temperature data at each node. After calculation of strains and stresses for each pass, additional elements for the next bead were added to the current mesh. Strains and stresses for the next pass were then calculated with a new set of stored temperature data. This procedure was repeated for each pass until the final pass was computed.
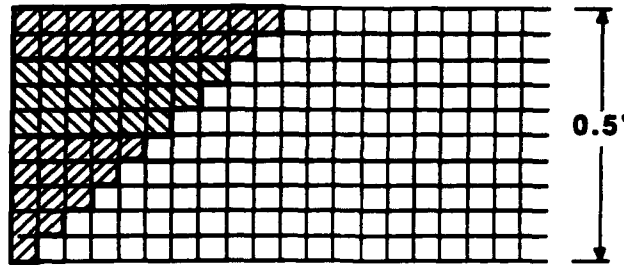
Material Properties

89. The material properties used in this research were for ASTM A36 mild steel. The thermal and stress analysis requires material properties such as conductivity, specific heat, density, latent heat, Young's modulus, yield

WELD PASSES

a) 1/2-in. plate

WELD PASSES

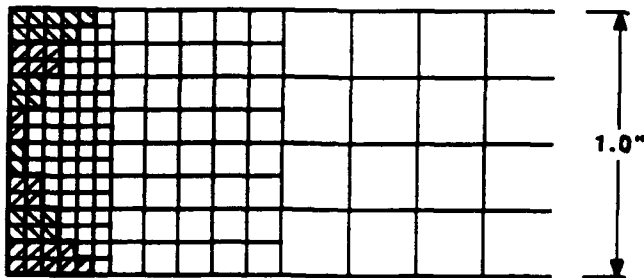b) 1-in. plate (double V-groove)

WELD PASSES
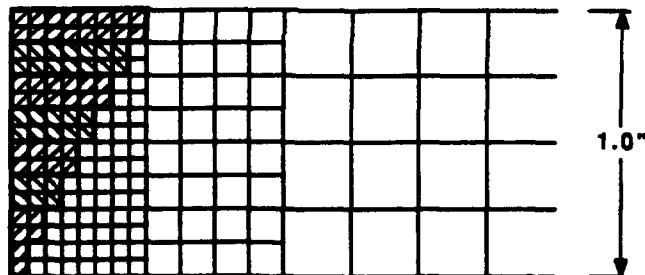
c) 1-in. plate (single V-groove)

WELD PASSES
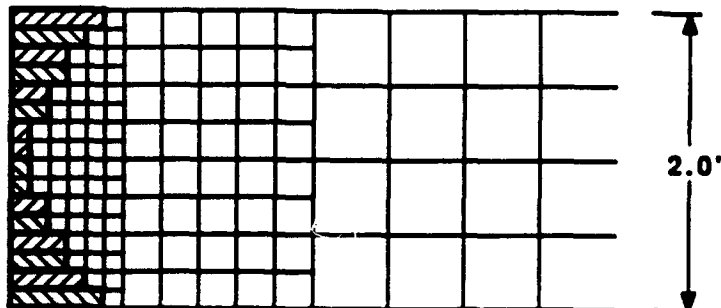

d) 2-in. plate

Figure 53. Finite element mesh

stress, thermal expansion coefficient, and strain hardening of the material. These temperature dependent thermal and mechanical properties are shown in the following tabulations and Figures 54 and 55 (American Society for Metals 1948; Ueda and Yamakawa 1973). Latent heat caused by phase transformation from solid to liquid or from liquid to solid was considered as heat sink or heat source.

- Density : 0.283 (lb/in^3)
- Thermal Conductivity:

Temperature °F	Conductivity BTU/in °F sec
70	6.93 E-4
200	6.84 E-4
400	6.50 E-4
600	6.07 E-4
800	5.60 E-4
1,000	5.05 E-4
1,200	4.50 E-4
1,400	3.70 E-4
1,600	3.40 E-4
1,800	3.60 E-4
2,000	3.80 E-4
2,200	4.00 E-4
2,400	4.20 E-4
2,600	4.40 E-4
2,800	4.60 E-4

- Specific Heat:

Temperature °F	Specific Heat BTU/lb °F
70	0.112
200	0.117
400	0.125
600	0.135
800	0.150
1,000	0.170
1,200	0.196
1,400	0.222
1,600	0.250
1,800	0.278
2,000	0.306
2,200	0.334
2,400	0.362
2,600	0.390
2,800	0.418

- Latent Heat : 117 BTU/lb
- Liquidus   : 2,770 °F
- Solidus   : 2,700 °F
- Thermal Expansion:

Temperature °F	Thermal Expansion °F^{-1}
70	6.1 E-6
200	6.4 E-6
400	6.8 E-6
600	7.2 E-6
800	7.5 E-6
1,000	7.8 E-6
1,200	8.1 E-6

- Young's Modulus:

Temperature °F	Young's Modulus psi
70	30.0 E6
200	28.5 E6
400	28.5 E6
600	27.0 E6
800	24.5 E6
1,000	17.0 E6
1,200	8.0 E6
1,400	1.0 E6

- Yield Stress:

Temperature °F	Yield Stress psi
70	36.0 E3
200	34.5 E3
400	32.5 E3
600	29.0 E3
800	25.0 E3
1,000	21.0 E3
1,200	11.0 E3
1,400	2.0 E3

- Strain Hardening: Strain hardening was assumed as shown in Figure 54.
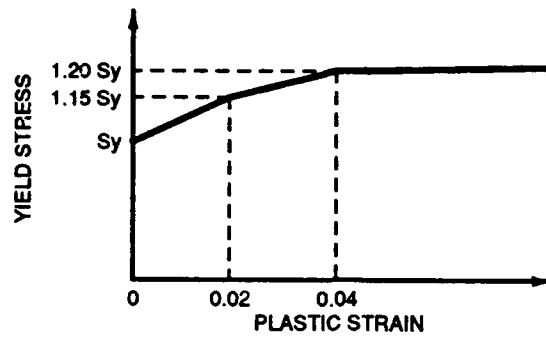
Figure 54.   Strain hardening
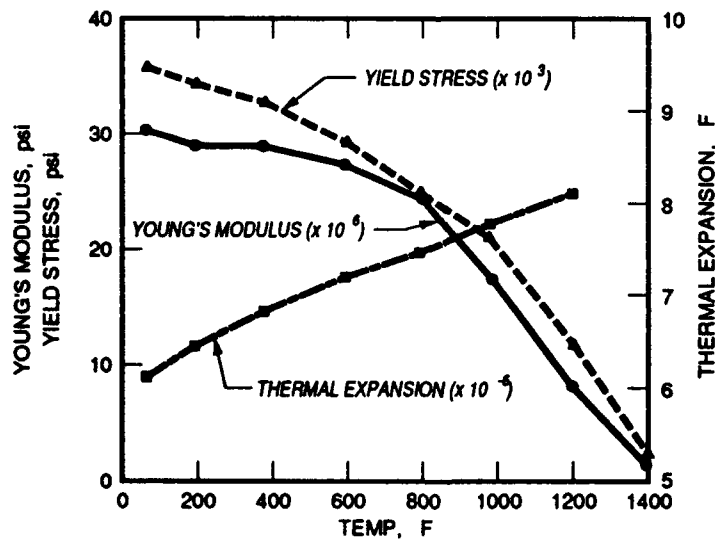
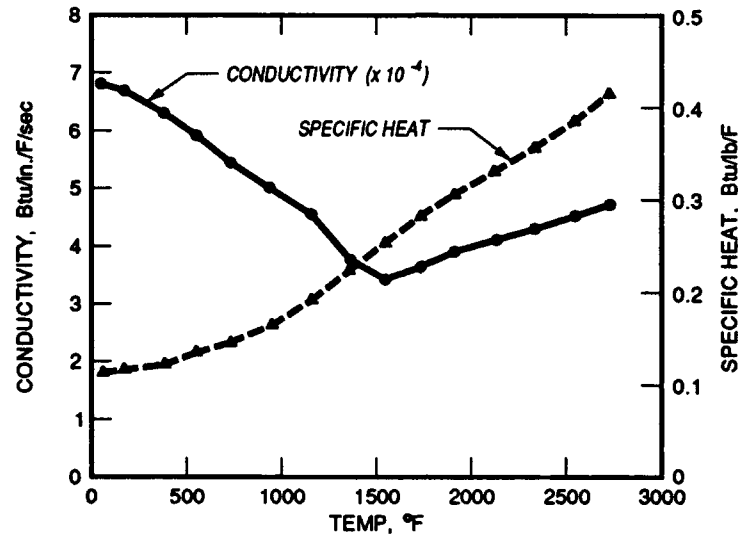Figure 55.   Temperature dependent material
properties used in the FEM analysis

77

PART IV: COMPARISON AND DISCUSSION

Thermal Analysis

Thermal model

90. A three-dimensional problem was reduced to a two-dimensional analysis by assuming heat flow in the welding direction was negligible. Computer costs were efficiently minimized by assuming symmetry about the center of the weld joint. The heat flux (q) was applied to the model gradually by using a ramp heat input model that was developed to allow variable ramp times as shown schematically in Figure 56. The ramp times for each pass and the maximum heat flux values (q_{max}) are presented in Table 14. The ramp heat input model was developed to avoid numerical convergence problems in finite element calculation due to an instantaneous increase in temperature near the fusion zone and provide for modeling the moving arc in the two-dimensional plane. The actual welding time for the arc to travel across the unit thickness of the finite element model is t1 + t2. Numerical analysis shows that as t1 increases, peak temperature decreases, and the required time to reach the peak temperature increases. Experimental results were considered in determining what the distribution of the heat flux should be with time. It was determined that for a general modeling rule of thumb, approximately 20 percent of the total model welding time (t1 + t2) should be used to input the heat flux magnitude from zero to q_{max} and decay the flux from q_{max}. Elapsed time between weld passes were assumed as 600 sec.

91. An arc efficiency of 85 percent was used for net heat input to the plate. This is a reasonable value for the GMAW process. Heat input to the plate was calculated by the following equation:
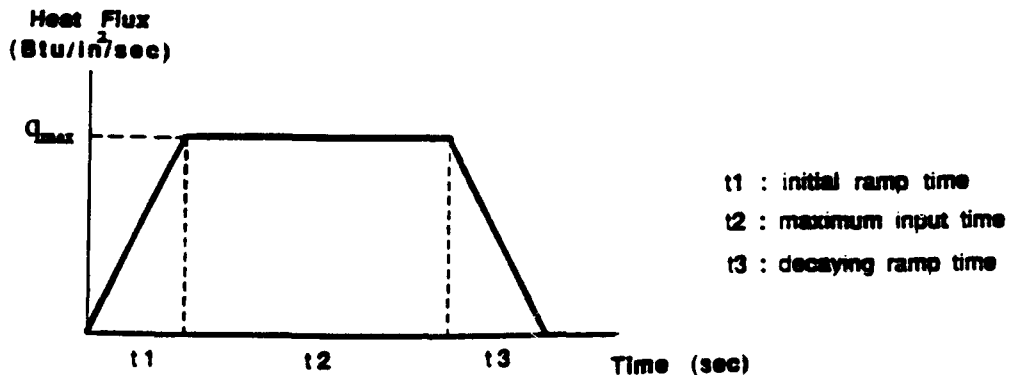

t1 : initial ramp time

t2 : maximum input time

t3 : decaying ramp time

Figure 56. Numerical model of heat flux input

Table 14

Ramp Time for Each Analysis Case

Pass	t1, sec	t2, sec	t3, sec	b*, in.	q_{max} Btu/in.^{2}/sec
A) 1/2-in. plate (Test 1)					
1	0.8	3.4	0.8	0.25	8.31
2	0.8	3.4	0.8	0.4	5.16
3	0.8	3.4	0.8	0.4	5.63
4-5	0.8	3.4	0.8	0.5	4.06
B) 1-in. plate with double V-groove (Test 4)					
1	1.5	6.1	1.5	0.125	15.31
2-3	1.1	4.3	1.1	0.1875	12.01
4-5	1.1	4.3	1.1	0.3125	7.21
6	1.5	6.1	1.5	0.125	15.31
7-8	1.1	4.3	1.1	0.1875	12.29
9	1.1	4.3	1.1	0.3125	7.37
10-11	1.1	4.3	1.1	0.3125	8.70
C) 1-in. plate with single V-groove (Test 3)					
1	1.8	7.3	1.8	0.125	15.40
2	1.8	7.3	1.8	0.1875	10.26
3-4	1.5	6.1	1.5	0.25	7.90
5-6	1.5	6.1	1.5	0.3125	6.32
7	1.5	6.1	1.5	0.3125	6.00
8-10	1.5	6.1	1.5	0.375	5.00
11-12	1.5	6.1	1.5	0.4375	4.29
13	1.5	6.1	1.5	0.4375	4.40
14-17	1.8	7.3	1.8	0.5	3.80
D) 2-in. plate with double V-groove					
1	1.8	7.3	1.8	0.125	15.4
2	1.8	7.3	1.8	0.25	7.7
3-4	1.5	6.1	1.5	0.25	7.9
5-9	1.5	6.1	1.5	0.375	5.3
10-12	1.5	6.1	1.5	0.5	4.0
13-16	1.5	6.1	1.5	0.625	3.2
17	1.8	7.3	1.8	0.125	15.4
18	1.8	7.3	1.8	0.25	7.7
19-20	1.5	6.1	1.5	0.25	7.9
21-25	1.5	6.1	1.5	0.375	5.3
26-28	1.5	6.1	1.5	0.5	4.0
29-32	1.5	6.1	1.5	0.625	3.2

* b: Width of weld bead used for heat input (equation 12)

79

$$Q = \frac{60 \, nEI}{1,055 \, Vb} \qquad (12)$$

where

Q — heat input, BTU/in^2

n — arc efficiency

E — arc voltage, volts

I — arc current, amps

V — welding speed, inches/min

60 — conversion factor, minutes to second

b — width of finite element modeling bead being deposited, in.

1,055 — conversion factor, Joule to BTU

E, I, and V are measured values from experiments.

92. Sample calculation for the first pass of the Test 1 is shown as an example.

Suppose

$n = 0.85$, $E = 24 \, V$, $I = 215A$, $V = 14.4$ inch/min

then

$$Q = \frac{60 \, nEI}{1,055 \, Vb} = \frac{60 \times 0.85 \times 215 \times 24}{1,055 \times 14.4 \times 0.25}$$

$$= 69.3 \text{ BTU/inch}^2$$

Heat Flux to the half of the plate:

$$q_{max} = \frac{nEI}{1,055 \, b} \times \frac{1}{2} = \frac{0.85 \times 215 \times 24}{1,055 \times 0.25 \times 2}$$

$$= 8.31 \text{ BTU/inch}^2/\text{sec}$$

Heat input time $(t_1 + t_2) = \frac{60}{V} = \frac{60}{14.4} = 4.17$ sec

$(Q = 2 \times q_{max} \times \text{Heat input time})$

93. Heat losses or gains from phase transformation were neglected. Free convection boundary condition were assumed for both top and bottom surfaces of the plate as opposed to forced convection where air would be passing over the surfaces. The heat convection coefficient of 1.0 E-5 BTU/in^2 F was assumed for all surfaces.

Ramp heat input

94. The ramp heat input model was used in the thermal analysis to
apply a heat flux gradually to the top surface of the elements in the fusion
zone. The general amplitude-time curve showing the variation of heat flux
with time for the ramp heat input model is shown in Figure 56. The thickness
of the two-dimensional plane strain model along the welding direction was 1-
in. One-half of the calculated heat input by Equation 12 was uniformly dis-
tributed over the 1-in. unit width during heat input time. This is the time
required for the electrode to travel across the 1-in. unit width. The heat
input time in Table 14 was determined from the welding speed in experiments.

95. Ramp times (t1 and t3) were considered from 10 to 100 percent of
the total actual heat input time (t1 + t2). The total area under these
various ramp heat input curves was kept constant to ensure that the same total
heat input to the model was maintained. The thermal analysis temperature his-
tory results for the 1/2-in.-thick plate were compared with the experimental
data (Test 1, first pass) to achieve the best ramp heat input model. Fig-
ure 57 shows the temperature profiles at 1/4 in. from the joint edge prepara-
tion for the first pass of the 1/2-in. plate (Test 1, first pass, T1) for the
various ramp heat input models. The general trend is for larger ramp times to
decrease peak temperatures and cooling rates. The temperature profiles for
large ramp times were shifted to the right indicating more time is required to
reach peak temperature. The maximum temperature difference during the heating
cycle was about 180 °F. The temperature difference during the cooling cycle
was very small compared with the heating cycle. Numerical temperature pro-
files were also compared with experimental data (T2, T4) at 1/2 in. from the
edge preparation at the top and 1.0 in. from the edge preparation at the bot-
tom of the plate as shown in Figure 58 and 59. General trends were the same
as the temperature profiles at 1/4 in. from the edge, but the effect of ramp
time was less dominating as the distance from the edge increased. Generally a
ramp time of 20 percent of the total weld time (t1 + t2) gave the best corre-
lation with the experimental data. Consequently, this value was selected to
model the heat input.

Results of the thermal analysis

96. Figure 60 and Figure 61 show the numerically calculated tempera-
ture versus time plots for the first pass at thermocouple locations T1 and T2
on the top surface of the 1/2-in.-thick plate (Test 5). Experimental results
from the thermocouples are also plotted for comparison. The temperature
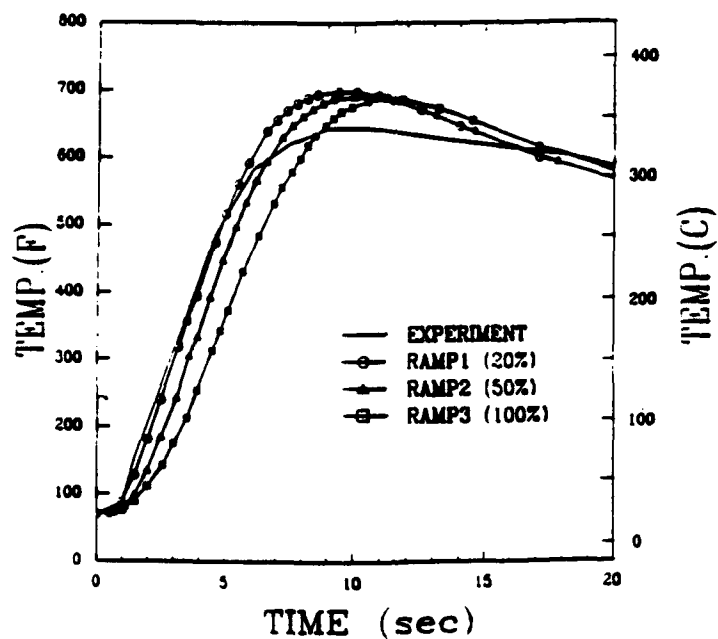
81

Figure 57.   Temperature profiles for the first pass of
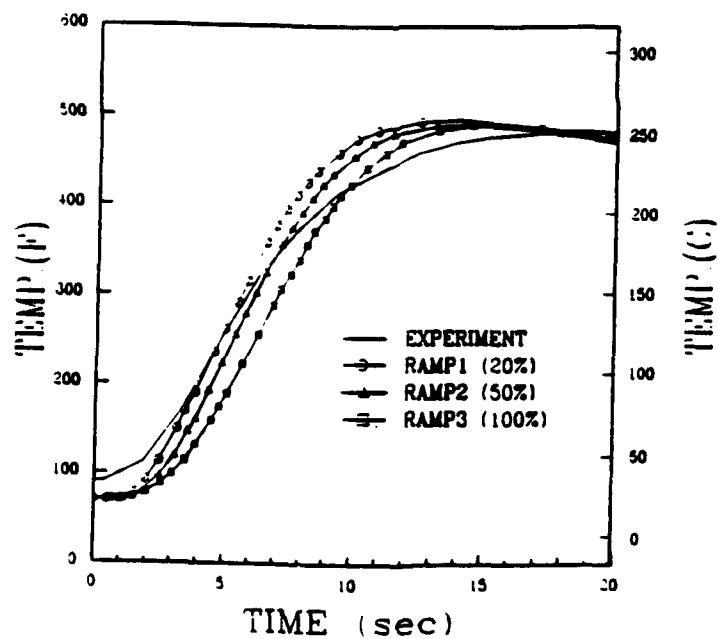1/2-in. plate (1/4 in. from the edge preparation at
the top, T1)

Figure 58.   Temperature profiles for the first pass
of 1/2-in. plate (1/2-in. from the edge preparation
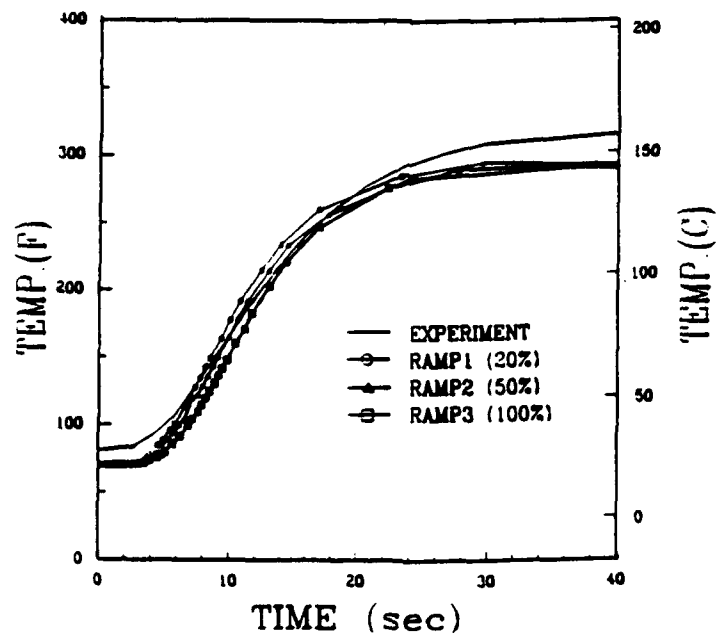at the top, T2)

82

Figure 59. Temperature profile for the first pass of
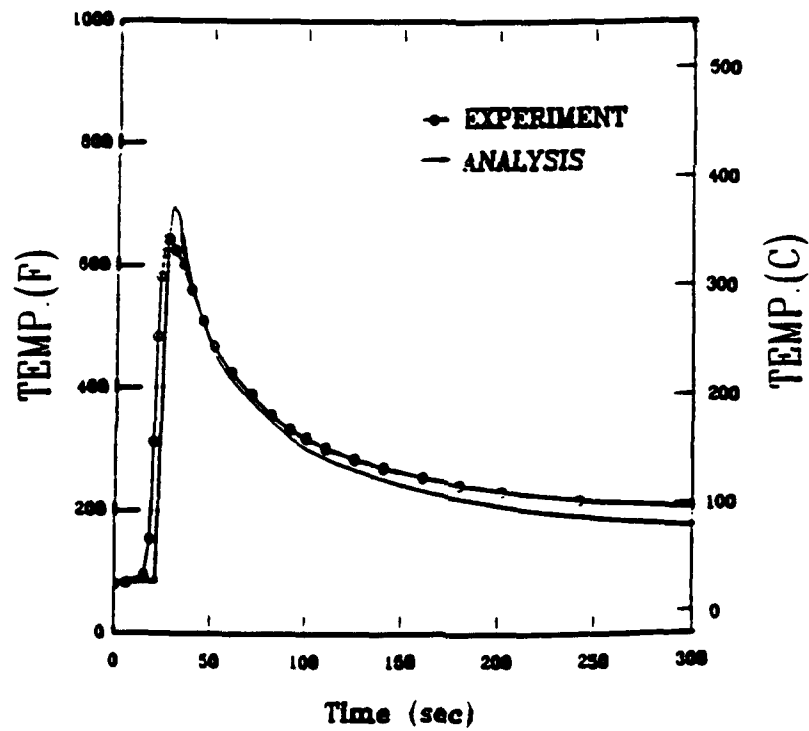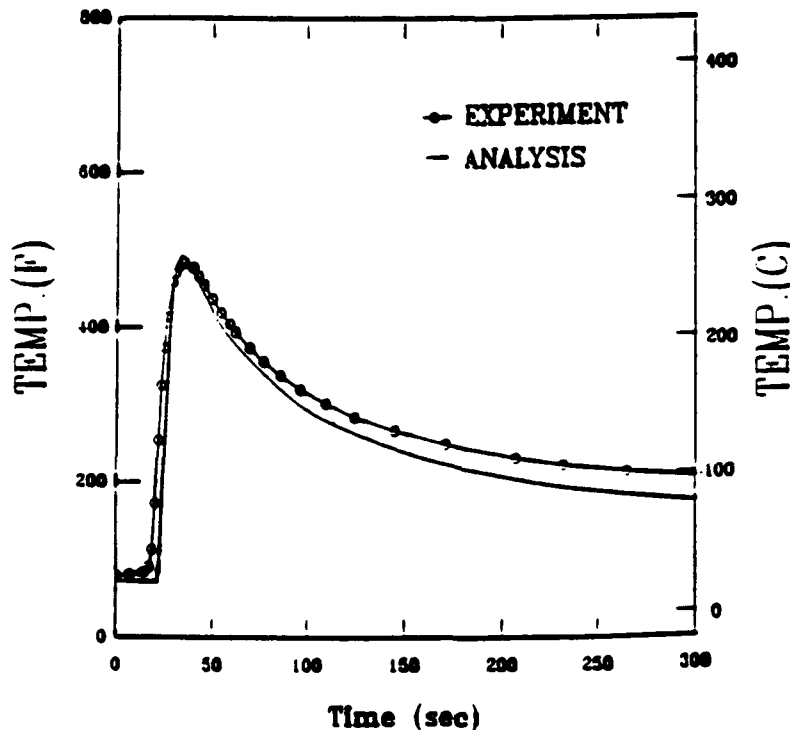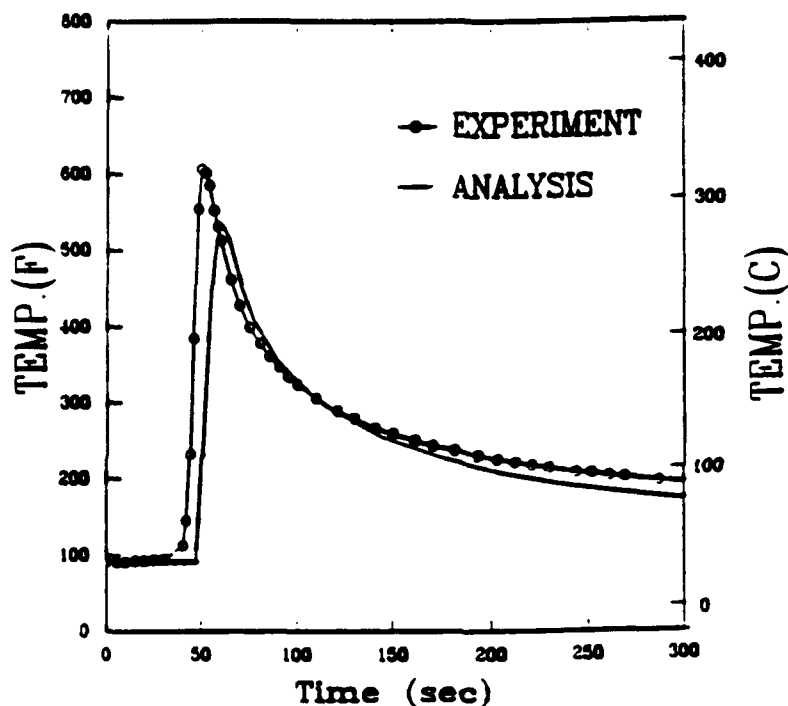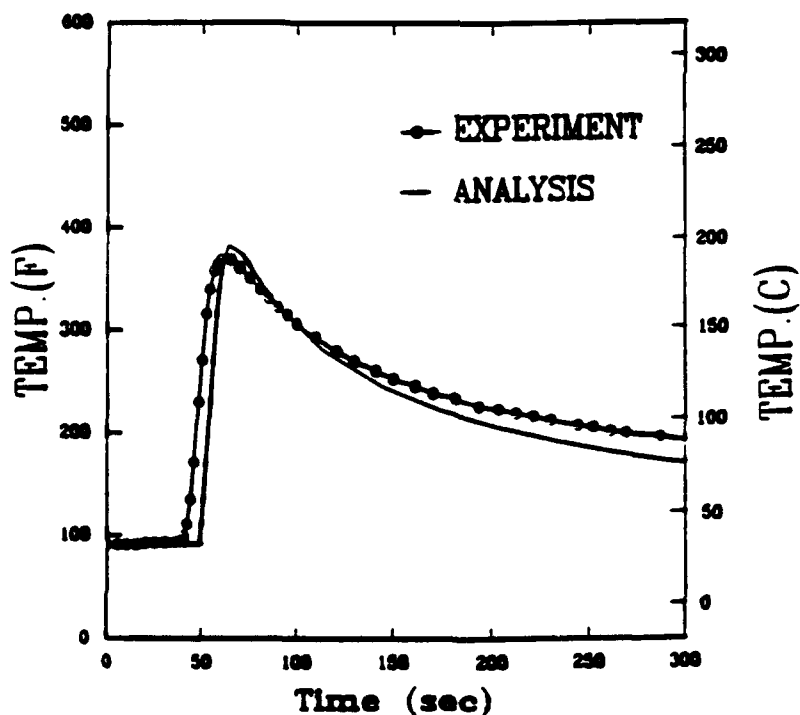1/2-in. plate (1 in. from the edge preparation at the
bottom, T4)

Figure 60. Temperature profile for the first pass
of 1/2-in. plate (1/4 in. from the edge preparation
at the top, T1)

Figure 61. Temperature profile for the first
pass of 1/2-in. plate (1/2 in. from the edge
preparation at the top, T2)

profiles from the analysis show good correlation with the experimental data
near the weld. This is important since high temperature in this area usually
results in large plastic strains and thermal stresses. Generally, the
difference between the peak temperatures calculated by the thermal analysis
and the experimental results were within ± 10 percent.

97. Several ramp times were investigated for the 1/2-in.-thick plate
(Test 1) to develop an appropriate amount of ramp time to model the heat
input. Larger ramp times tend to lower peak temperature and decrease cooling
rates. A ramp time consisting of 20 percent of the total heat input time gave
the best correlation between calculated temperatures and experiments. Fig-
ure 62 and Figure 63 also show the temperature profiles for a 1-in.-thick
plate (Test 4). The same general trends as the 1/2-in.-thick plate also
exists.

98. Each pass modeled in the thermal analysis was divided into small
time increments, such that the maximum temperature change between any two time
increments was less than 200 °F. The temperature data for each increment were
saved and used as input to the stress analysis.

Figure 62. Temperature profile for the first pass of
1-in. plate (1/4 in. from the edge preparation at
the top, T2)

Figure 63. Temperature profile for the first pass
of 1-in. plate (1/2 in. from the edge preparation
at the top, T3)

Stress Analysis

Structural model

99. Generalized plane strain theory was used for the stress analysis to consider the strain of the cross section in the direction of welding. Generalized plane strain theory assumes that the model lies between two initially parallel planes perpendicular to the welding direction. These planes may move as rigid bodies with respect to each other, so strain varies linearly throughout the cross section. The same finite element mesh and time increments were used for both the thermal and structural analysis.

100. The fusion zone elements are incrementally activated to model the weld passes as they are deposited. The temperature history obtained from the thermal analysis is input as a thermal loading into the structural model to calculate thermal strains and stresses for each time increment. These thermal strains and stresses are accumulated to produce the final state of residual stresses.

101. Two models were used for stress analysis of 1-in. and 2-in.-thick plate. The first model (not lumped model) analyzed the heat flux of each individual pass and distributed it over the top surface of weld bead. The result of temperature analysis for each pass was used as thermal loading in the stress analysis. This procedure was repeated for each pass to complete the weldment. The second model (lumped model) used lumped passes. Each layer of weld bead was considered as one lumped pass in this model. Heat fluxes for each pass in that layer was added and distributed over the top surface of the layer.

102. Temperature dependent material properties and the von Mises yield criterion were used as shown in paragraph 90. The von Mises yield criterion assumes that yielding begins when the distortion energy equals the distortion energy at yield in simple tension. The von Mises yield criterion usually fits the experimental data better than the other theories, and it is easier to apply. Free boundary conditions were modeled for the free surfaces except at the center line of the cross section, where symmetry conditions exist. Volume changes due to phase transformations were neglected. Initial stresses and strains were zero, since the test specimens were stress relieved before welding. The mass of the plate was not included in the analysis.

Results of the stress analysis

103. Figure 64 shows the transverse (perpendicular to the welding direction) stress at the top surface of the 1-in.-thick butt welded plate with a double V-groove (Test 2). Tensile stress is positive in the plots. Both the stresses calculated by finite element analysis and the results of the blind-hole drilling method were plotted for comparison. The distribution of the stress is in relatively good agreement. As shown in Figure 64, the transverse residual stress exceeds yield strength near the fusion line and decreases rapidly away from the weld. This stress pattern results from the high temperature gradients and nonlinear thermal cycles that occur at the fusion zone during welding. The transverse stress for a single V-groove butt joint (Test 3) also shows a tensile zone near the center of the weld and zero stress away from the fusion line as shown in Figure 65; however, the stress magnitude near the center line is much less than that of the double V-groove. The finite element predicted and experimentally measured longitudinal (welding direction) stress distribution for the 1-in.-thick butt welded plates (Test 2 and Test 3) are shown in Figure 66 and Figure 67. Both figures show a similar distribution of tensile and compressive stresses, indicating that the joint geometry on a single flat plate is not a major factor that influences the longitudinal stress distribution on the surface. The agreement between theoretical analysis and experimental results for both transverse and longitudinal stresses builds confidence in the application of the generalized plane strain theory to the calculation of residual stresses in multipass weldments.

104. The distribution of longitudinal and transverse stresses at the top and bottom surface of the 1/2-in.-thick plate (Test 1) along the transverse direction as predicted by the numerical analysis are plotted in Figure 68. Longitudinal stresses show higher tensile values than transverse stresses within 1/2 in. from the center line. Longitudinal stress decreases rapidly from tensile to compressive stress near the heat affected zone and then gradually increases away from the weld line. Transverse stress shows a similar trend decreasing to a zero stress state. Compressive transverse stress exists at weld center line. This phenomenon seems difficult to explain. However, other researchers have found similar trend (Free and Porter Goff 1989). Further studies will be necessary to model thermomechanical behaviors in the fusion area. Shear stress is negligible compared with longitudinal or transverse stresses. Stress distributions at the surface of the 1-in.-thick plate are given in Figure 69 and Figure 70 (Test 2 and
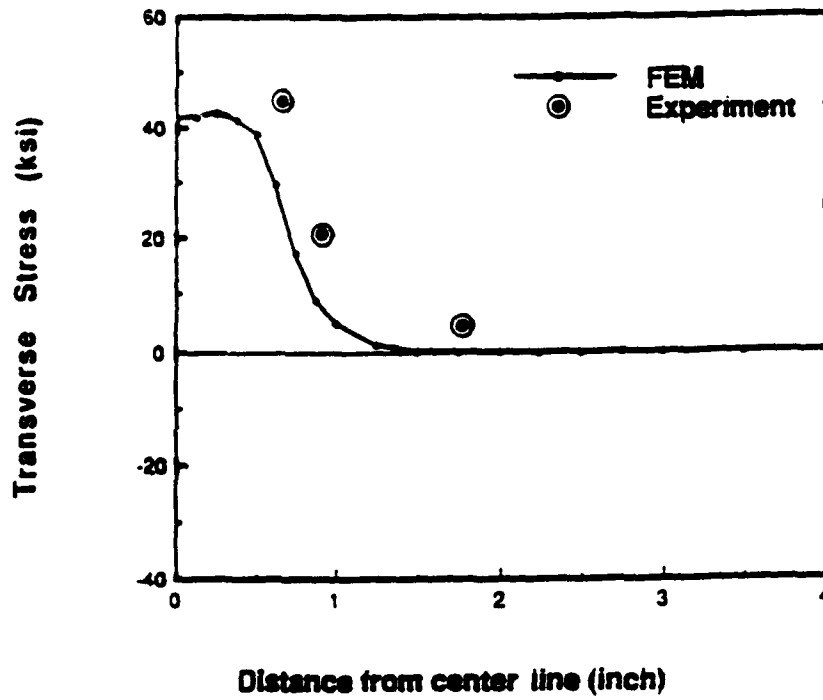
Figure 64. Transverse stress at the top surface of
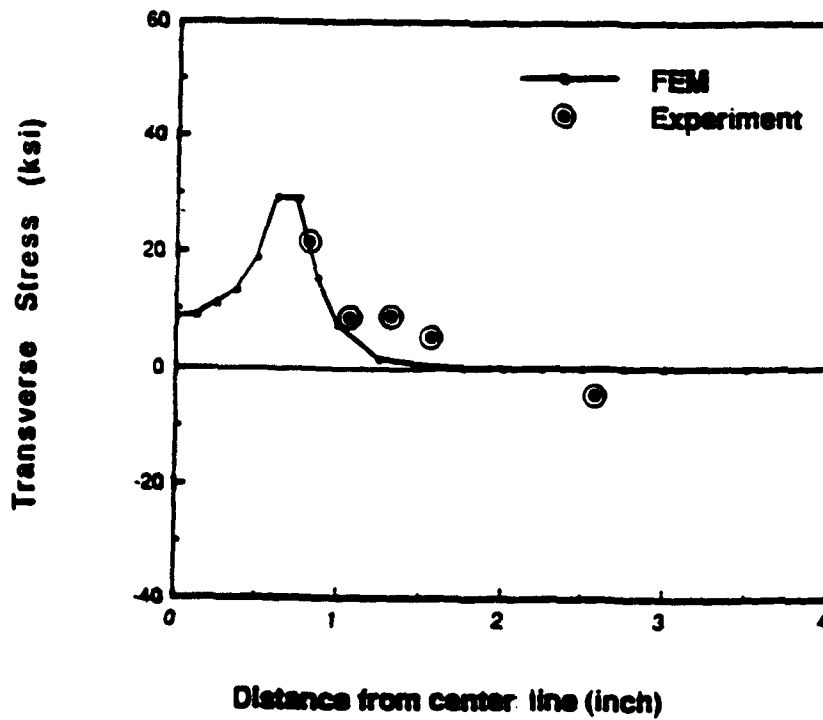1-in. plate (double V- groove, Test 2)

Figure 65. Transverse stress at the top surface of
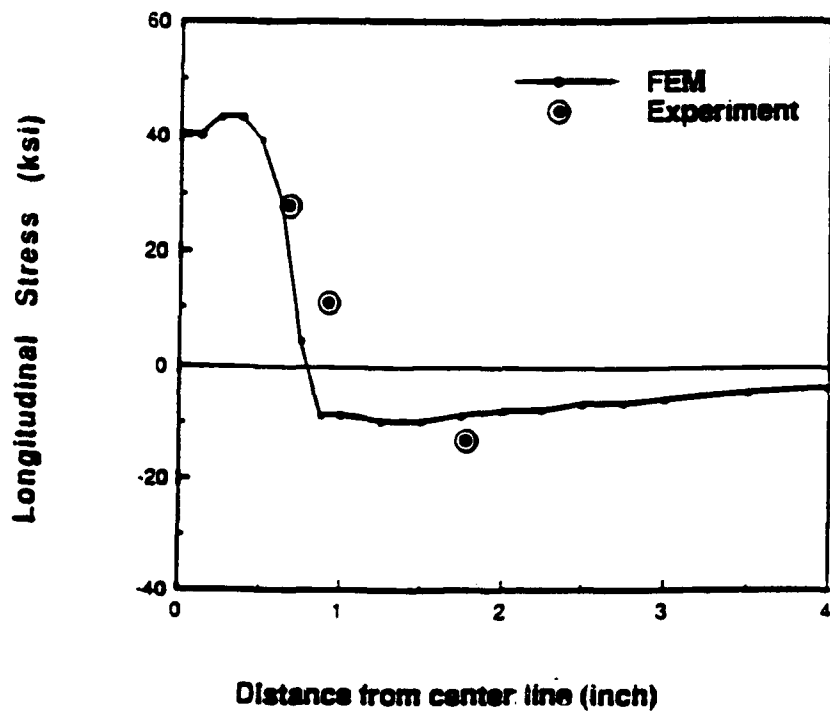1-in. plate (single V-groove, Test 3)

Figure 66. Longitudinal stress at the top surface of
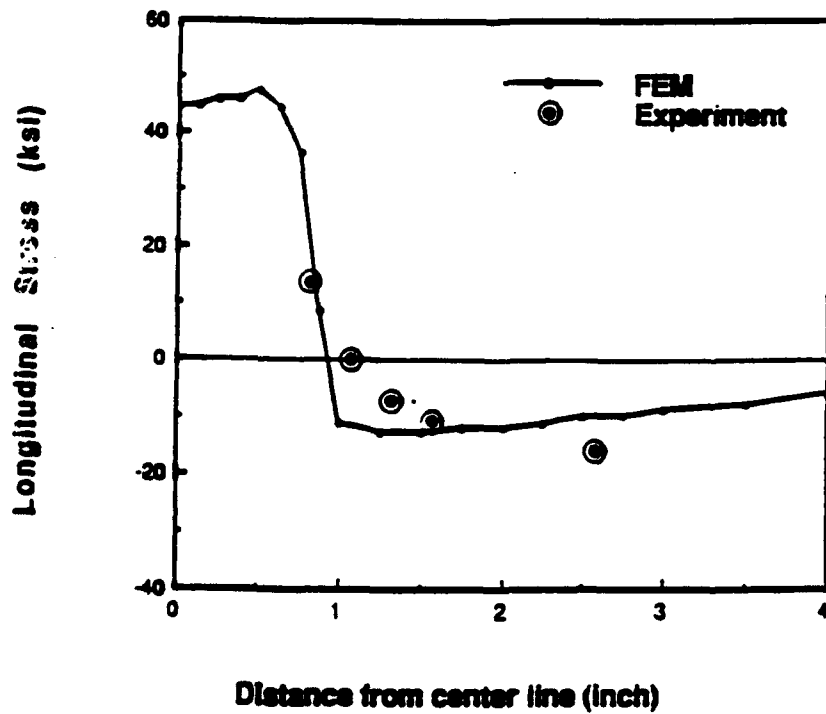1-in. plate (double V-groove, Test 2)

Figure 67. Longitudinal stress at the top surface
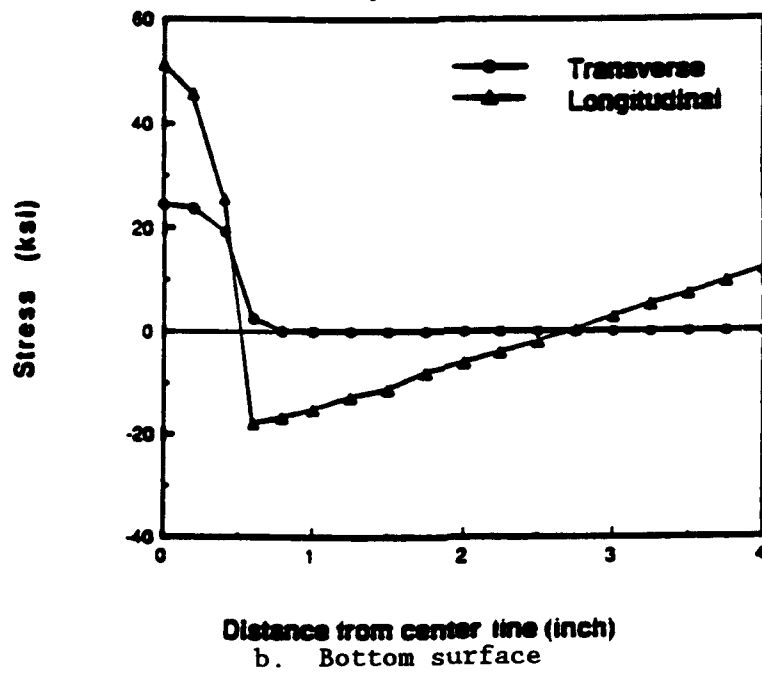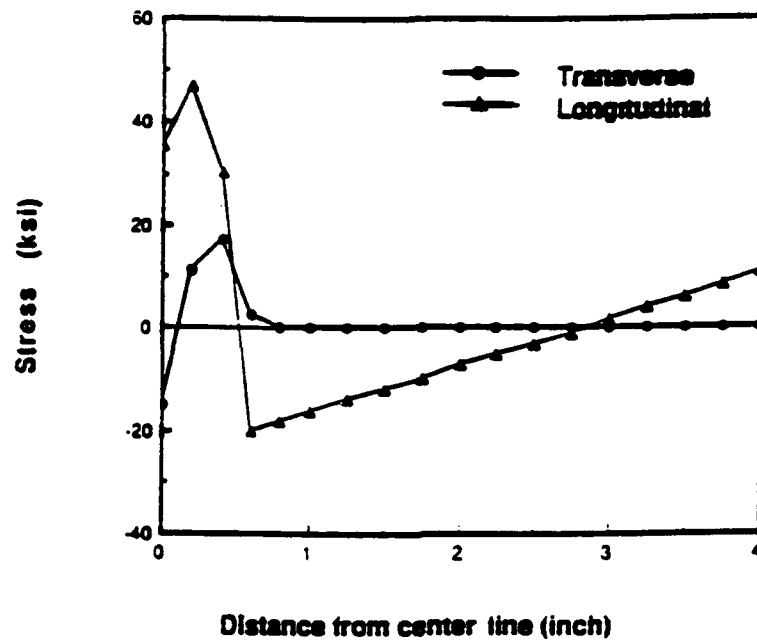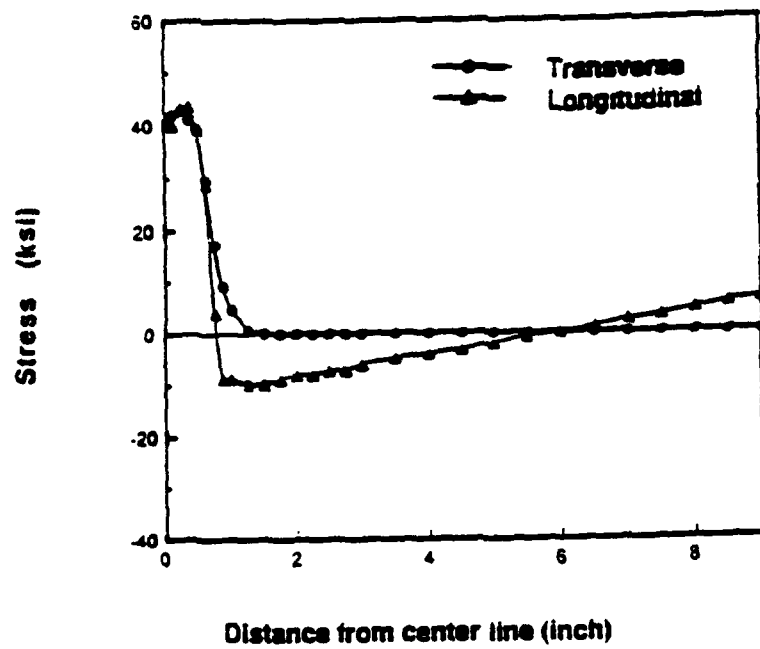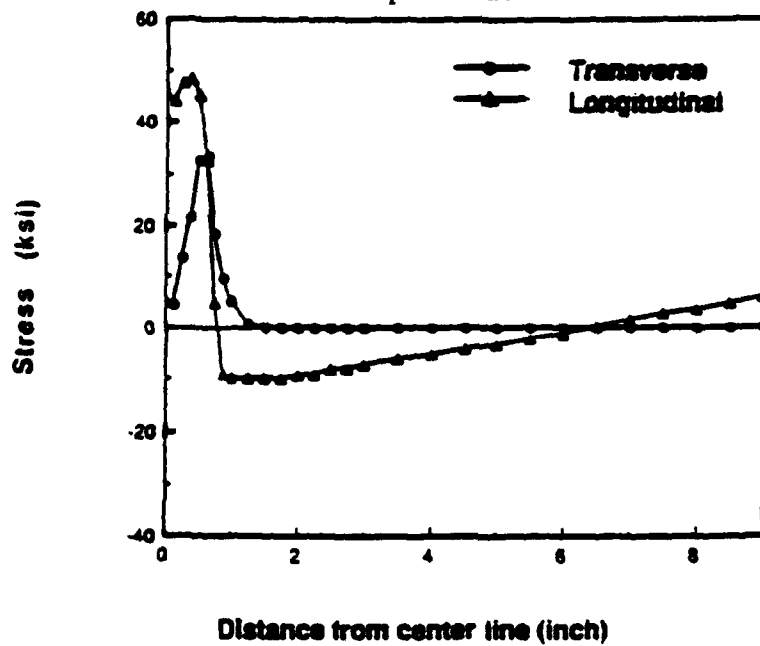of 1-in. plate (single V-groove, Test 3)

a. Top surface

b. Bottom surface

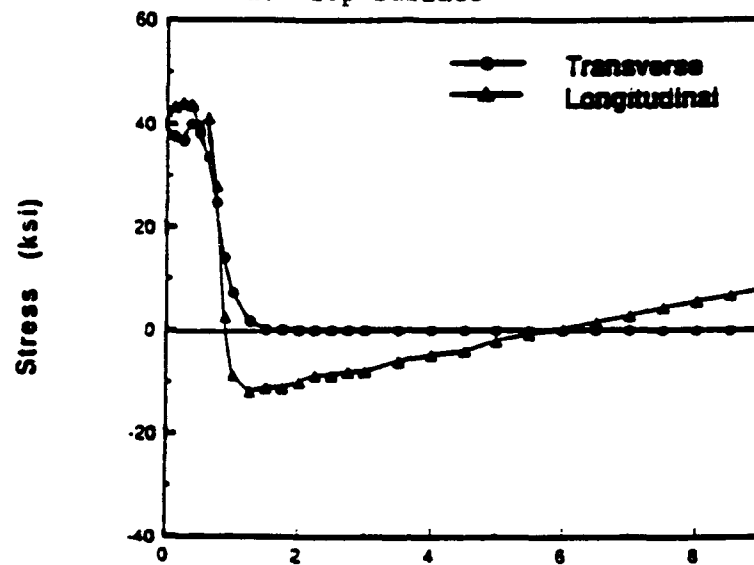Figure 68.   Stress distributions for 1/2-in. plate
(single bevel, Test 1)

a. Top surface

b. Bottom surface

Figure 69.   Stress distributions for 1-in. plate
             (double V-groove, Test 2)

91
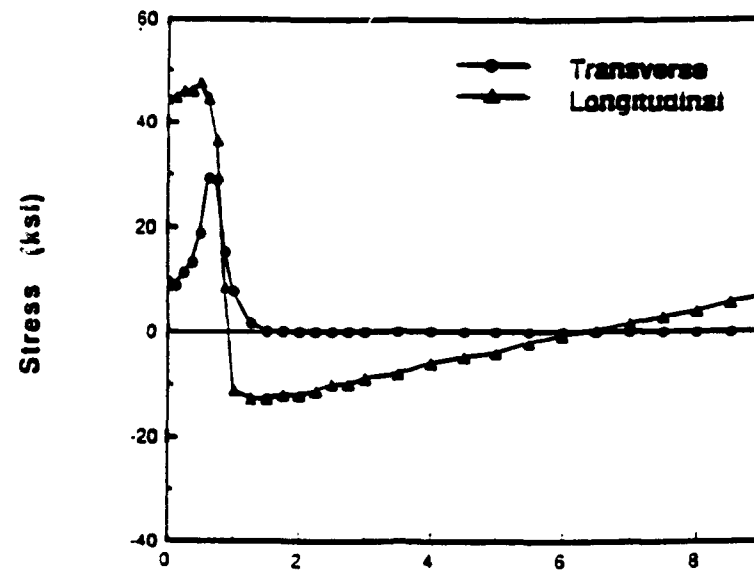
Figure 70. Stress distributions for 1-in. plate (single V-groove, Test 3)

Test 3). Both figures show similar distribution and size of tensile zone, except for transverse stresses at the weld area. Figure 71 shows the longitudinal and transverse stresses at the surface of a 2-in.-thick plate with a double V-groove. Same heat input and welding speed for the 1-in.-thick plate with a single V-groove (Test 3) were used for each side of the groove. The numerical results indicate that the size of the tensile zone is increased by about 60 percent for longitudinal stress and 120 percent for transverse stress compared to the 1-in.-thick plate with a double V-groove; however, the general trend for the stress distribution is very similar to the 1/2- and 1-in.-thick plates.

105. Figure 72 shows the longitudinal and transverse stress variations at the weld center line through the thickness of the 1/2-in.-thick plate (Test 1) evaluated by the finite element method. As shown in the figure, the tensile transverse stress is balanced by compressive stresses in the plate. The longitudinal stress field shows high tensile stress throughout the thickness of the plate.

106. Figure 73 shows the stress field at the weld center line of the 1-in.-thick plate with a double V-groove specimen (Test 2) and Figure 74 shows for single V-groove specimen (Test 3). As shown in the figures, the general trend of the stress distribution is very similar to the 1/2-in.-thick plate except that the transverse stress at the top of the 1-in.-thick plates is in tension. To evaluate the effect of joint geometry on the through thickness stress field, both single and double groove joints were analyzed. The single V-groove joint had higher tensile transverse stress at the bottom surface, with lower tensile transverse stress at the top surface compared to double V- groove specimens. The longitudinal stress field was almost the same at both surfaces. The through thickness stress distribution at the weld center line for the 2-in.-plate is shown in Figure 75. The general trend of the stress field is very similar to the 1-in.-thick plate with a double V-groove.

107. Figures 76 through 79 illustrate stress contours of the cross sections near weld center line. Comparison of the figures yields useful information that the basic trends of the stress distribution through the thickness are primarily dependent on the shape of the weld groove. The plates welded with a single V-groove show high tensile longitudinal stresses at the top surface of the plate and high tensile transverse stresses at the bottom of the plate. The plates welded with double V-groove show high tensile longitudinal stresses at the bottom of the plate and high tensile transverse stresses
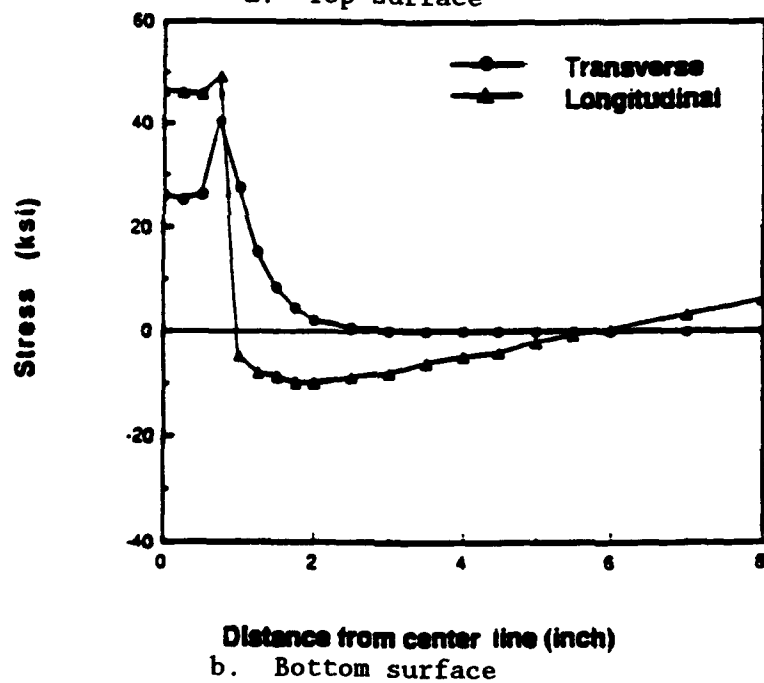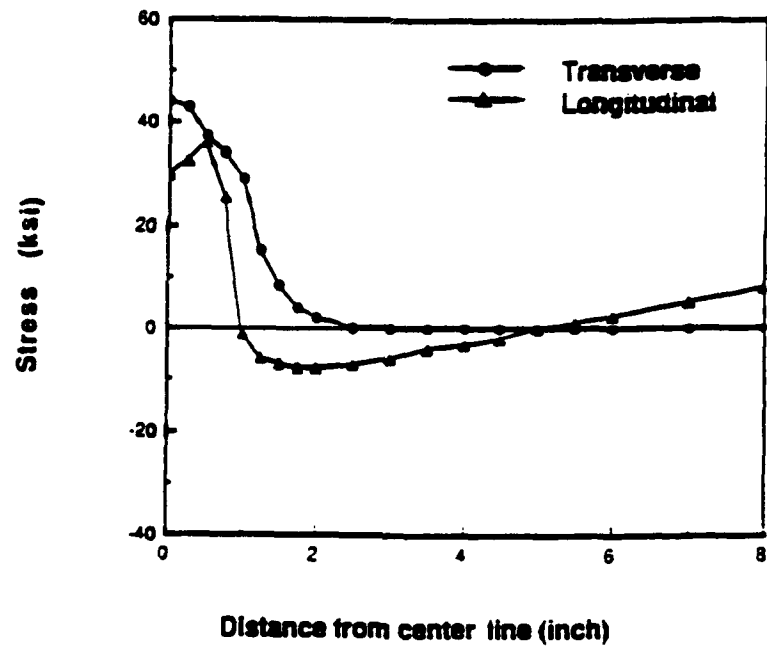
93

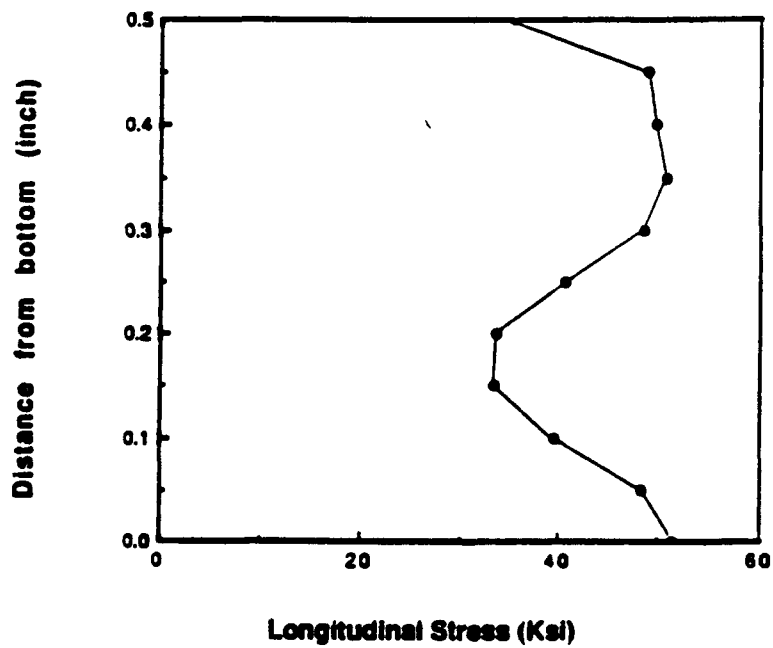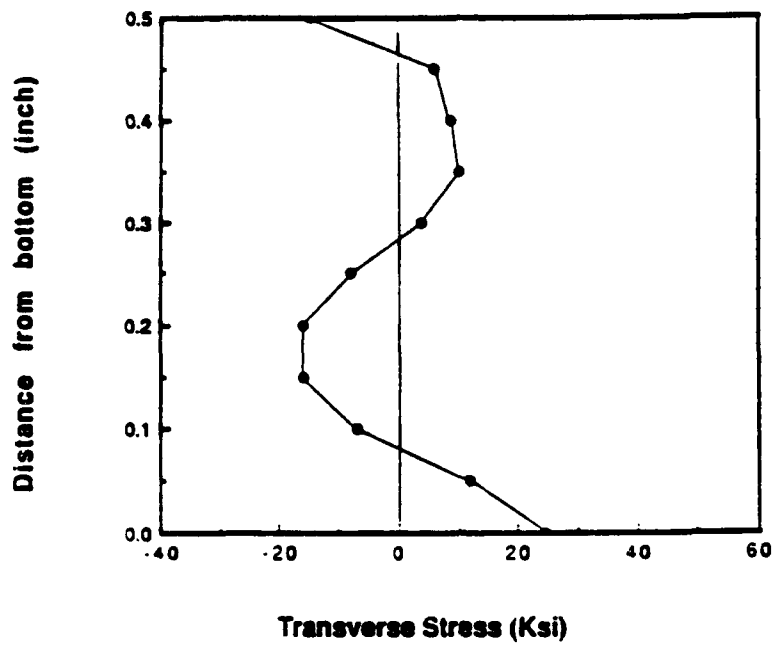**Figure 71.** Stress distributions for 2-in. plate (double V-groove)

Figure 72. Through-thickness stresses for 1/2-in.
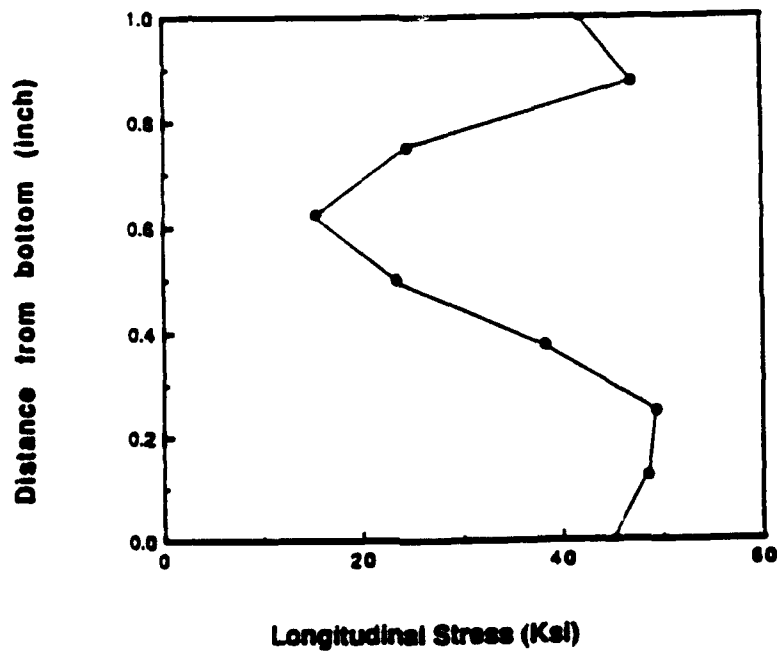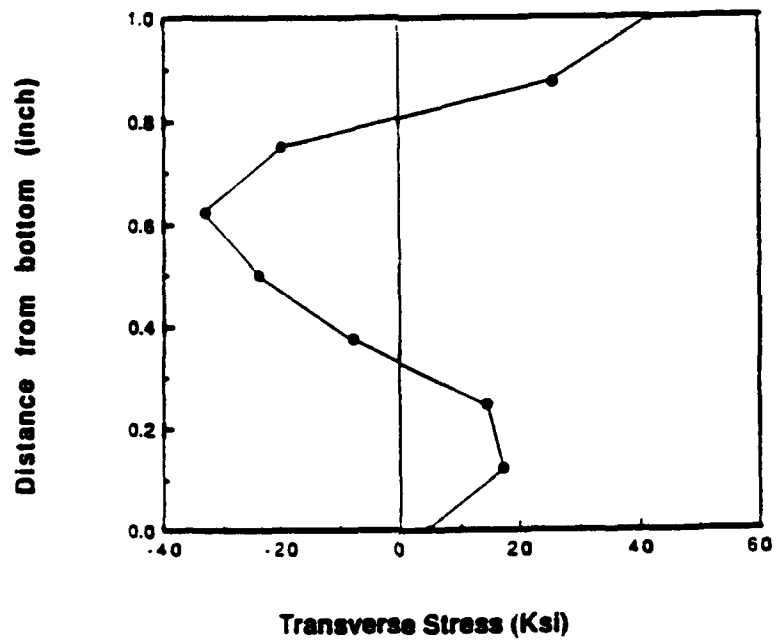plate at weld center line (single bevel, Test 1)

Figure 73. Through-thickness stresses for 1-in. plate
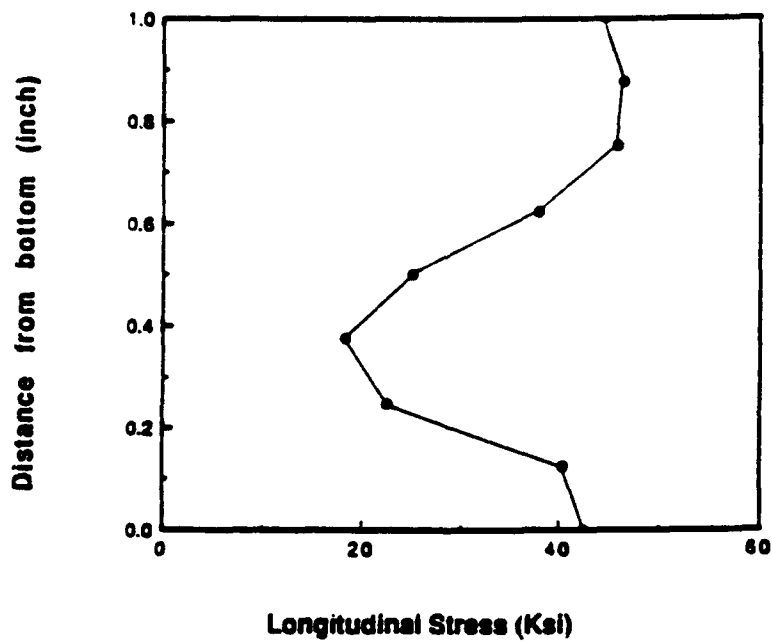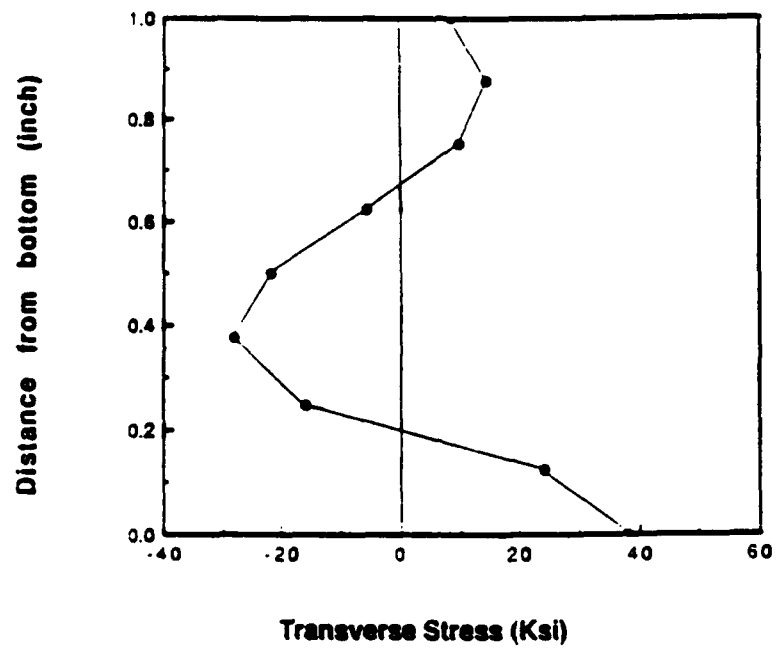at weld center line (double V-groove, Test 2)

Figure 74. Through-thickness stresses for 1-in. plate
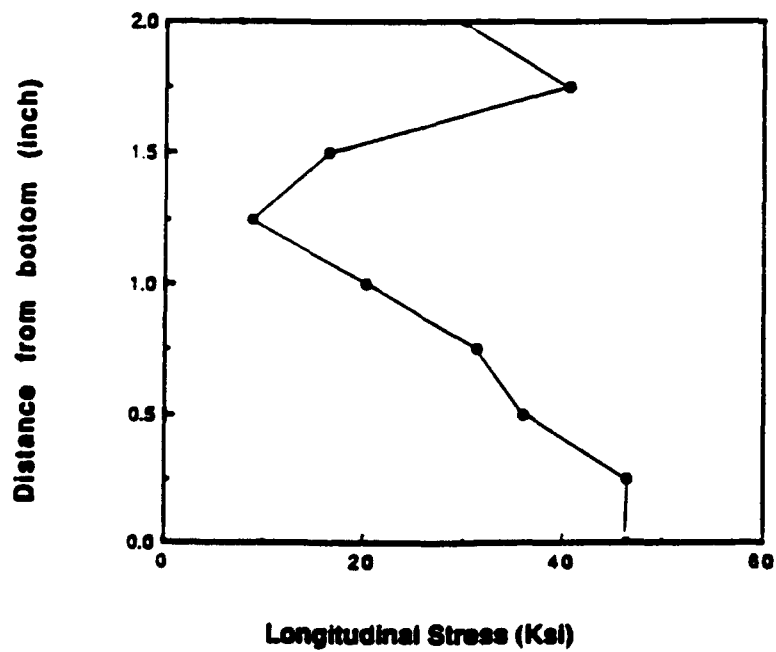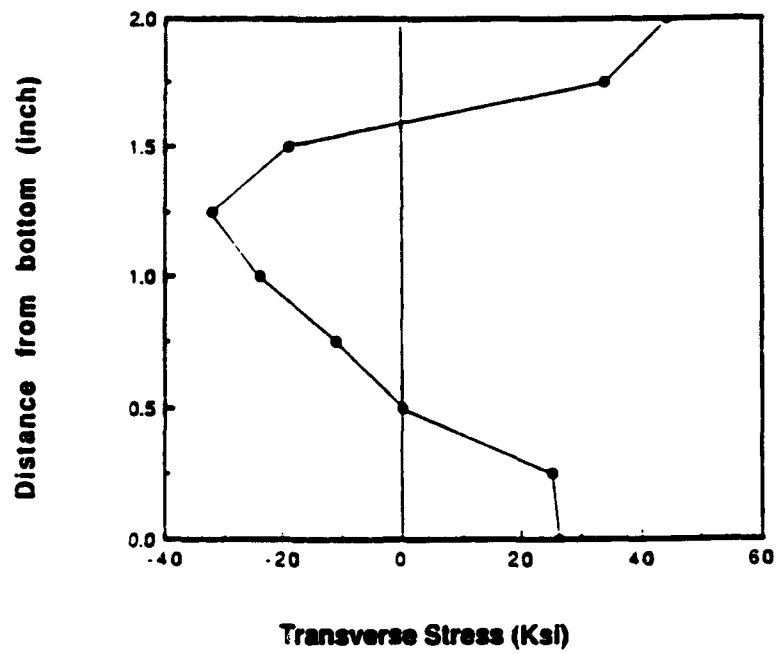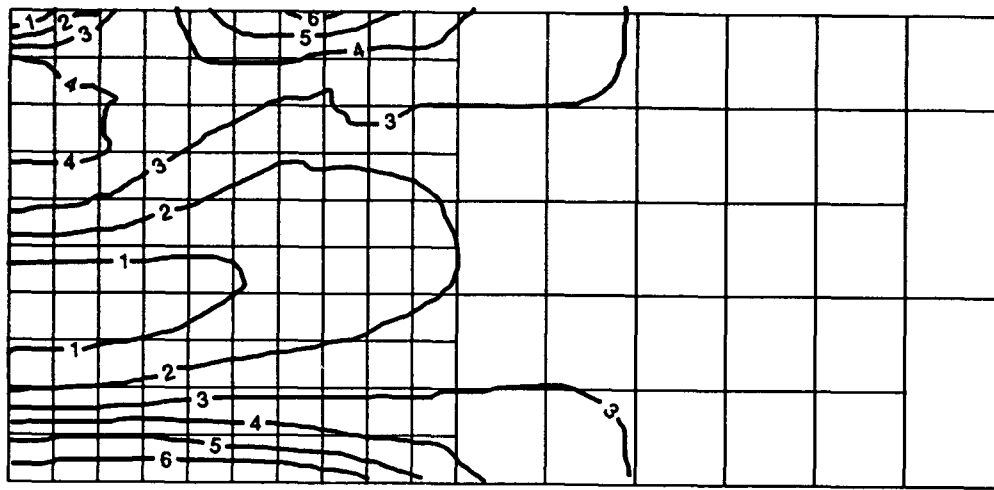at weld center line (single V-groove, Test 3)

97

Figure 75. Through-thickness stresses for 2-in. plate at
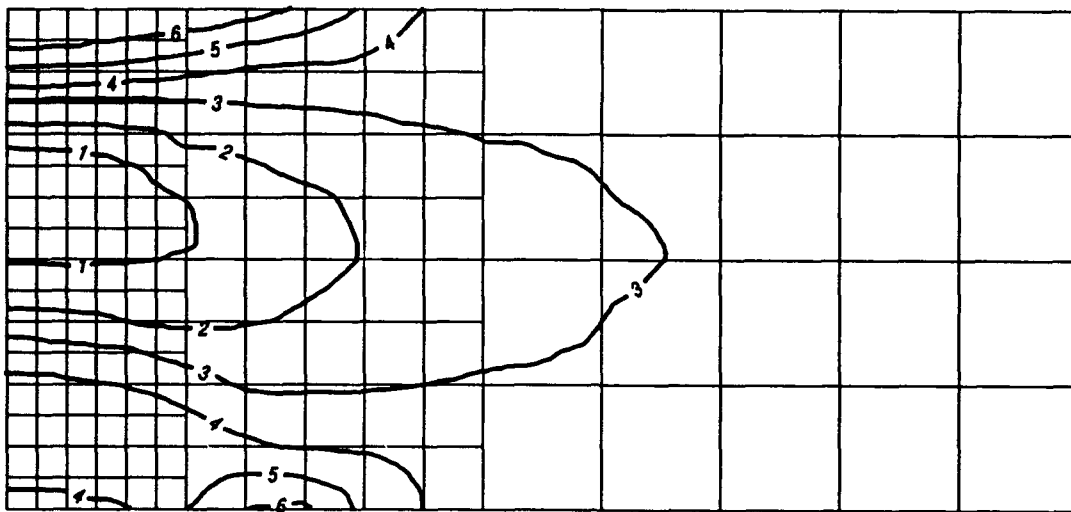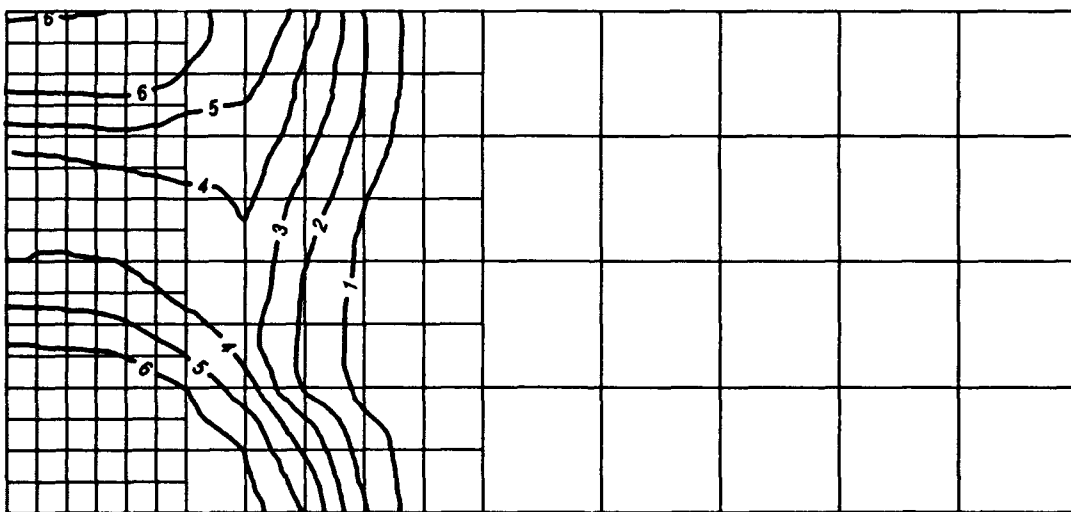weld center line (double V-groove)

98

a. Transverse stress

b. Longitudinal stress

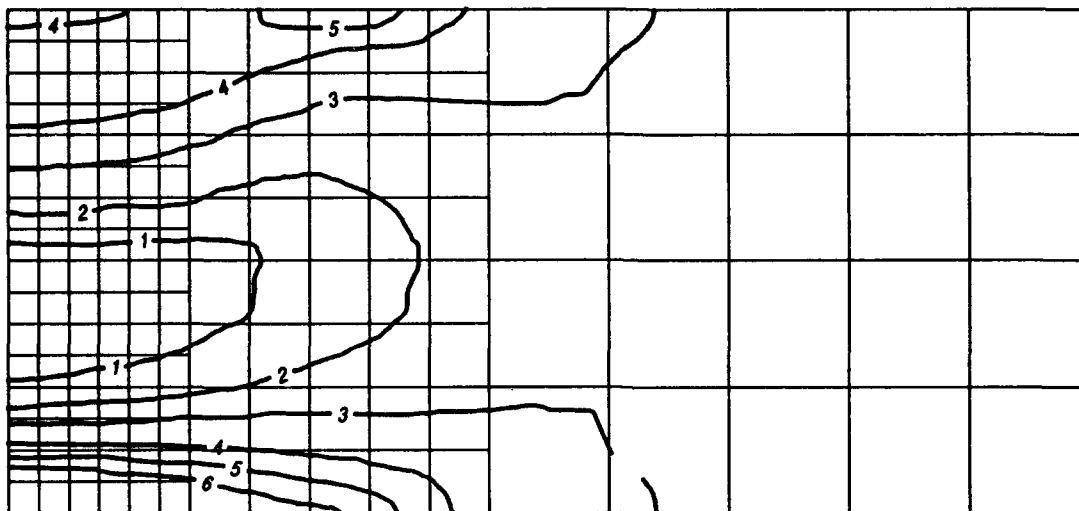Figure 76. Stress contours for 1/2-in. plate (single bevel, Test 1)
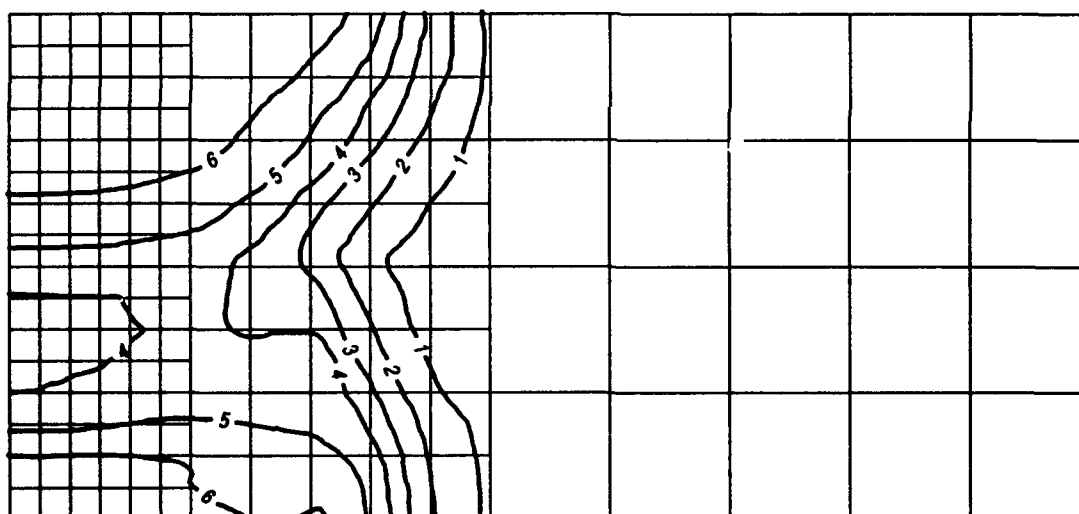
a. Transverse tress

b. Longitudinal stress

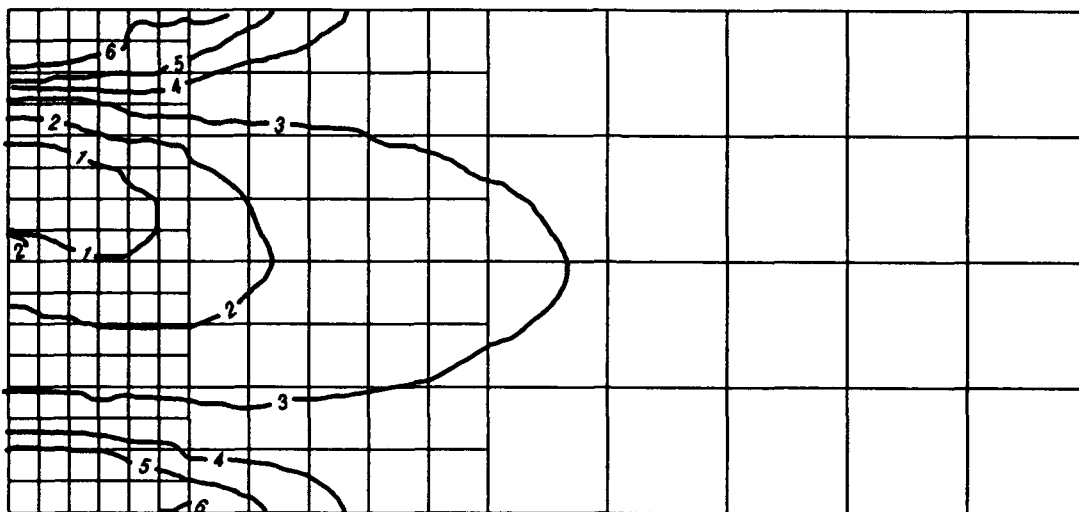Figure 77. Stress contours for 1-in. plate (double V-groove, Test 2)
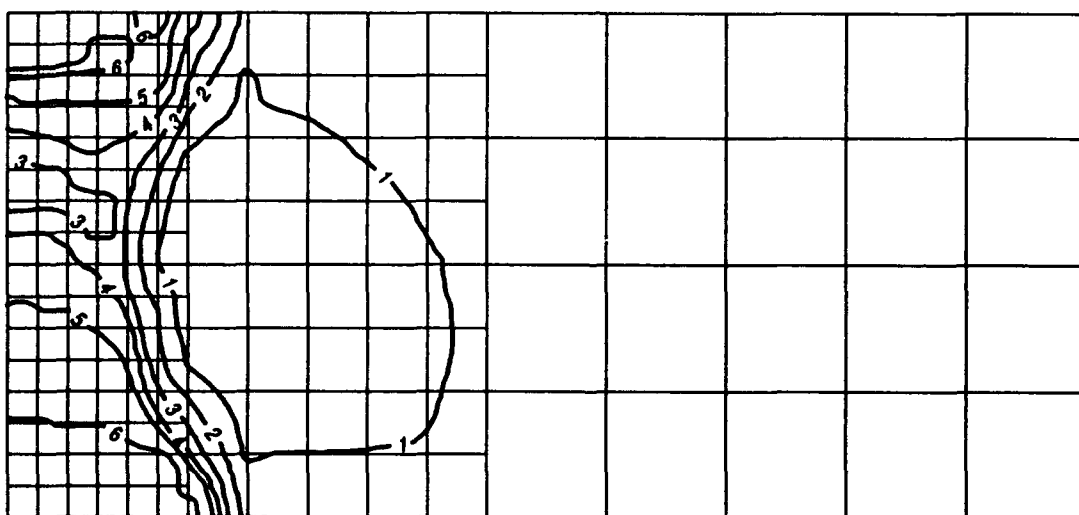
100

a. Transverse stress

b. Longitudinal stress

Figure 78. Stress contours for 1-in. plate (single V-groove, Test 3)

a. Transverse stress
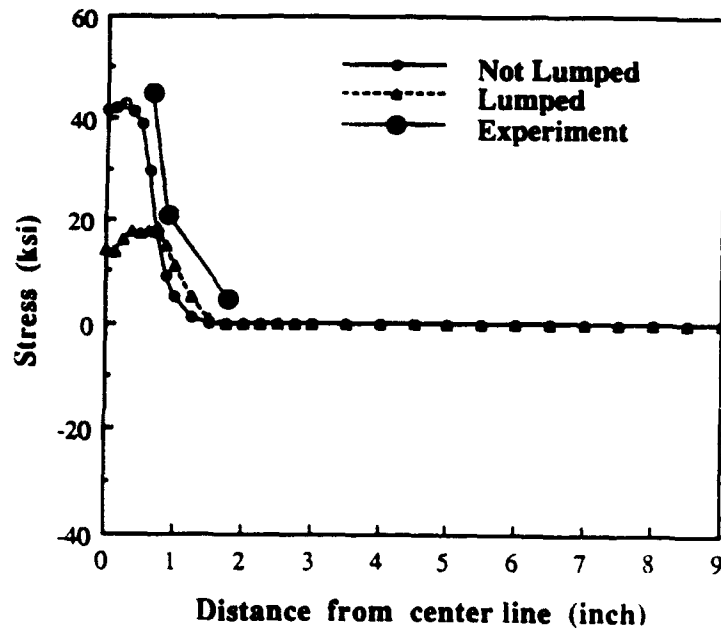

b. Longitudinal stress

Figure 79. Stress contours for 2-in. plate (double V-groove)

at the top of the plate. The size of the tensile stress zone increases as the number of weld passes increases.
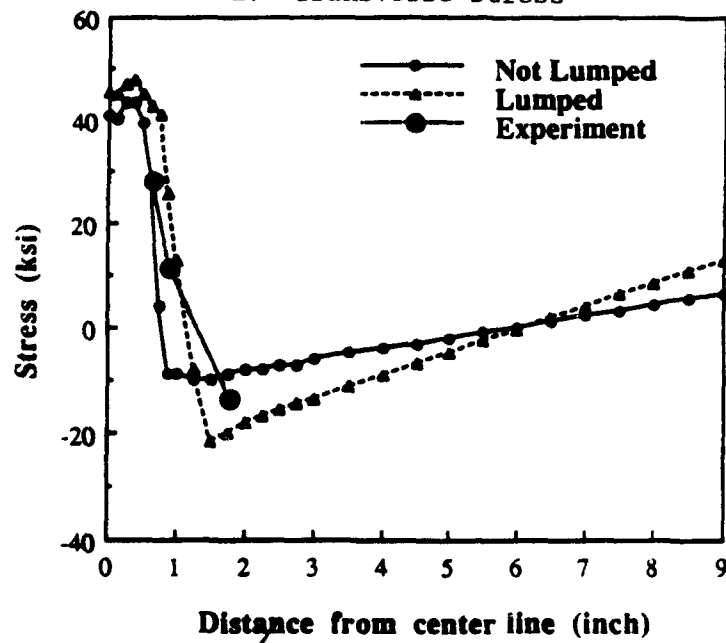
108. The through-thickness stress distribution is very useful for fracture assessment of weldments. The magnitude and type (tensile or compressive) of residual stress around crack tips should be considered in a fracture evaluation or prediction of remaining life of a structure subjected to a fatigue loading.

109. Figures 80 and 81 show the results of the thermomechanical stress analyses using a lumped and not lumped model. Figure 80 shows the longitudinal and transverse stresses at the top surface of a performed 1-in.-thick plate with a double V-groove. Eleven passes were lumped into six passes. The lumped model results are compared with the results of the first model (not lumped) and experimental data. The tensile zone was increased by about 1/3 in. in the lumped model. The lumped model showed higher longitudinal compressive stress outside the weld area than the nonlumped model.

110. Figure 81 shows the longitudinal and transverse stress distributions at the weld center line through the thickness of the 2-in.-thick plate with a double V-groove joint. Thirty-two passes were reduced to fourteen passes in the lumped model. As shown in Figure 81, the lumped model predicted lower tensile longitudinal stress through the thickness than the first model (not lumped). Both transverse and longitudinal stress distribution showed similar shapes.
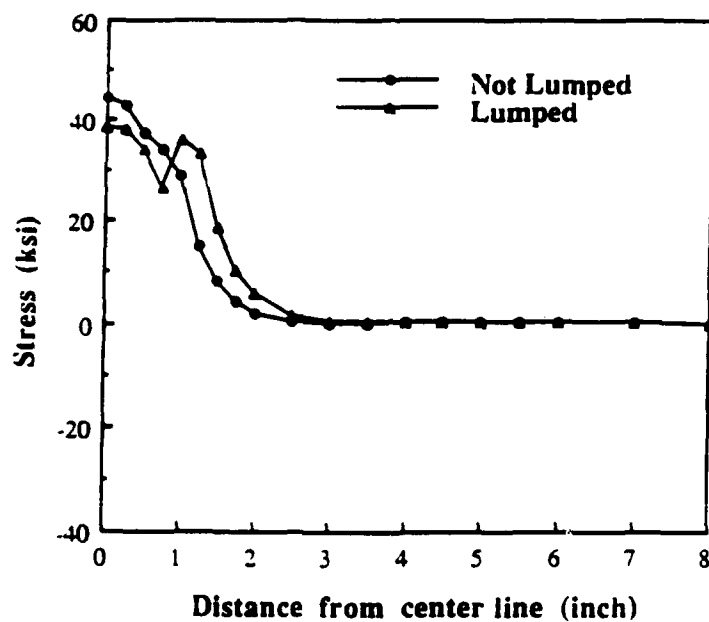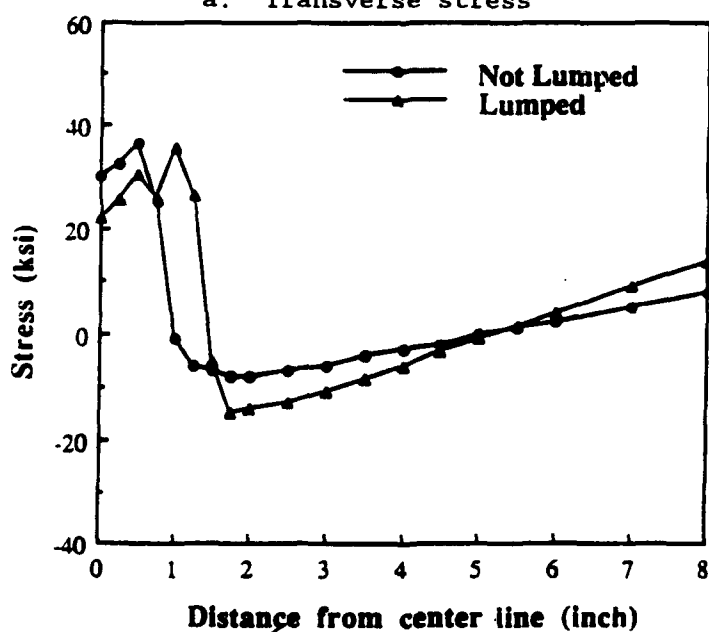
a. Transverse stress

b. Longitudinal stress

Figure 80. Stress distributions at the top surface
of 1-in. plate with double V-groove (Comparison of
two models)

a. Transverse stress

b. Longitudinal stress

Figure 81. Through-thickness stress distributions for
2-in. plate with double V-groove at weld center line
(Comparison of two models)

105

PART V: CONCLUSIONS

111. The nonlinear finite element method was used to analyze residual stress field of a plate during welding. The results were compared with the experimental test data containing temperature and residual stress. This report concentrated on developing a methodology for evaluating residual stress field both numerically and experimentally.

112. The effect of the joint geometry on the residual stress was studied by using two different grooves, a single V-groove and a double V-groove. Longitudinal and transverse residual stresses on the plate surface were the primary concern of the analysis. The stress distribution through the plate thickness was obtained using this finite element analysis.

113. From the investigation carried out in this study, the following conclusions are drawn.

   <u>a</u>. Uncoupled nonlinear finite element method is a reasonable tool for evaluating residual stress of the welded joints. In this analysis, ramp function heat input assumption was provided to avoid numerical instability.

   <u>b</u>. Lumped pass modeling techniques were adopted to reduce total computation time and cost without decreasing the accuracy.

   <u>c</u>. The temperature history during welding can be accurately recorded through the use of thermocouples and the data acquisition system.

   <u>d</u>. In the residual stress measurement, the blind-hole drilling method gives more consistent results relative to other techniques which were quite sensitive to the surface condition.

   <u>e</u>. The transverse stress field at the surface showed tensile stress and never down to compressive stress but the longitudinal stress field changed tensile to compressive stress. The transverse stress field is as important as longitudinal stress in most of the cases at the surface. However, transverse stress is not as significant as longitudinal stress in the middle of the plate thickness because of the magnitude.

   <u>f</u>. The stress field through-thickness direction was investigated and showed that the maximum stress was near the surface. The longitudinal stress showed high tensile stress through the thickness, but the transverse stress changed tensile to compression near the middle of the thickness.

   <u>g</u>. The joint geometry was not a sensitive parameter as far as residual stress was concerned.

   <u>h</u>. This analysis brought confidence about the numerical simulation of the complicated multipass welding simulation.

106

i. Supercomputer is necessary for analyzing this type of analysis even though two-dimensional and lumped pass assumption was adopted.

REFERENCES

American Society for Metals. 1948. <u>Metals Handbook.</u> Cleveland, Ohio.

American Society for Testing and Materials. 1985. <u>Determining Residual Stresses by the Hole-Drilling Strain Gage Method.</u> ASTM Standard E837-85, Philadelphia, PA.

American Welding Society. 1979. "Specification for Carbon Steel Filler Metals for Gas Shielded Arc Welding," ANSI/AWS A5.18-79, Miami, FL.

Argyris, J. H., Szimmat, J., and William, K. J. 1982. Computational Aspects of Welding Stress Analysis," *Computer Methods in Applied Mechanics and Engineering*, Vol 33, pp 635-66.

Boyles, L. G., Lee, W. C., and Kim, D. S. 1987. "Weld Joint Analysis for CIT Vacuum Chamber," Final Report to GA Technologies.

Free, J. A., and Porter Goff, R. F. D. 1989. "Predicting Residual Stress in Multi-Pass Weldments with the Finite Element Method," *Computer & Structures*, Vol 32, No. 2, pp 365-378.

Hibbit, Karlson, and Sorensen, Inc. 1988. <u>ABAQUS Users Manual, Version 4.</u> Providence, RI.

Inframetrics. 1981. <u>Operations Manual.</u> Bedford, MA.

Kelsey, R. A. 1956. "Measuring Non-Uniform Residual Stresses by the Hole Drilling Method," <u>Proceedings SESA.</u> Vol 14, No. 1, pp 181-194, Westport, CT.

Majid Kabiri. 1984. "Nonuniform Residual Stress Measurement by the Hole-Drilling Technique," *Experimental Mechanics*, Vol 24, No. 4, pp 328-336.

Masubuchi, K. 1980a. <u>Analysis of Welded Structures.</u> Pergamon Press, Elmsford, NY, p 192.

_____. 1980b. <u>Analysis of Welded Structures.</u> Pergamon Press, Elmsford, NY, pp 112-147.

Measurement Group, Inc. 1988. "Measurement of Residual Stresses by the Blind Hole Drilling Method," Technique Note 503, Raleigh, NC.

_____. 1989. "Strain Gage Selection Criteria, Procedures, Recommendations," Technique Note 505-1, Raleigh, NC.

Muskhelishvili, N. I. 1953. <u>Some Basic Problems in the Mathematical Theory of Elasticity.</u> Noordhoff, Groningen, Holland, pp 202-204.

Niku-Lari, A., Lu, J., and Flavenot, J. F. 1985. "Measurement of Residual Stress Distribution by the Incremental Hole-Drilling Method," *Experimental Mechanics*, Vol 25, No. 2, pp 175-185.

Rendler, N. J., and Vigness, I. 1966. "Hole-Drilling Strain-Gage Method of Measuring Residual Stresses." <u>Proceedings, SESA XXIII.</u> No. 2, pp 577-586, Westport, CT.

Schajer, G. S. 1981. "Application of Finite Element Calculations to Residual Stress Measurements," *Journal of Engineering Materials and Technology*, Vol 103, pp 157-163.

Tekriwal, P., Stitt, M., and Mazumder, J. 1987 (Oct). "Finite Element Modelling of Heat Transfer for Gas Tungsten Arc Welding," *Metal Construction*, pp 599R-606R.

Tiitto, S. 1989. "Magneto-elastic Testing of Uniaxial and Biaxial Stresses," International Conference on Residual Stresses, Societe Francoise de Metallungie, Nancy, France.

Timoshenko, S., and Goodier, J. M. 1951. *Theory of Elasticity*, McGraw-Hill, New York.

Ueda, Y., and Yamakawa, T. 1973. "Analysis of Thermal Elasto-Plastic Behavior of Metals During Welding by Finite Element Method," *Japan Welding Society*, No. 42-6, pp 567-577.

Williams, M., and McFetridge, G. 1983 (Apr). "Unbalanced-bridge Computational Techniques and Accuracy for Automated Multichannel Strain-measuring Systems," *Experimental Techniques*, pp 32-37.

APPENDIX A

MAGNETO-ELASTIC STRESS MEASUREMENTS

1. When a ferromagnetic material is subjected to a magnetic field, it becomes magnetized in a rapid series of tiny steps or jumps. These discontinuous changes in magnetization, which are attributed to the reorientations of the walls of the microscopic magnetic domains in the material, may be monitored with sensitive electromagnetic or acoustic detectors. The measured signals, called "Barkhausen noise," are influenced by the residual and/or applied stresses in the material. Under an alternating magnetic field repetitive noise may be obtained. The stress state of material, including residual stress, can therefore be evaluated by monitoring the Barkhausen noise and implementing calibration technique. The relation between noise level and stress is illustrated in Figure A-1.

2. Uniaxial calibration curves have been used to correlate the magneto-elastic Barkhausen noise with stress for a given material. Such curves are obtained by measuring the level of Barkhausen noise while stressing the test piece. Recent experiments have indicated that the accuracy of the calibration could be improved by using biaxial calibration technique (Tiitto 1989). This biaxial calibration technique is to produce all combinations of biaxial strain field in a calibration sample and determine values of the magneto-elastic parameter (MP) in the principal stress directions at each combination. When evaluating stresses in an actual component of the same material, a pair of MP values in the principal stress directions is measured and converted into principal stresses/strains with the aid of biaxial calibration data.

3. In our study, the STRESSCAN 500C unit from AST Co. was used to measure stresses. The STRESSCAN 500C has an adjustable magnetic(MAGN) control. The function of the MAGN is to vary the amount of electrical current passing through the magnetizing coil of the connected sensor. This current determines the magnetic field strength applied to the sample when the sensor is in contact with the sample. The STRESSCAN testing setup is illustrated in Figure A-2. The probe is firmly contacted at the point of interest, and the MP
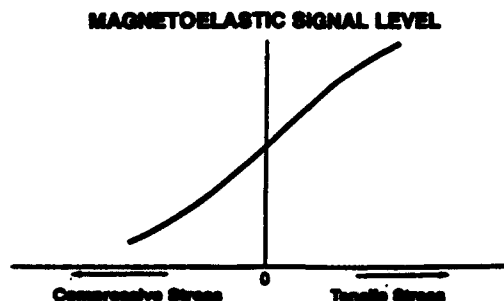

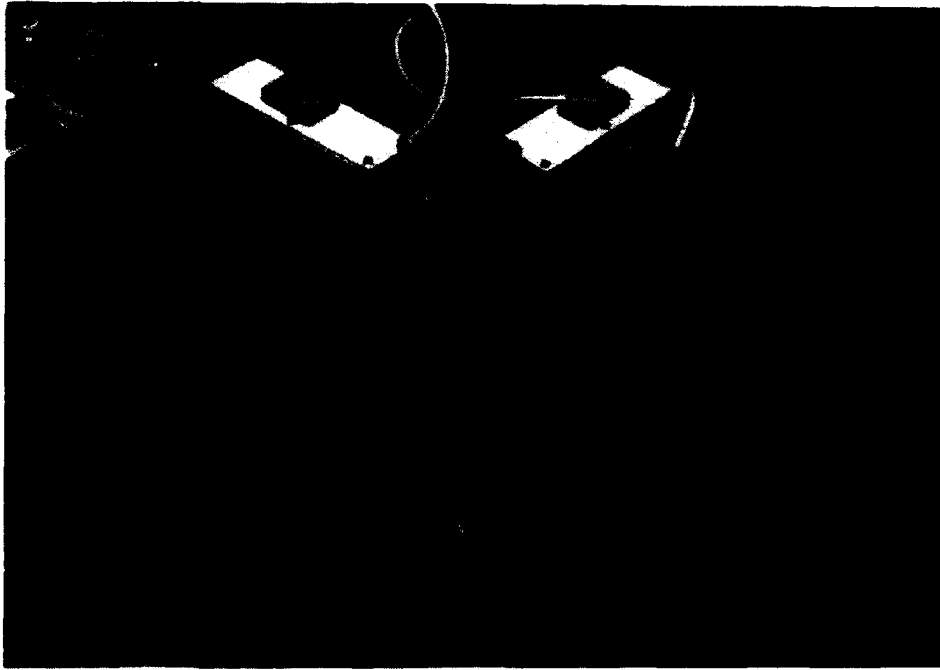Figure A-1. Barkhausen noise response to stress

Figure A-2. Calibration setup for magneto-elastic
stress measurements

value is obtained directly from the STRESSCAN 500C. The MP values are con-
verted into the strain or stress values using a biaxial calibration chart or
curve. As shown in Figure A-3, a special sample should be prepared for mea-
suring the MP values in both directions, longitudinal and transverse, to
obtain the biaxial calibration chart. Table A-1 shows a biaxial calibration
chart measured from the ASTM A-36 sample. Figure A-4 shows the calibration
curve measured in longitudinal direction of the sample. However, welding
residual stress measurements could not be performed in this project because of
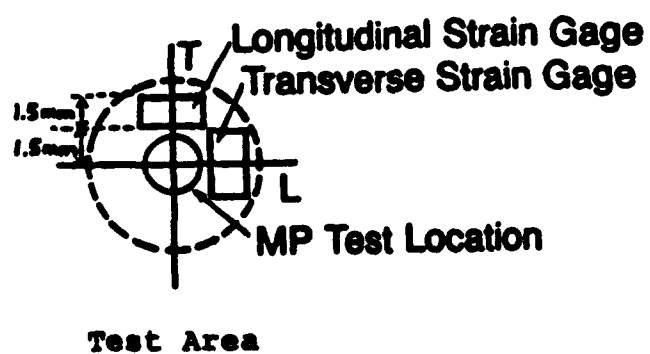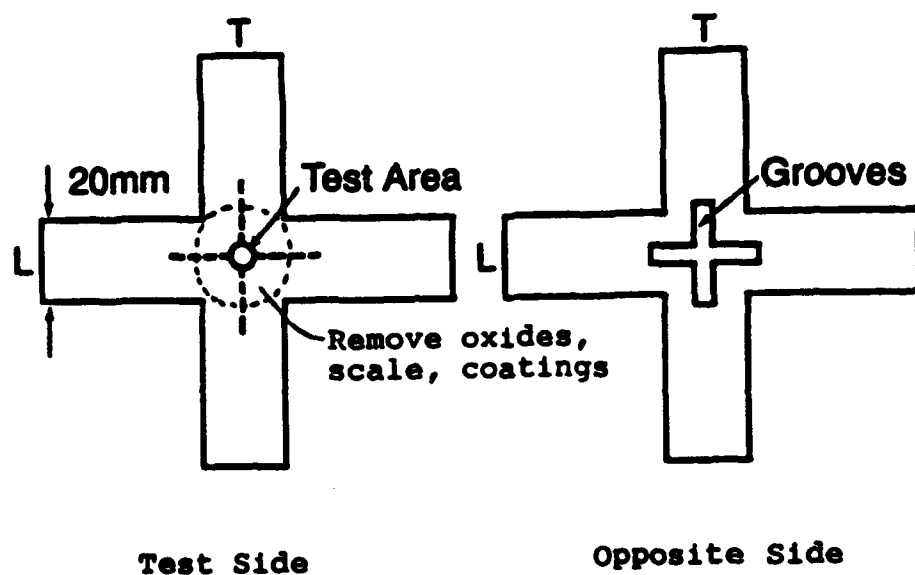the time restraint.

Figure A-3. Schematic drawing of the test sample indicating locations of strain gages and MP testing
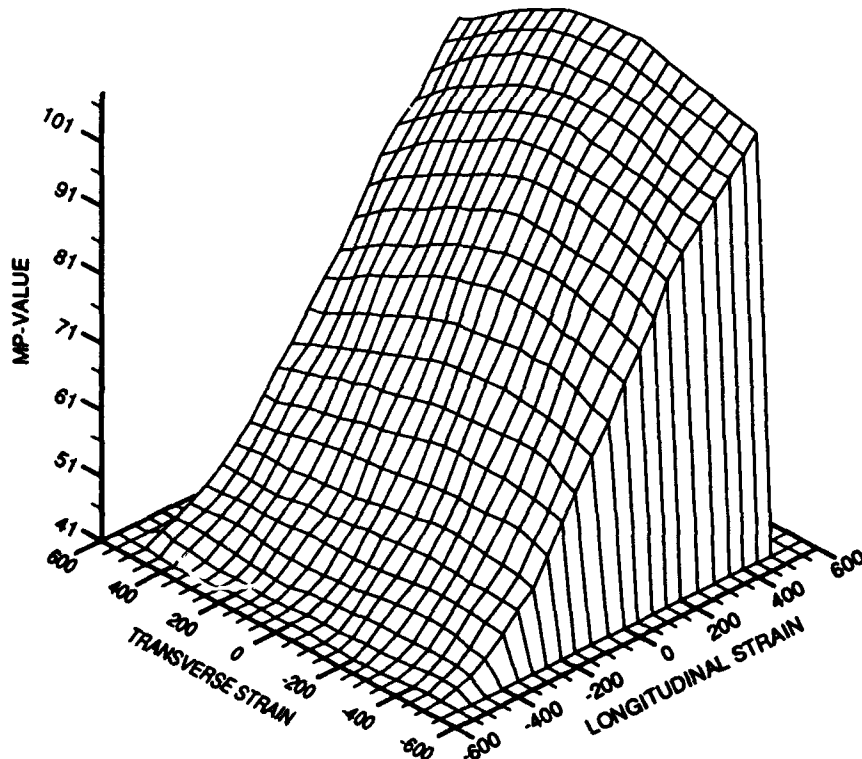
Biaxial Calibration Chart for ASTM A-36 Steel Sample

Longitudinal Strain	Transverse Strain						
	600 L/T	400 L/T	200 L/T	0 L/T	-200 L/T	-400 L/T	-600 L/T
600	102/77	106/66	114/61	115/52	113/48	110/44	108/42
400	87/86	97/73	103/68	105/58	104/51	101/44	99/41
200	73/94	84/84	88/80	95/64	94/57	91/45	87/40
0	62/101	66/92	71/85	75/75	76/59	75/46	67/40
-200	51/103	52/93	53/84	54/75	56/58	56/46	52/42
-400	44/100	44/91	43/79	43/68	44/53	44/44	42/40
-600	40/98	39/88	38/74	37/62	39/49	39/42	39/39

L - Longitudinal MP value
T - Transverse MP value

CALIBRATION CURVE FOR BIAXIAL STRESSES (A-36)

Figure A-4. Biaxial calibration curve measured in longitudinal direction of an ARTM A-36 steel sample